CHALMERS
UNIVERSITY OF TECHNOLOGY

2 µm | WD = 8.5 mm | EHT = 15.00 kV | Signal A = InLens | Mag = 15.00 K X

Experimental Characterization of Pearlitic Rail Steel after Thermomechanical Straining

Master's thesis in Materials Engineering

DAVID CARLSSON & DANIEL GREN

Department of Industrial and Materials Science
Chalmers University of Technology
Gothenburg, Sweden 2019

Experimental Characterization of Pearlitic Rail Steel After Thermomechanical Straining

David Carlsson and Daniel Gren

CHALMERS
UNIVERSITY OF TECHNOLOGY

Experimental characterization of pearlitic rail steel after thermomechanical straining
David Carlsson
Daniel Gren

Cover: Experimental characterization of pearlitic rail steel after thermomechanical
straining

Experimental characterization of pearlitic rail steel after thermomechanical straining
David Carlsson and Daniel Gren
Department of Industrial and Materials Science
Chalmers University of Technology

Abstract

Rails are subjected to very high contact loads during service. The high contact loads cause the surface layer of the rails to be heavily deformed and aligned. The anisotropic nature of the deformed surface layer is prone to crack initiation. The deformed surface layer is also very thin and has a large gradient of accumulated strain. This large gradient makes it difficult to examine the material behavior with conventional testing methods because they requires a fairly uniform microstructure. A predeformation method developed by CHARMEC researchers have proven to be able to produce a material with a fairly uniform microstructure which is consistent with rail field samples with high accumulated shear strain.

The aim with the Master Thesis was to expand the knowledge of the material behaviour of pearlitic rail steels (grade R260) under combined thermal and cyclic mechanical loading. The goal was to produce a microstructure with higher accumulated strains compared to previous work. It was achieved by adding a heat treatment to the predeformation method. An axial-torsion test rig with an induction coil has been used to deform and heat treat solid cylindrical test bars. This was done to obtain a microstructure that was similar to the one found in the field. The material was compared with field samples in terms of microstructure and hardness.

The results of this thesis describes the mechanical behavior of a pearlitic rail steel during simultaneous axial compression and torsion with different compression loads at elevated temperature. The microstructures have been characterized and accumulated strain and hardness have been measured. The highest amount of accumulated strain was obtained with constant heating at 350 °C with an axial compression of 350 MPa and twist rate of 1.5 °/s. The amount of twisting was 3.5 times higher compared to previous work. Heating in between the twisting cycles resulted in the least amount of accumulated strain.

Acknowledgements

The authors would like to thank the supervisor, Dimitrios.N, PhD at department of Industrial and Materials Science, for all the assistance in the lab and the support with the project. The authors would also like to thank the supervisor/examiner, Ahlström.J, Professor at department of Industrial and Materials Science, for the continuous support and guidance throughout the project.

<div align="center">David Carlsson and Daniel Gren, Gothenburg, June 2019</div>

Contents

Contents

List of Figures

List of Figures

List of Tables

1
Introduction

1.1 Background and Motivation

Steels with strength of 6 GPa can be produced through wire drawing of pearlitic based materials. The extreme strength is due to a highly deformed and aligned microstructure. A similar microstructure is found in the surface layer of railway rails and wheels.

The surface layer of rail steels are subjected to very high contact stresses exerted by the train. These stresses lead to large plastic deformations mainly caused by the accumulation of shear strains at the surface. The shear strain accumulation results in an anisotropic surface layer which is a preferential site for the initiation of rolling contact fatigue. Rolling contact fatigue is a major problem in the railway industry and is alone responsible for the majority of maintenance costs.

Steel properties can be tailored by applying different heat and deformation treatments to achieve the requirements for a certain application and even to introduce beneficial gradients in properties. The major reason why steel is such an interesting material is mainly due to its high strength to price ratio. Although steel is an old material, scientists are still able to design stronger steels and therefore there is a need to further investigate them.

Previous work within Chalmers Railway Mechanics (CHARMEC) have included work on deformation of pearlitic steel test bars at room temperature by using a biaxial compression-torsion machine. The latest work resulted in a maximum revolution of two full turns of the cylindrical test bars. CHARMEC researchers want to examine if it is possible to reach even higher strains and strength by performing different deformation experiments at high temperature with different ways to apply the temperature and by this maybe produce a super strong steel?

1.2 Aim

The aim of this master thesis is to expand the knowledge of the material behavior of pearlitic railway rail steels (grade R260) under combined thermal and cyclic mechanical loading. The goal is to reach even higher shear strains compared to previous investigations and try to obtain a microstructure which is representative of the one found in the surface layer of field rail steels. Also, to examine if it is possible to reach higher strength compared to previous investigations conducted by CHARMEC which included biaxial torsion-compression deformation of pearlitic test bars at room temperature.

1.3 Limits

- The experimental characterization will be limited to a fully pearlitic rail steel (grade R260) with respect to initial hardness and initial microstructure.
- The microstructure characterization will be limited to optical microscopy, macrohardness tests and scanning electron microscopy.
- The process parameters will be limited to the test bar geometry, temperature during twisting, heating in between twists, axial compressive stress and cyclic vs monotonic twisting with heating in between cycles.
- The mechanical testing will only be conducted by a biaxial torsion-compression test rig, equipped with an induction coil for heating.

1.4 Specification of Issue

- How is the material behavior affected by the process parameters with respect to hardness and microstructure?
- Can higher shear strains and strengths be reached by combining thermal and cyclic mechanical loading?
- Which temperature should be used for the heat treatment to achieve higher accumulated strains without causing severe spheroidization?
- Is there a need of a new test bar geometry in order to achieve higher shear strains and strength?

1.5 Report Outline

- Theoretical background: This chapter describes the theoretical background needed for the mechanical testing and microstructural characterization.
- Methodology: This chapter presents the tests and the parameters used for the biaxial testing. It also presents how the sample preparation was conducted. It ends with presenting the method used for the microstructural characterization.
- Results: This chapter presents the results from both the biaxial testing and the microstructural characterization.
- Discussion: This chapter discusses the results and connects it with theory. The chapter ends with a discussion about the similarities and differences between the artificially produced steel and field material from the rails.
- Conclusion and future work: Describes the conclusion of the project and suggestions on future work in the area.

2

Theoretical Background

Chapter 2 begins with describing the development of the highly deformed surface layer in rail steels. It continues with presenting common methods used for the production of super strong steels and how their microstructure develops during plastic deformation. Further, the structure, formation, and the effect of heating pearlite is discussed in detail. The chapter continues with describing the basics of dislocation theory, and connects it with the strengthening mechanisms in pearlite. The chapter ends with describing different phenomena which occur during deformation of pearlite at elevated temperatures.

2.1 Stresses Developed at the Wheel-Rail Interface

Loading of a polycrystalline material results in deformation which can either be elastic or plastic. Deformation will be permanent i.e plastic deformation, if the load exceeds the elastic limit of the material, however if the load is below the elastic limit it will return to its undeformed shape. Plastic deformation alters the mechanical behavior of the material, and results in a displacement of the crystal structure [2].

Undeformed polycrystalline steels are generally isotropic on a macroscopic scale, meaning that the properties are more or less similar in all directions. The reason for this is that the grains are randomly oriented and therefore the anisotropic nature of each grain will be averaged out. During service, rail steels are repeatedly plastically deformed in approximately the same directions. This generates an aligned microstructure along the load direction and thus the microstructure becomes anisotropic [2]. At the contact surface between the rail and the wheel, a plastically deformed surface layer is being formed during service. This layer is harder and more brittle compared to the rest of the material. There are mainly two types of loads which generates the deformed surface layer; normal loads and shear loads. The normal loads induce stresses which exceed the elastic limit of the material in a region that starts from the contact area with a depth down to several millimeters. This region is subjected to small to medium strain hardening [2]. The shear loads are caused by traction and cornering [3]. The induced plastic deformation from these loads are severe and result in much higher strains compared to the normal loads [2].
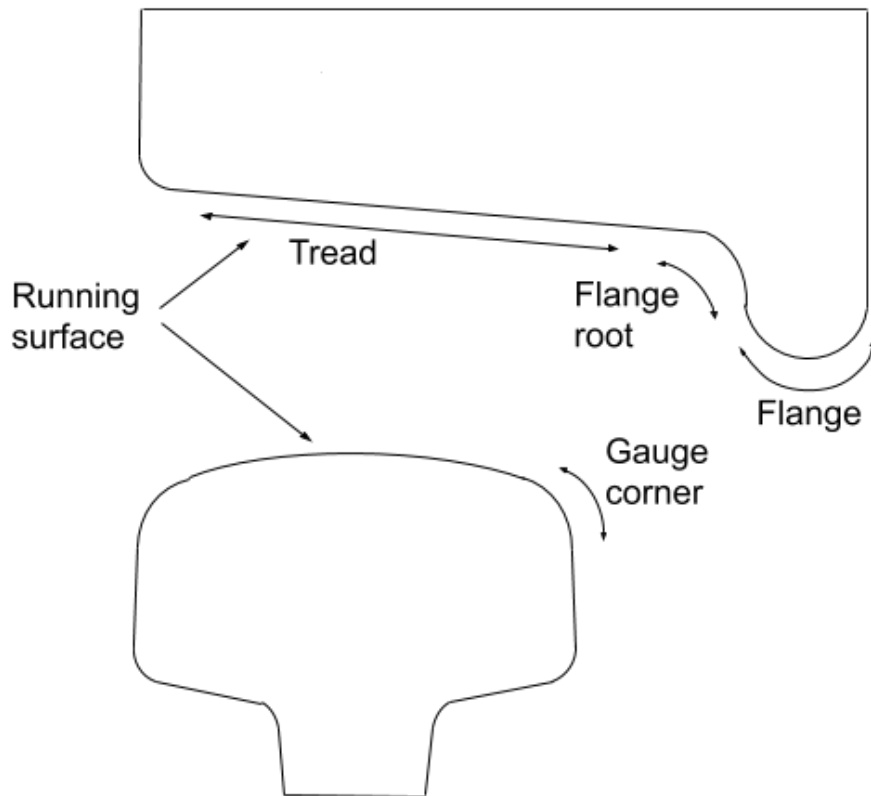
Figure 2.1: Wheel-rail geometry [1]

The thickness and hardness gradient of the deformed surface layer is strongly dependent on which of the two loads is more dominant. Large normal loads create a thicker surface layer with a smaller hardness gradient, and large shear loads result in the opposite [2]. Figure 2.1 shows the typical geometry of the wheel rim and rail head. The most common region of rail-wheel contact is between the wheel tread and the running surface of the rail. The contact stresses in this region are the smallest. During cornering, contact between the flange root and rail gauge corner can occur. This produces a smaller contact area than the former load case, which yields higher contact stresses and results in more severe deformations [1, 4].

2.2 Wheel Rail Contact Mechanics

The material in the railway rails are repeatedly subjected to high contact forces during service and the contact area where the forces are transferred to is small. The field of contact mechanics is a complex area and the existing solutions to the contact problem are simplifications. The contact problem depends on several factors for example: if the surfaces are smooth or rough, if the deformation is elastic or plastic, how large the normal and tangential contact forces are, material properties of the rail and wheel and also if relative motion is static, sliding or rolling [4].

The contact between the rail and wheel can be described as of the rolling-sliding type. Some fundamental properties of the wheel-rail contact stresses can be approx-

imated by using Hertzian theory e.g. the contact geometry and contact stresses [4]. The most simplified solution for the contact problem is by considering the wheel-rail contact as a contact between two cylinders perpendicular to each other i.e circular point contact. This solution is based on several assumptions e.g. that the contact surfaces are smooth, the material response is linear elastic and that the contact is friction-less [4]. The simplified Hertz contact problem is illustrated in figure 2.2.
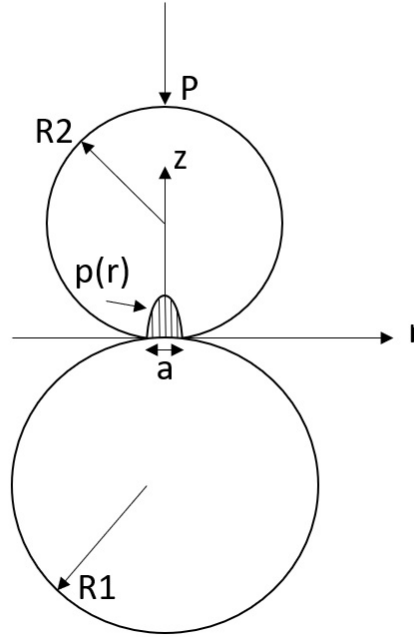
Figure 2.2: Hertz contact for two circular surfaces

The maximum pressure for a given axial load is determined by equation 2.1 [4].

$$p_0 = \left(\frac{6PE^{*2}}{\pi^3 R^2} \right)^{\frac{1}{3}}$$

(2.1)

Where P is the applied load, E^* is the equivalent modulus of elasticity given by equation 2.2 and R is the equivalent radius given by equation 2.3 [4].

$$\frac{1}{E^*} = \frac{1 - \nu_1^2}{E_1} + \frac{1 - \nu_2^2}{E_2}$$

(2.2)

Where E_1 and E_2 is the elasticity modulus for cylinder 1 and 2, respectively. ν_1 and ν_2 is the Poissons ratio for cylinder 1 and 2, respectively.

$$\frac{1}{R} = \frac{1}{R_1} + \frac{1}{R_2}$$

(2.3)

Where R_1 and R_2 is the radius of cylinder 1 and 2, respectively. The pressure upon loading will be distributed over the contact area and the pressure distribution along the r direction is given by equation 2.4 [4]. The contact area upon loading will have the shape of an ellipse and the length of the major axis a, is given by equation 2.5 [4].

$$p(r) = p_0 \sqrt{1 - (\frac{r}{a})^2} \tag{2.4}$$

$$a = \left(\frac{3PR}{4E^*}\right)^{\frac{1}{3}} \tag{2.5}$$

The pressure distribution generates shear stresses within the solids and the maximum shear stress for this simplified contact problem is given by equation 2.6 where the location of the maximum shear stress is given by equation 2.7 [4].

$$q(r) = 0.31 \times p_0 \tag{2.6}$$

$$z = 0.48a \tag{2.7}$$

The depth and magnitude of the maximum shear stress increases with higher load which results in a larger deformed zone [4].

2.3 Biaxial Torsion-Compression Testing

Previous work by [5] showed how a MTS 809 Axial Torsional System can be used for multiaxial fatigue tests by a biaxial torsion-compression test method. These kind of tests are conducted under force/torque control and can be used for simulating the complex stress condition which occur in the rail during service [5].

A predeformation method with the MTS 809 Axial Torsion System has been developed by researchers from CHARMEC and has proven to be able to create samples with a microstructure rather similar to the found in rail field material. The test method involved a multiaxial deformation where the samples were repeatedly loaded in both compression and torsion. The predeformation method has been developed to study the ratcheting behaviour in rail steels [6]. The MTS test rig for the biaxial testing had maximum load cells capacities of 100 kN in axial loading, 1100 Nm in torsional loading and 90° torsional stroke [3].

The specimens used for the biaxial machine were solid cylindrical test bars. During deformation a heterogeneous strain field is obtained within the specimens due to the torsional loading. The shear strains and stresses will be the highest at the surface and these will gradually decrease towards the center of the test bar. At the center, the stresses and strains caused by the torsional loading are zero [3]. The applied compression load causes axial strains which change the overall geometry of the test bar if the elastic limit of the material is exceeded. Plastic deformation due to compression decreases the length of the test bar and increases its diameter. This causes the shear strains at the surface to be even higher. If the compression load is too high the test bar will buckle [3].

2.4 Techniques for Producing Super Strong Steels

By severe plastic deformation (SPD) techniques it is possible to produce nanostructured steels. There are several SPD techniques that are able to produce super

strong steels such as high pressure torsion (HPT), equal channel angular pressing (ECAP), accumulative roll bonding (ARB) and wire drawing [7]. The techniques that resemble most the one used in this project were HPT and wire drawing and will therefore be further described.

2.4.1 High Pressure Torsion

HPT is a technique which has been used in many studies for the production of nanostructured steels [8–11]. The method has also been found to be able to replicate the properties of the deformed surface layer in rail steels [6].

Three main setups for HPT exists: unconstrained, quasi constrained and fully constrained. The quasi-constrained set up is mostly used because it handles some of the problems that can arise with the other two set-ups. HPT use disc shaped samples with a thickness around 10% of the diameter. The basic principle of the technique involves first placing the samples between two anvils, applying a certain pressure and finally twisting by rotating one of the anvils. If the thickness does not change during the process, the deformation can be regarded as simple shear with maximum shear strain at the outer surface [12].

Compressive stresses, suppresses the damage accumulation from the shear stresses and thus large deformations before failure can be achieved i.e the crack formation is suppressed. By applying a high hydrostatic pressure as in the quasi-constrained set up, almost unlimited amounts of strain can be reached. The high strains during HPT leads to grain refinement of the deformed material which enhance the mechanical properties. The main disadvantages with HPT are that the strain is linearly dependent on the radius and that the sample size is very small [12].

2.4.2 Wire Drawing

The strongest steel product that currently can be produced is cold drawn pearlitic steels which can have a strength up to 6 GPa [13]. Wire drawing is a technique in which a steel rod is drawn through one or several dies in order to reduce the cross-sectional area [14]. Cold drawing of pearlitic steels results in a highly anisotropic microstructure with the pearlite lamellae aligned in the drawing direction [15]. The high yield strength of pearlitic steel wires has been suggested from several articles to be due to the reduction in interlamellar spacing (ILS) [13, 15, 16]. The literature study also suggests three strengthening mechanisms for cold-drawn pearlite; boundary strengthening, dislocation strengthening, and solid solution hardening [13].

2.5 Microstructure Development During Plastic Deformation of Pearlitic Steels

Several studies have shown that the lamellar structure in pearlite becomes aligned with the shear direction during HPT tests [8, 10, 11]. According to Ivanisenko et al [10], the microstructure development is affected by how the colonies in the pearlite microstructure is oriented when the shear load is applied. Interlamellar spacing

decreases when colonies are oriented parallel to the shear direction and increases when the colonies are oriented perpendicular to the shear direction. Furthermore, if the lamellae have an unfavourable orientation angle, the lamellae will then have a more bendy and wavy shape [10].

Regarding pure torsion Zhao et al [17] proposed a similar relationship between the lamellae direction with respect to the shear direction for pearlitic steels. Depending on the orientation angle between the lamellae and the shear direction, the interlamellar spacing will either increase or decrease. Orientation angles larger than 90° results in a decrease in interlamellar spacing and for lower angles the interlamellar spacing will increase. With large angles ($> 90°$), the lamellae will align in the shear direction and deform in a similar way as in tension. Straining of lamellae with low angles ($< 90°$) leads to bending of the cementite plates. If the shear strain is large enough the interlamellar spacing decreases, but if its too large the cementite plates will break [17].

2.6 Morphology of Pearlite

The morphology of pearlite is illustrated in figure 2.3. Pearlite is a microstructure consisting of cementite and ferrite lamellae [1]. The microstructure of pearlite can be divided into nodules and colonies. Nodules are formed inside prior austenite grains during the formation of pearlite and consists of colonies. Within each colony the lamellae are aligned [1, 18].
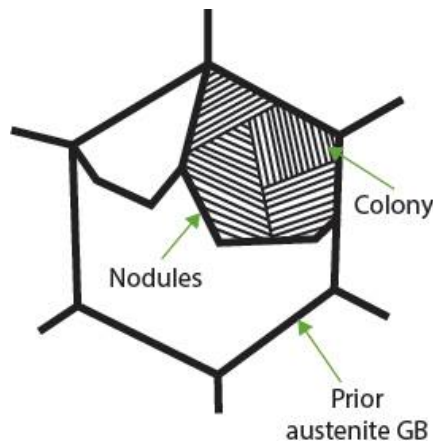
Figure 2.3: Morphology of pearlite

2.7 Phase Transformation of Pearlite

To be able to understand why a phase transformation occurs for any system, one has to study the basics of thermodynamics and the stability of a system. The stability of a system is measured by its Gibbs free energy (G) which is defined as:

$$G = H - TS \tag{2.8}$$

where H is the enthalpy, T is the absolute temperature and S is the entropy [19]. The criterion for a phase transformation to occur is:

$$\Delta G = G_2 - G_1 \, (G_2 < G_1) \tag{2.9}$$

where G_2 and G_1 are the final and initial free energies respectively. A phase transformation occurs if the free energy of the final state is lower than the initial state i.e. if the final state is thermodynamically more stable [19].

Eutectoid phase transformation is defined as a transformation from a single phase solid into a two phase solid structure. In the Fe-C phase diagram, this reaction occurs when austenite(γ) is transformed to pearlite ($\alpha + Fe_3C$). Equation 2.10 below describes the eutectoid transformation at equilibrium for a binary Fe-C alloy [20]:

$$\gamma(0.77wt.\%C) \Longleftrightarrow \alpha(0.02wt.\%C) + Fe_3C(6.67wt.\%C) \tag{2.10}$$
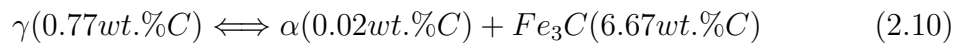
2.8 Pearlite Formation

The following section describes the formation of pearlite in terms of nucleation, growth, nucleation rate and growth rate.

2.8.1 Nucleation and Growth of Pearlite

The transformation from austenite to pearlite is accompanied by redistribution of carbon atoms and a crystallographic change [21]. Nucleation of pearlite most often initiates at the austenite grain boundary and involves both nucleation of ferrite and cementite [22]. The composition and structure of the austenite grain boundary as well as the temperature governs which phase that nucleates first [19, 21].

In the case of grain boundary nucleation, the first phase that nucleates will form an orientation relationship with one of the austenite grains (γ_1), since this lowers the activation energy barrier to nucleation. The orientation relationship generates a semi-coherent interface with γ_1 and as a consequence the interface with the other austenite grain γ_2 will be incoherent. The next phase nucleates when the surrounding austenite has been depleted/saturated of carbon. The new phase nucleates adjacent to the first phase and forms the same type of interfaces with γ_1 and γ_2 as the first phase. In addition, this phase also forms an orientation relationship with the initial phase. The nucleation process of pearlite is continued by sideways growth along the austenite grain boundary and by edgewise growth into the austenite grain. The growth of pearlite is cooperative and this takes some time to be established which corresponds to the incubation time of pearlite transformation. There are other ways pearlite can grow but the explanation given above corresponds to the main principles [19]

2.8.2 Nucleation Rate and Growth Rate of Pearlite

The growth (G) and nucleation (N) rate of pearlite nodules governs the transformation rate of pearlite. The temperature interval where pearlite can form is depicted

in an isothermal transformation diagram (TTT-diagram). The transformation rate i.e the rate of N and G, increases with decreasing temperature. Another factor influencing nucleation and growth rate is plastic deformation. Plastic deformation increases the number of nucleation sites as well as introduces vacancies which increases diffusion. The ratio N/G governs the size of the pearlite nodules. A small ratio results in large nodules and a large ratio result in small nodules [21].

2.9 Spheroidization of Pearlite

Spheroidized structures are characterized by spherical cementite particles embedded in a ferrite matrix [22]. In steels, this is the most thermodynamically stable structure because of the low interfacial energy associated with the spherical particles. The driving force for spheroidization is the reduction of interfacial energy and will therefore occur in any prior microstructure [20]. Since the process is diffusion controlled, the rate increases as the temperature increases. The spheroidization rate of undeformed pearlite is slow [22]. When pearlite is exposed to high temperatures the lamellae starts to break up and coarsen, this is known to cause softening through the change in morphology [1].

There are three major models proposed for the spheroidization mechanism namely: Rayleigh's capillarity induced perturbation theory, grain boundary thermal groove theory, and fault migration theory [23]. The fault migration theory is thought to be the main mechanism during static annealing of undeformed pearlite according to [23]. The theory describes spheriodization as a process which initiates at lamellae faults e.g kinks, striations, and holes which are formed during the transformation from austenite to pearlite. The principal idea is that a chemical potential gradient develops between the flat cementite plates and the curved faults. The chemical potential gradient provides the driving force for the lamellae break up which can be explained through the Gibbs-Thomson effect [23].

Cold work and concurrent hot deformation increases the rate of spheroidization. Previous studies have shown that during cold work of pearlite, cementite lamellae will to some extent fracture and step bands can be developed. These induced defects are thought to initiate spheroidization. Furthermore, it is believed that the excess of vacancies, generated during concurrent deformation, increases the rate of spheroidization by increasing the diffusion rate of carbon and iron [24].

2.10 Dislocation Theory

Dislocations are line defects which exist in all polycrystalline materials. The presence of dislocations allow polycrystalline metals to deform at stresses order of magnitude lower than the theoretical shear strength [25]. Crystalline materials generally deform plastically by slip (shear) when a sufficiently high load is applied to the material [1, 26]. Slip is produced by the movement of dislocations in specific crystallographic planes called slip planes and in specific direction on the slip plane. The number and orientation of the slip planes depend on the crystal structure. Generally, slip planes are those planes of a crystal that are most closed-packed or closely packed.

Similarly, the direction of slip on a certain slip plane is most likely the direction where the atoms are most closely packed [27].

The movement of dislocations is limited by the presence of various obstacles within the material. These obstacles governs the flow stress of the material. The obstacles for dislocation motion can be divided into two categories: thermal and athermal obstacles [28]. Thermal obstacles such as solute atoms, interstitials and vacancies, induce short range order stresses which dislocations can overcome by thermal activation [29]. Lattice friction (Peierl-Nabarro stress) can also be considered as a thermal obstacle [30] and for BCC metals e.g iron this is the main obstacle for dislocation motion at low temperatures [31]. However, athermal obstacles such as dislocation pile-ups, precipitates and grain boundaries induce long range order stresses which are too strong to be overcome by thermal activation [29].

Dislocation velocity as a function of temperature and applied stress can be divided into two regions. In the first region there is an increase in velocity as the temperature increases. Dislocations within this region are limited by thermal obstacles which explains the temperature dependence above. In the second region the relation between velocity and temperature is reversed and the velocity decreases with increased temperature[32].

2.11 Strengthening Mechanisms

The following section describes the general strengthening mechanisms used for enhancing the mechanical properties of materials. It ends with describing the general strengthening mechanisms that yield the strength of super strong steels with pearlitic microstructure.

2.11.1 General Strengthening Mechanisms

Strengthening refers to mechanisms that hinder the movement of dislocations and as a consequence making the material stronger [25]. There are several ways to strengthen a material but only those involved in this particular steel will be explained.

Work Hardening

Work hardening refers to the progressive increase of stress necessary to deform a material during plastic deformation [33]. There are several theories which describes the mechanism of work hardening, and all are based on the assumption that dislocation movement becomes more difficult with increased plastic strain [21]. The principal idea of work hardening was postulated by Taylor and is still used in modern theories [31]. The principle is based on the assumption that dislocations get tangled and generates an internal stress which impedes the movement of other dislocations [21]. The entanglement is a result of the increased dislocation density during plastic deformation. The overall effect of work hardening is an increase in strength on the expense of ductility [33].

Grain Boundary Strengthening

Polycrystalline materials consists of grains with different orientations relative to each other. The regions between the grains are called grain boundaries. Grain boundaries act as obstacles to dislocation movement because slip is interrupted due to the different grain orientations [25]. The relationship between the yield stress and grain size is commonly described by the Hall-Petch equation which is based on experimental observations, see equation 2.11. This equation is an approximation and is valid for a limited range of grain sizes [31].

$$\sigma = \sigma_0 + \frac{k}{\sqrt{d}} \tag{2.11}$$

Several mechanisms with different approaches have been proposed in order to explain the grain size effect. Hall and Petch suggested that a Frank-Read source was operating inside the grain and that the generated dislocations piled up at the grain boundary. It was thought that dislocations could cross the grain boundary if the stress ahead of the pile up reached a critical value. The stress ahead of a dislocation pile up was considered to be proportional to the number of dislocations in the pile up. The smaller the grain size the lower amount of dislocations. This means that the stress becomes smaller and a higher external load is required to initiate yielding compared to larger grain sizes [31, 34]. However, Cottrell realized that dislocations cannot cross the grain boundary. Instead he proposed that the stress generated by the dislocation pile up would activate a Frank-Read source in a neighbouring grain when the stress reached a critical value [31].

J.C.M. Li suggested another approach in order to explain the grain size effect. Li considered that dislocations are generated by grain boundary ledges and emitted into the grains [31]. According to Li, dislocation forests are generated near the grain boundaries and the onset of yielding corresponds to the stress necessary to move the dislocations through these forests of dislocations [25, 31, 34]. Furthermore, in a more recent review study by [34] it was concluded that Frank-read sources are absent during deformation of polycrystalline metals and alloys. Instead grain boundary ledges and related interfacial ledges have been proposed to be the dominating dislocation source during deformation [34].

Solid Solution Strengthening

Dislocations can move relatively easily in pure metals and by alloying (solid solution) dislocation movement becomes more limited [31]. Solid solutions refers to an alloy where the parent lattice contains foreign atoms which can either be interstitial or substitutional. These atoms cause local internal stress fields in the matrix which impede dislocation movement. The amount of increased strength mainly depends on the solute concentration and the size difference [25].

Texture Strengthening

During plastic deformation of a polycrystalline material the randomly oriented grains will at large strain rotate and align themselves in a preferred direction. This makes the materials anisotropic i.e. their properties depend on the orientation of the grains [31].

2.11.2 Strength of Pearlite

The strength of pearlite depends on several strengthening mechanisms and will be discussed in following section.

Yield Stress

According to Dollar and Bernstein [35] the yield strength of pearlite corresponds to the stress required to move dislocations in ferrite between two cementite plates. This stress level increases as the interlamellar spacing decreases. The effect of decreasing the interlamellar spacing is to reduce the slip distance. Their theory is based on the assumption that dislocation sources are activated at the cementite-ferrite interface [35].

The yield strength and hardness of eutectoid steels have generally been observed to follow a Hall-Petch relation with respect to interlamellar spacing. The Hall-Petch relation is described in equation (2.12) where σ_0 is the lattice frictional stress in the ferrite, k represents the hardening due to dislocation locking under continuous yielding and λ is the interlamellar spacing [36].

$$\sigma = \sigma_0 \frac{k}{\sqrt{\lambda}} \tag{2.12}$$

Ultimate Tensile Strength

The mechanisms behind the high work hardening rate of pearlite have been widely discussed in the literature and several explanations have been suggested [37, 38].

Zhang et al. [37] proposed three strengthening mechanisms for pearlitic cold drawn steel, namely: grain boundary strengthening, dislocation strengthening, and solid solution hardening. The proposed mechanisms were based on previous studies where it has been reported that interlamellar spacing decreases during wire drawing and that a high dislocation density is generated in the ferrite. Further, it was also reported that cementite can decompose at large strains leading to carbon enrichment in the ferrite lamellae. The principal ideas for the mechanisms proposed in the article is explained below [37].

Grain boundary strengthening was based on the assumption that cementite lamellae can impede dislocations by acting as barriers. Where the onset of yielding was based on the stress generated by dislocation pile ups. The closer the interlamellar spacing the more barriers to dislocation glide and therefore higher strength. In the second strengthening mechanisms, dislocation strengthening, it was assumed that dislocations increases the strength through dislocation entanglement. Lastly, it was

thought that cementite decomposition could enrich the ferrite at large strains leading to solid solution strengthening [37].

The authors of [37] have proposed an equation which is based on the assumption that the strengthening mechanisms are linearly additive. The sum of the individual strength contributions showed good agreement with the experimental results. The following equation was used by the authors to describe the flow stress:

$$\sigma(\epsilon) = \sigma_0 + \sigma(b) + \sigma(\rho) + \sigma(ss) \tag{2.13}$$

where $\sigma(\epsilon)$ represents the flow stress at a given strain, σ_0 the frictional stress for pure ferrite, $\sigma(b)$ the boundary strength, $\sigma(\rho)$ the dislocation strength and $\sigma(ss)$ the solid solution strength [37].

2.12 Static and Dynamic Strain Ageing

Solute atoms can segregate to dislocations and impede their movement. This phenomenon is called strain ageing and is both time and temperature dependent. There are two types of strain ageing, static and dynamic. Static strain ageing occurs after a steel has been plastically strained, unloaded, and then aged. This leads to an increased yield and tensile strength, and decreased ductility upon reloading. Dynamic strain ageing occurs at higher temperatures concurrent with plastic deformation during cyclic or monotonic testing [1]. The main result of dynamic strain ageing is an increase in work-hardening rate and tensile strength [31]. Furthermore, the stress-strain curves can become serrated when dynamic strain ageing is present and this effect is sometimes referred to as the Portevin-Le Chatelier effect [33].

Hardening due to dynamic strain ageing was observed during low cycle fatigue tests conducted on pearlitic railway wheel steels at temperatures around 300° [1].

2.13 Swift Effect During Pure Torsion

Swift effect is a phenomenon which occurs due to plastic axial strains which occur in metallic cylindrical specimens when they are subjected to free-end-torsion. Torsional loading causes the material to strain harden and generate axial plastic strain which causes the material to plastically elongate. The swift effect is explained to be due to a texture induced anisotropy [39].

2.14 Effect of Strain Rate and Temperature

Both strain rate and temperature have a large influence on the mechanical properties of rail steels. Generally the flow stress increases with increased strain rate and decreases with increased temperature. Plastic deformation with high strain rates could cause adiabatic conditions which lead to softening. Adiabatic conditions cause a locally increased temperature due to heat generated by the excess energy from the plastic deformation [40].

2.15   Static and Dynamic Recovery

Recovery is a process in which the distribution and density of crystal defects in strained material changes without affecting the shape and orientation of the grains. Recovery is mainly attributed to the rearrangement and annihilation of dislocations which reduces the strain energy of the system [21, 33]. Recovery can either be static or dynamic and the principal difference is that static recovery occurs after deformation and dynamic recovery during deformation at elevated temperatures. The rate of recovery is strain and temperature dependent, it increases with higher temperature and deformation [41]. Furthermore, dynamic recovery leads to softening of the material and is besides the temperature dependent on the strain rate [42].

2.16   Induction Heating

Materials that are electrically conductive can be heated by electromagnetic induction which is referred to as induction heating. This is a technique that can be used for heat treating materials. The induction heater consists of an induction coil through which an alternating voltage is applied. This generates an alternating current which produces an alternating magnetic field which in turn generates eddy currents within in the material. Heat is then generated by the eddy currents through the Joule effect, see equation 2.14, where P is the power, I the current and R the electrical resistance [43].

$$P \propto I^2 * R \qquad (2.14)$$

An important material property regarding induction heating is the electrical resistivity which is the reciprocal of electrical conductivity. The electrical resistivity is a measure of the materials resistance to current flow. Electrical resistivity is a material dependent property and is affected by factors such as temperature, grain size, and plastic deformation. Regarding plastic deformation of ferritic-pearlitic rail wheel (grade R7), Eifler et al. [44, 45] showed that the electrical resistivity increased with plastic deformation. It was reported that this increase was primarily attributed to the increased dislocation density.

The induction system is affected by the electrical resistivity which affects the temperature distribution and the depth of heat generation [43]. The major advantage with induction heating is that it is able to heat a material quickly. A drawback with induction heating is that it creates a temperature gradient through the material. This effect is called skin effect and occur due to the decrease of current towards the center of the material being heated [43].

2.17   Thermal Conductivity and Conduction

Thermal conductivity (k) is a thermal property of materials which describes how fast heat moves in a material. The temperature distribution within the material becomes more uniform as the thermal conductivity of the material increases [43].

The well known Fourier´s law is used for describing how heat travels from high to low temperature-regions, see equation 2.15, where q is the heat flux, k the thermal conductivity and T the temperature [43].

$$q = -k\,grad(T) \tag{2.15}$$

3
Method

Chapter 3 begins with presenting the material and test bar geometry. It continues with presenting the experimental procedure used for the attempt to produce test bars with a microstructure similar to the one found in the surface layer of fully pearlitic rail steels. Thereafter, sample preparation is described. The chapter ends with presenting the methods used to characterize the microstructure.

3.1 Material and Test Bar Geometry

The steel studied in this project was a R260 grade rail steel which follows the standard EN 13674-1. The general material properties are shown in table 3.1 [46].

Table 3.1: General material properties for R260

Material	Microstructure	Hardness	Yield Stress	Tensile Strength
Steel	Pearlitic	260-300HB	600 MPa	900 MPa

The microstructure of the R260 rail steel is fully pearlitic and has an interlamellar spacing around 230 nm. The chemical composition for the material is shown in table 3.2 [46].

Table 3.2: Chemical composition of R260 steel in wt %

	C	Si	Mn	S	Cr	Cu	V	P	Al	N	Fe
R260	0.72	0.31	1.04	0.01	0.02	0.018	<0.005	0.006	<0.002	0.006	Bal

The material for the biaxial testing were extracted as solid cylinders from virgin rail heads, see figure 3.1. The geometry of the test bars is shown in figure 3.2.
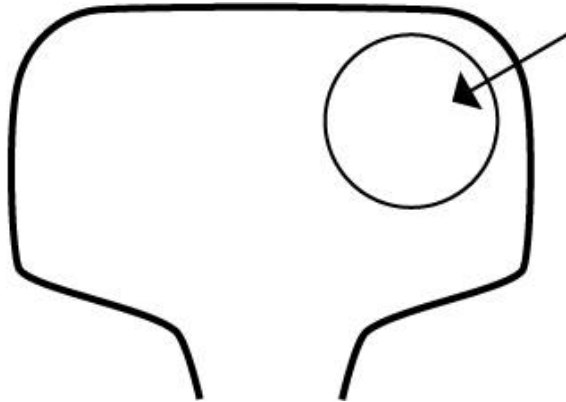
Figure 3.1: Location of material extraction in the rail head
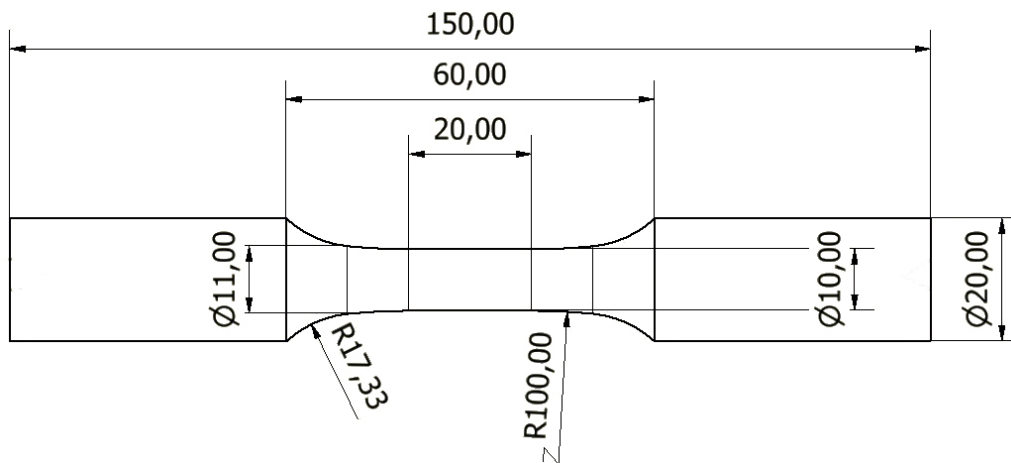
Figure 3.2: Geometry of the test bar used in biaxial testing

3.2 Experimental Procedure

The section experimental procedure begins with presenting which parameters that were used for biaxial testing and how these parameters were selected. It continues with describing how the heat treatment of undeformed rail steel was designed. The section ends with describing the equipment and how the tests were conducted.

3.2.1 Process Parameters

The process parameters were limited to test bar geometry, axial compressive load, temperature, twist rate, monotonic, and cyclic twisting.

3.2.2 Design Approach

The approach for the design of the tests was based on an iterative procedure, illustrated in figure 3.3. The results from each test were analyzed in order to conclude which changes in the process parameters that should be made in order to maximize the objective i.e. increase the accumulated shear strain.
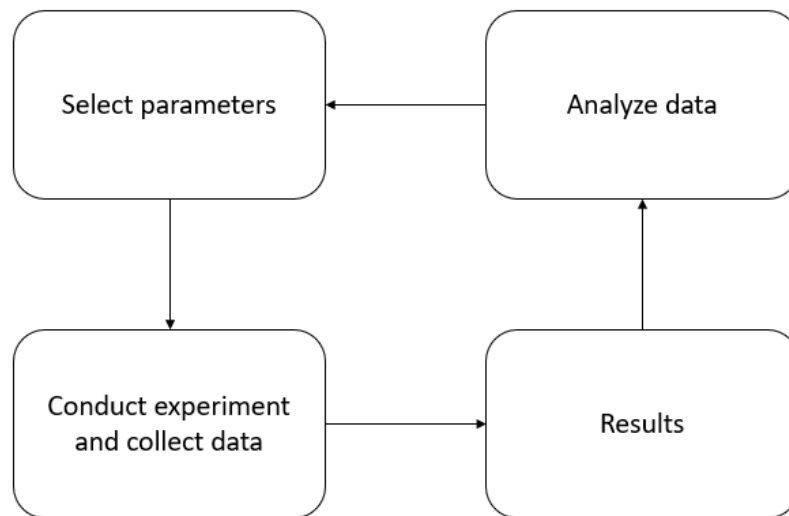
Figure 3.3: Flow chart of the iterative process

3.2.3   Parameter Values for Experiments 1-7

Table 3.3 below describes how each test was conducted and which parameters were used. As described previously the parameter selection was an iterative process involving conducting the tests, collecting data, and analyzing data. The temperature selection was based on previous work [47], where severe spheriodization was observed at temperatures above 500 °C and dynamic strain ageing at temperatures around 300 °C. These temperatures were used as an upper and lower limit and a temperature in between was therefore selected as a starting point. The selection of nominal axial compressive stress and twist rate was also based on previous work [6], which used the same predeformation method but at room temperature for the nominal axial compressive stresses 0, -250, and -500 MPa and twist rate of 1.5°/s. This selection was made in order to get a good comparison with the predeformation method conducted at room temperature.

Table 3.3: Detailed description of all parameters for each test

Test	Twist	Twist increment [°]	Time [s]	Heat	Temp [°C]	Axial comp.stress [MPa]
1	Monotonic	90	60	Constant.Temp	400	-500
2	Monotonic	90	60	Constant.Temp	400	0
3	Monotonic	90	60	Constant.Temp	400	-250
4	Monotonic	90	60	Annealing in between twists	400	-250
5	Monotonic	90	60	Constant.Temp	350	-250
6	Monotonic	90	60	Constant.Temp	350	-350
7	Monotonic	90	60	Constant.Temp	300	-500

3.2.4   Heat Treatment

In addition to the thermomechanical testing, a separate heat treatment was performed on undeformed material. It was done to investigate how the temperature solely affects the microstructure of the steel. In total three samples were prepared, two samples were heat treated and the third sample was used as a reference. The heat treatment used the same working conditions as the thermomechanical testing for test 3 and 6 since they achieved highest amount of deformation at respective temperature. The heat treatment was conducted in an air atmosphere at 350 and 400°C during 50 and 40 minutes which corresponds to test 6 and 3 respectively.

All samples were taken around the same location at the grip section of an undeformed test bar. The samples were later prepared and characterized with optical microscopy, scanning electron microscopy and hardness test.

3.2.5   Biaxial Testing Machine and Software

The tests were conducted with MTS Model 809 axial/torsional test system. Two programs were used in order to conduct the tests. In the station manager (control program) the machine could be manually controlled and all measured values were displayed. The second software was Multipurpose Elite in which the deformation programs described in the next section was created.

3.2.6 Program for Thermomechanical Testing

The following section describes the two methods used to deform and heat treat the test bars.

Deformation Program: Constant Temperature

The deformation program with constant temperature was used for all the tests except test 4. An illustration of the program sequence is shown in figure 3.4. The program starts with resetting torque and axial force to zero. The induction coil then starts to heat up the test bar to the specified temperature during 180 seconds followed by a dwell time of 20 seconds to allow the temperature to stabilize. Axial displacement is then offset to zero so that displacement is measured from the expanded state. The program will thereafter ramp up the axial load to the specified value and then rotate the test bar 90° in 60 seconds. Before the test bar is rotated back to the initial position by manually releasing the lower grip, axial force and torque are automatically relaxed. The test bar is then re-gripped manually at the starting position and this procedure is repeated until failure or until the stop criterion is reached. In order to protect the machine from being damaged during testing a limit of -12 mm in axial displacement was set as a stop criterion.
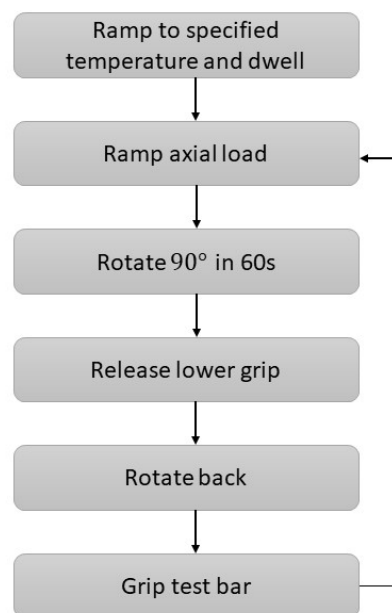
Figure 3.4: Deformation program: Constant temperature

Heating in Between Twists

The deformation program with heating in between twists was used for test 4 and is nearly identical with the program for constant heating. An illustration of the program sequence is shown in figure 3.5. The only differences is that deformation is conducted at room temperature and that a heat treatment is applied at the end of the twisting cycle after the loads have been relaxed. The heat treatment consist of heating the test bar to the specified temperature followed by a dwell time of 20 seconds. Thereafter the test bar is air cooled.
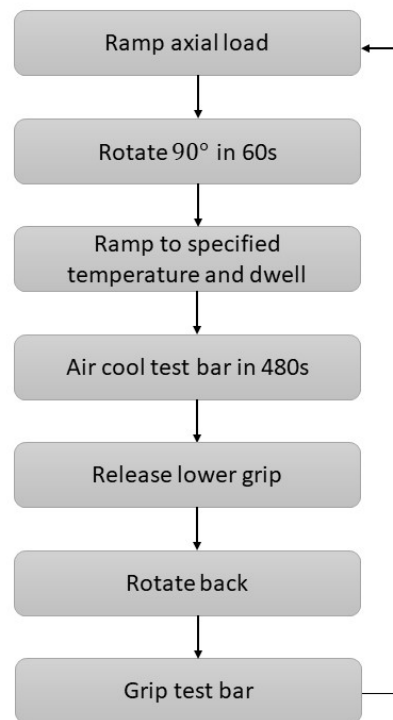
Figure 3.5: Deformation program: Heating in between twists

3.2.7 Setup of the Equipment

Two thermocouples were used, one was welded at the transition curvature on the upper part of the test bar and the other was looped around the gauge section of the bar. The specified temperature was controlled by using the looped thermocouple as input values for the control unit. The welded thermocouple was used in case the looped thermocouple would break. In that case, the program would still be able to be continued. Furthermore, the test was in the control program, programmed to stop if the temperature measured by the welded thermocouple exceeded 100 °C from its stabilized temperature. Furthermore, the control program was set to indicate if the temperature of the looped thermocouple exceeded 100 °C from its specified value. Indicate was used in order to be able to adjust the power during the test. In total, three different looped thermocouples had to be used for the tests, one for test 1-4, another for test 5 and a new one for test 6-7.

The induction coil was set to 1 kW power and was centered at the middle of the test bar. Furthermore, two heat shields made of copper were used to protect the machine grips. The large servohydraulic pump of the test rig was used to deliver the pressure and torque via the actuator. No extensometer was used. Figure 3.6 illustrates the setup of the equipment for the thermomechanical testing.
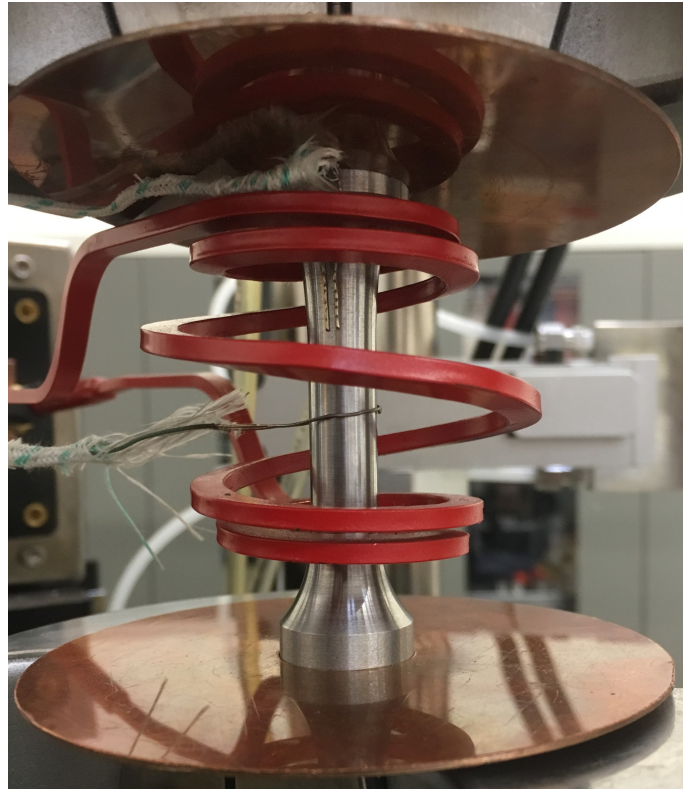
Figure 3.6: Setup of the equipment for the thermomechanical testing

3.3 Sample Preparation

Sample preparation was required for characterizing the material with scanning electron microscopy, optical microscopy, and hardness testing. Each preparation step can generate artifacts which can mislead the results. In order to analyze the steel properly it is therefore essential to use a preparation method that minimizes the material alteration. As guidance for this, Struers preparation methods was used, which means that the preparation results must be reproducible [48]. The sample preparation was performed in the sequence: cutting, mounting, mechanical preparations and etching.

Two types of samples were cut out from each test bar, see figure 3.7. The first sample was used to measure the shear strain and characterize the microstructure. This sample was taken from the radial direction for each test bar and is termed flowline sample in the report. The second sample was used for hardness testing which was measured in the axial direction and is termed hardness sample.
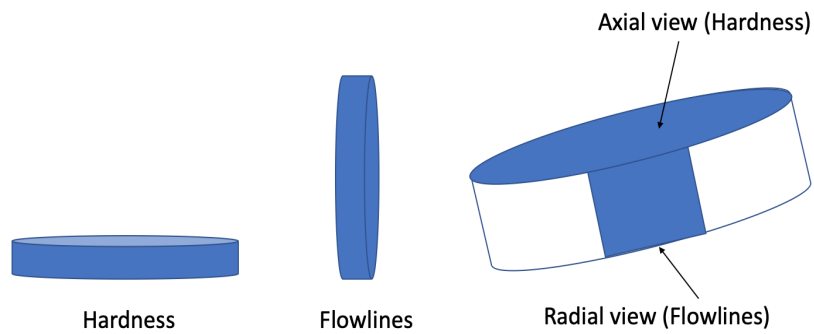
Figure 3.7: Illustration of hardness and flowlines samples.

The heat treatment samples were prepared according to figure 3.8 where the radial cross-section was the area of interest.
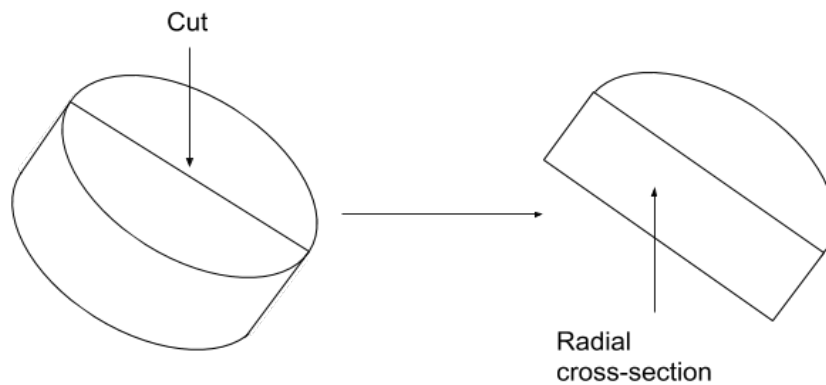
Figure 3.8: Preparation of heat treatment samples

3.3.1 Cutting

Abrasive wet cutting was used as cutting method. Two different cutting machines were used, one with rough precision and one with fine precision. The machine Struers Discotom-2 with rough precision was used for sectioning the test bar into two pieces of suitable length, since the test bar was too large to be handled in the precision machine (ISOMET 2000), see figure 3.9. The fine precision machine was used for cutting out the samples with a thickness about 2 mm.
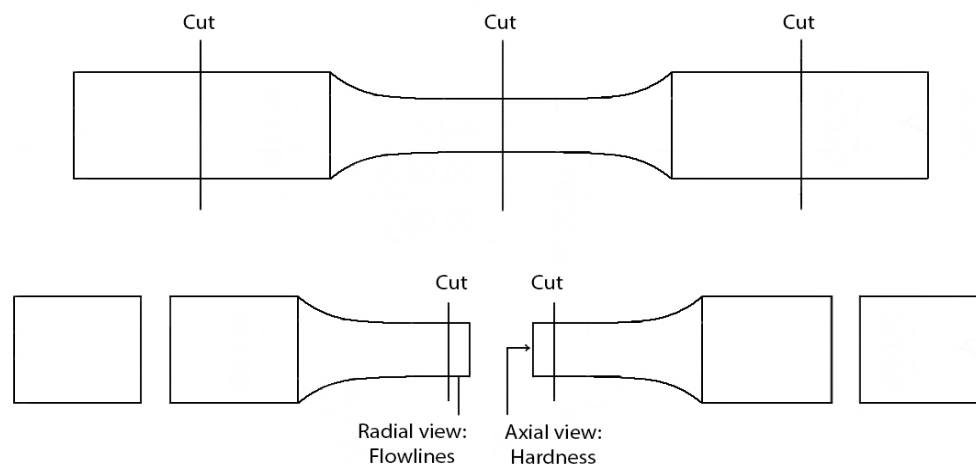
Figure 3.9: Sectioning of test bar and sample cut

The rough precision machine was manually operated and the cut-off wheel, grade 50A25, was fed forward with a speed that only gave minor sparking. The precision machine was automatically controlled and the load and speed was set to 4.5N and 3500 rpm respectively. The cut-off wheel used in the fine precision machines was 30A13 which has aluminum oxide as abrasive.

Two samples, one for hardness and one for flowlines were cut out for each test. The samples were cut out from thickest part of the gauge section where the amount of deformation should be highest.

3.3.2 Mounting

All samples were hot mounted in Struers CitoPress-20 with a polyfast resin. The process parameters were set according to the Struers selection guide for hot mounting which were: 20 ml polyfast resin heated at 180 °C under a pressure of 250 bar for 3.5 minutes followed by 1.5 minutes cooling at high rate. This resin is conductive and allows the samples to be examined in SEM.

3.3.3 Grinding

Grinding was conducted in two steps, (1) plane grinding and (2) fine grinding with Struers grinding and polishing machine (TegraPol-31+Tegraforce-5). Plane grinding used silicon carbide sandpaper and fine grinding used diamond suspension. The settings used for plane and fine grinding are shown in table 3.4 and 3.5 respectively.

Table 3.4: Settings for grinding hardness samples

	Disk/Cloth	Time [min]	Foce [N]	Speed [rpm]	Abrasive
Plane grinding	Sandpaper	1	20	300/150	SiC, 500 µm
Fine grinding	MD-Allegro	7	35	150/150	Diamond suspension 9 µm

Table 3.5: Settings for grinding flowline samples

	Disk/cloth	Time [min]	Force [N]	Speed [rpm]	Abrasive
Plane grinding	Sandpaper	1.5	20	300/150	SiC, 500 µm
Fine grinding	MD-Allegro	1	35	150/150	Diamond suspension 9 µm

3.3.4   Polishing

Polishing was conducted in two steps with Struers grinding and polishing machine (TegraPol-31+Tegraforce-5). The first polishing step used a diamond suspension with a particle size of 3 µm The second polishing step used a diamond suspension with a particle size of 1 µm. The polishing settings used for hardness samples and flowlines samples are shown in table 3.6 and 3.7.

Table 3.6: Polishing settings for hardness samples

Disk/cloth	Time [min]	Force [N]	Speed [rpm]	Abrasive
MD-Mol	5	35	150/150	Diamond suspension 3 µm
MD-Nap	3	25	150/150	Diamond suspension 1 µm

Table 3.7: Polishing settings for flowlines samples

Disk/cloth	Time [min]	Force [N]	Speed [rpm]	Abrasive
MD-Mol	3	35	150/150	Diamond suspension 3 µm
MD-Nap	2	25	150/150	Diamond suspension 1 µm

3.3.5   Etching

The samples were chemically etched with a 3% nital etch, which is a solution of 97% ethanol, and 3% nitric acid. Etching was performed by immersing the samples in the etch, cleaning with ethanol and drying the samples. The procedure was repeated until a good contrast was achieved.

3.4 Microstructural Characterization

The following section describes the microstructural characterization. It includes the methods for evaluation of hardness gradient, shear strain measurement and evaluation of the lamellae structure using SEM imaging.

3.4.1 Evaluation of Hardness Gradient

Hardness was evaluated with Vickers hardness method and the equipment used for the hardness test was Struers hardness testing machine (Durascan-70 G5). The load was set to 10 kgf (HV10) and the indent was measured with a 20x objective lens.

Two samples, hardness and flowline, from each test bar was used for the hardness measurements. Hardness for the flowline and hardness samples were measured in radial and axial direction respectively. The indent pattern for the prepared hardness samples is illustrated in 3.10. The indent pattern for hardness measurement of the heat treatment samples and flowlines samples are illustrated in figure 3.11.
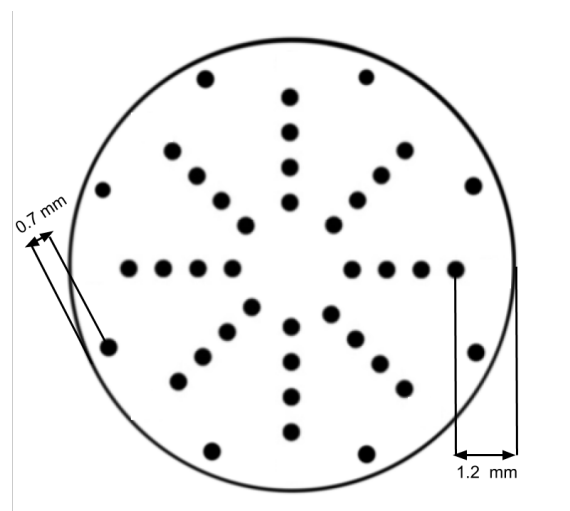
Figure 3.10: Indent pattern for hardness samples
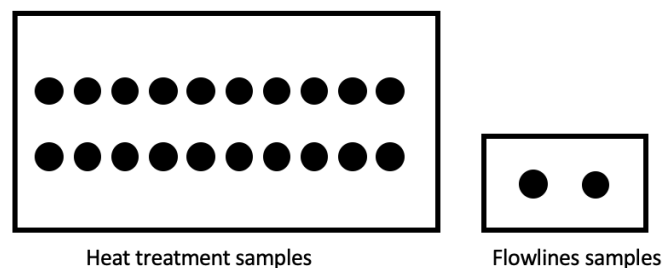
Figure 3.11: Indent pattern for heat treatment and flowlines samples

The number of indents per sample is listed in table 3.8. The number of indents for the hardness samples became a function of the diameter. The spacing from the edge and between the indents were 0.7 mm and 1mm respectively. The spacing was chosen according to the standard ISO 6507.

Table 3.8: Number of indents per sample

Sample	Number of indents
Hardness	40-50
Flowlines	2-3
Heat treatment	20

3.4.2 Shear Strain Measurement of Flowline Samples

Strain is usually measured with an extensometer. However, this method was not possible to use due to the large amount of twisting and high temperature. Therefore, a method which has been proven to give a good estimation of the accumulated shear strain in rail steels was used [49]. This method requires optical micrographs taken close to the surface layer and for this a 10x objective lens was used. Shear strain was calculated by equation 3.1 by measuring the angle α between the flowlines and axial direction, see figure 3.12 [49].

$$shear strain = \gamma = tan(\alpha) \tag{3.1}$$
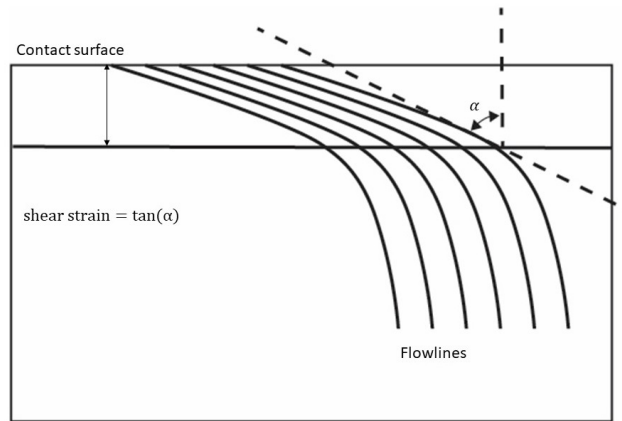
Figure 3.12: Principal of strain measurement

The angle α was measured in two different ways. The first method measured the angle α for ten individual flowlines and the shear strain was calculated by averaging the angles. The second method used a grid consisting of parallel lines. This grid was manually rotated until the flowlines and grid lines obtained the best fit, see figure 3.13. The angle between the grid lines and normal direction gave the average angle α which was used for calculating the average shear strain. The accumulated shear region is very thin, usually 20-30 μm in field samples [49]. The depth of the surface layer in which the flow lines was measured in are presented in appendix A.2.
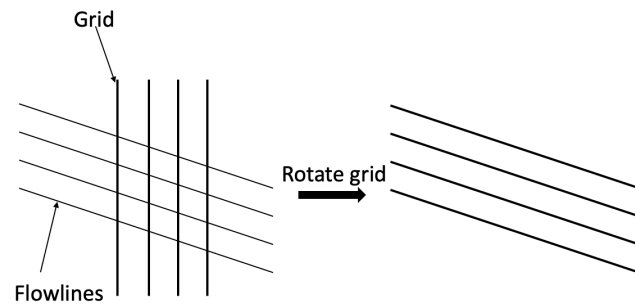
Figure 3.13: Principal of grid method

3.4.3 Depth of Grinding and Polishing

The maximum depth d, below the surface for the flowline samples was calculated by using equations 3.1-3.3. The maximum distance is illustrated in figure 3.14.

$$\phi = \arcsin \frac{b}{r} \tag{3.2}$$

$$h = \frac{b}{\tan \phi} \tag{3.3}$$

$$d = r - h \tag{3.4}$$

Where b = half the sample surface base, r = radius of the sample, h = height from the center of the sample to the middle of the sample surface and d = maximum depth after grinding and polishing.
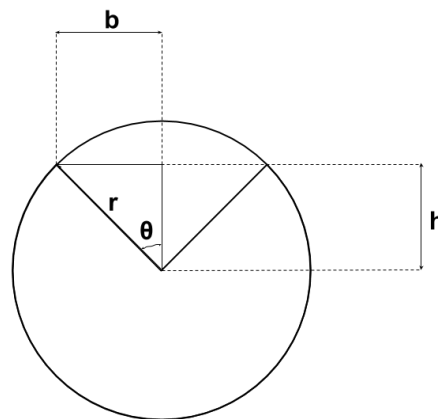
Figure 3.14: Maximum depth of grinding and polishing

3.4.4 Evaluation of the Lamellae Structure

The lamellae structure was evaluated by taking SEM images on several locations for each sample. These were later compared with field samples and undeformed material which were heat-treated and non heat treated. This method was only used to evaluate if the microstructure remains stable or if it starts to break up.

Both SE2 and InLens detectors were used for imaging. Working distance was set to 8.5 mm and acceleration voltage to 15kV. Generally, magnifications between 5k-20k were used to get an overview of the microstructure for each test.

4

Results and Analysis

This chapter presents the results and the analysis of the thermomechanical testing and the material characterization analysis.

4.1 Mechanical Testing at Elevated Temperatures

The results from the thermomechanical testing are included in this section. It begins with describing general results and observations for all tests and continues with presenting the results for each test in sections 4.1.2-4.1.8. The results from each test are plotted in figure 4.1-4.21 where the following results are included: torque response with respect to twisting, how the temperature varies during the test and the length change with respect to rotation. The section ends with a comparison and analysis of all tests, see figure 4.22 and 4.23 in section 4.1.9.

4.1.1 General Results for Tests 1-7

Serrated torque curves ("saw tooth shaped") was observed for all tests (except test 4) and torque increased/decreased in a linear manner between the peaks and valleys of these serrations. The magnitude of the serrations varied between each test and within each test. Furthermore, there was an overall increase in torque for all tests except test 2 where torque decreased throughout the test.

The induction coil was able to keep an average temperature which was close to the selected temperature parameter for each test. In appendix A.3 temperature vs time and torque vs time is plotted for all the tests. The effect of temperature deviations on the torque response is discussed in chapter 5.

Axial displacement with respect to twist is plotted for each test in section 4.1.2-4.1.8 and the regularly spaced spikes in these plots represent the elastic relaxation after each twisting cycle. The length of the test bars decreased in all tests except for test 2 where the length slightly increased. The corresponding change in diameter was measured at three locations according to figure A.1 and the diameter at these locations after each test is listed in table A.1. The diameter was quite uniform over the measured section except for test 1 which buckled. The general results for test 1-7 are summarized in table 4.1.

Table 4.1: General results for test 1-7

Test	Avg.Temp [°C]	SD	Max Torque [Nm]	Max Axial.Disp [mm]	Total Twist [°]
1	396	8	200	-14	800
2	399	3	110	0.6	380
3	398	4	170	-8	1530
4	-	-	180	-1.4	270
5	350	7	200	-4.1	1530
6	347	7	260	-8	1850
7	296	9	230	-4.8	460

4.1.2 Test 1

The test stopped on the ninth twisting cycle at 40° twisting without failure since the stop condition for maximum axial displacement was reached. No cracks where visible on the surface of the test bar after the test was completed. Furthermore, during the first cycle the test stopped at 78° twist because the test was initially programmed to stop if the torque dropped with 2 Nm below the maximum torque level for the current cycle.

During the test, at the beginning of the fifth twisting cycle, the test bar buckled, see appendix A.7.1. The buckling was accompanied by a large temperature drop see figure 4.2. Furthermore, the torque curves was smooth during this temperature drop, see cycle 5-7 in figure 4.1. The temperature drop was later compensated by increasing the max power of the induction heater.
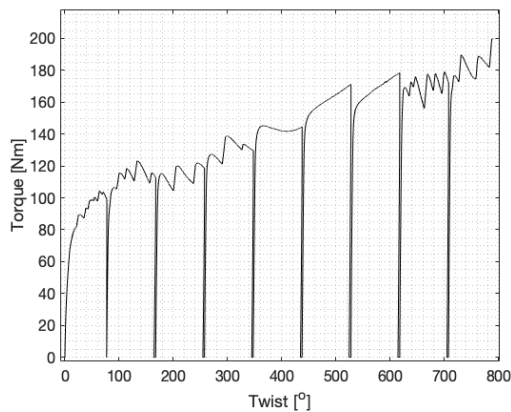
Figure 4.1: Torque vs twist
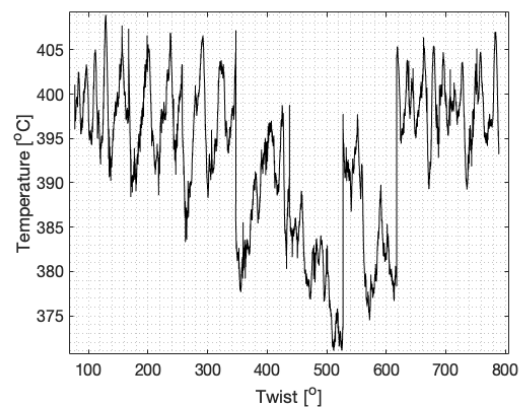
Figure 4.2: Temperature vs twist.
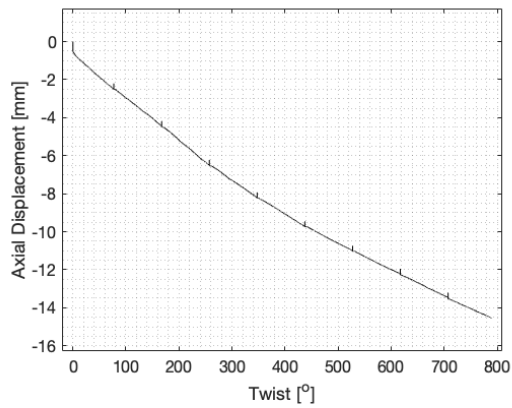
Figure 4.3: Change of specimen length

4.1.3 Test 2

Test 2 completed four twisting cycles and broke at the beginning of the fifth twisting cycle. During the test, around the fourth twisting cycle, small cracks started to appear in the middle of the gauge section. These cracks increased in size during subsequent rotation and at the fifth cycle a large crack appeared in the middle of the gauge section which caused the test bar to break, see appendix A.7.2.
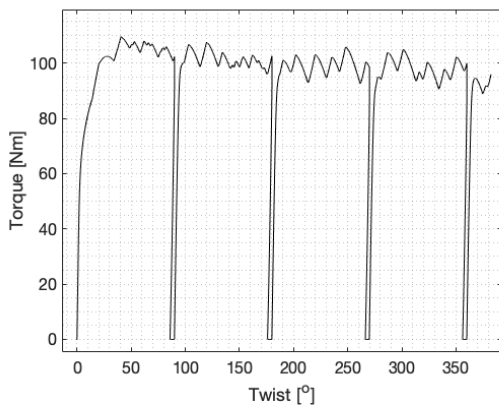
Figure 4.4: Torque vs twist
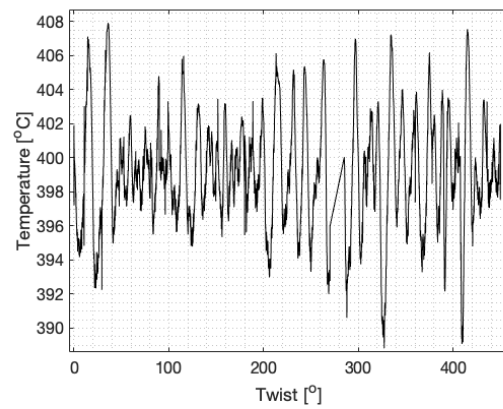
Figure 4.5: Temperature vs twist
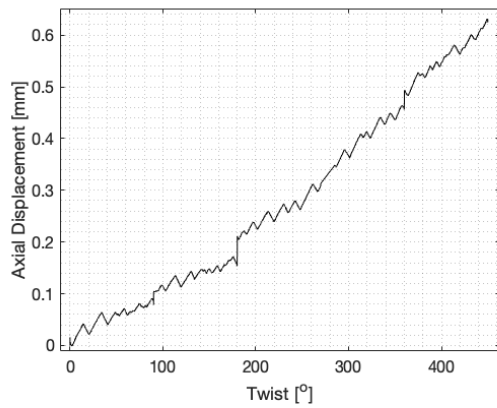
Figure 4.6: Change of specimen length

4.1.4 Test 3

Test 3 stopped at the 18th cycle without failing. It stopped due to that the lower grip got stuck when it was rotating back to the starting position. Although the test bar did not fail, several small cracks could be observed on the surface, see appendix A.7.3. These cracks were located at the center part of the gauge section and started to appear on the surface around the 12th cycle. The torque response was not serrated for twisting cycles 13-16.
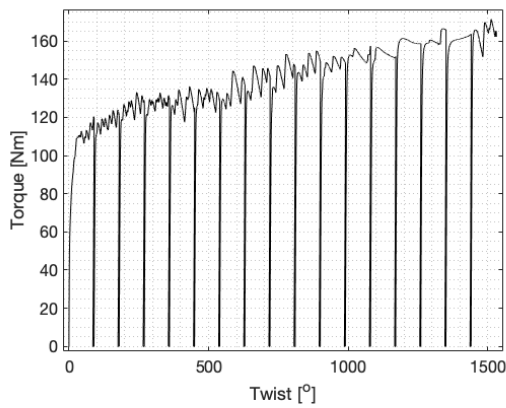
Figure 4.7: Torque vs twist
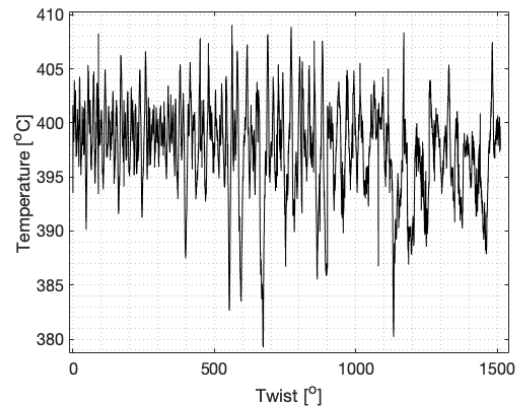
Figure 4.8: Temperature vs twist
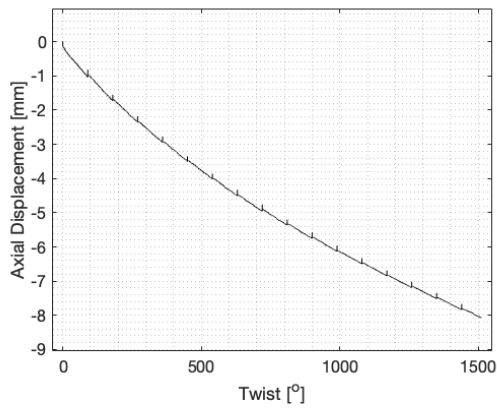
Figure 4.9: Change of specimen length

4.1.5 Test 4

The test bar broke after three cycles. No cracks were visible after the two first cycles and no buckling was observed. The torque increased after each cycle where the work hardening rate was rapid at the beginning of the cycle followed by steady work hardening rate, see figure 4.10. The heat treatment in between the twists is plotted in figure 4.11. The test bar was heated at 400 °C during 20 seconds and then air cooled with a cooling rate of 0.83°C/s.
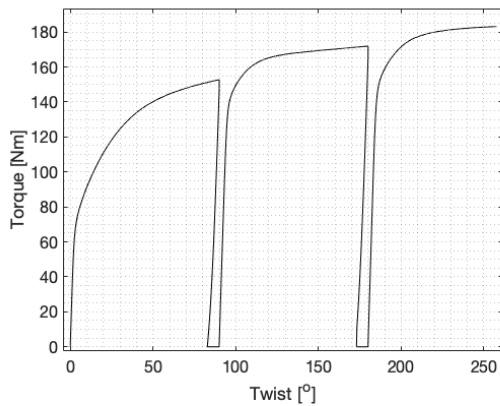
Figure 4.10: Torque vs twist
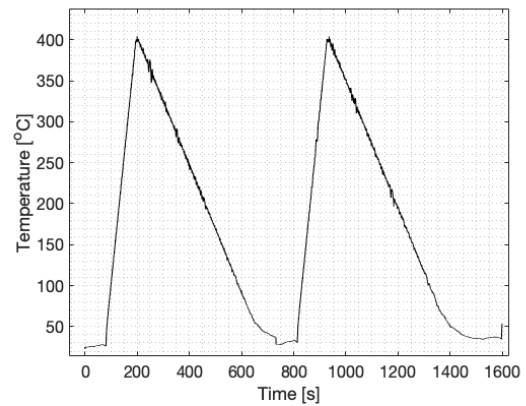
Figure 4.11: Temperature vs time
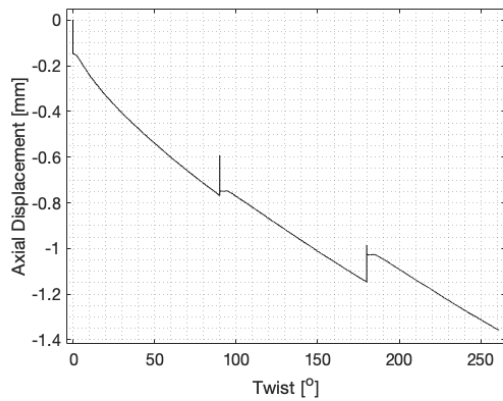
Figure 4.12: Change of specimen length

4.1.6 Test 5

The test bar broke at the beginning of the 18th twisting cycle. During the test a small crack appeared after the eighth twisting cycle, located at the upper part of the gauge section. Two additional cracks was observed at the same location after the 14th cycle and at the 15th cycle several cracks were spread across the gauge section.

The torque response was less serrated compared to test 1-3. The average temperature was 350 °C because of the symmetry of the temperature deviations, see figure 4.14. The temperature deviations was large at the beginning of the test and then continuously decreased.
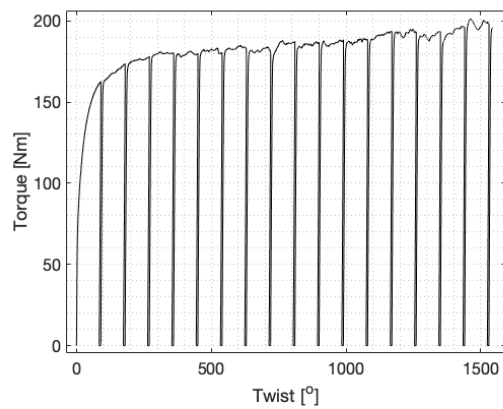
Figure 4.13: Torque vs twist
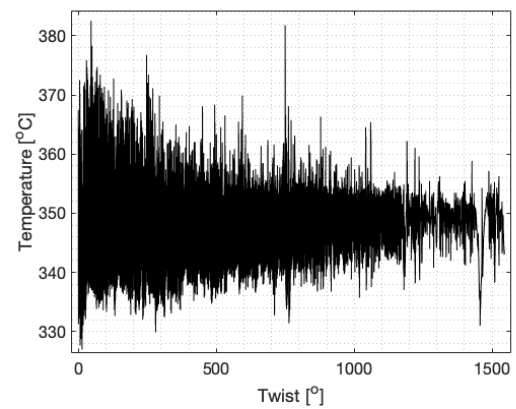
Figure 4.14: Temperature vs twist
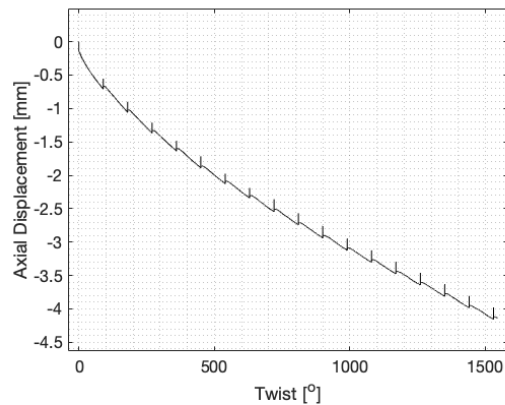
Figure 4.15: Change of specimen length

4.1.7   Test 6

The test bar broke at the beginning of the 22nd twisting cycle. During the test run, a small crack was observed at the 17th twisting cycle and at the 19th cycle additional cracks became visible around the same location. At the 21th cycle cracks started to appear at the bottom of the gauge section and at the 22nd cycle the bar broke.

The temperature fluctuations were quite small up until 90°twisting, they were rather large between 90-600° twisting and continuously decreased after 600° twisting. Furthermore, the magnitude of the torque serrations was larger when the temperature deviations were larger see figure 4.16 and 4.17.
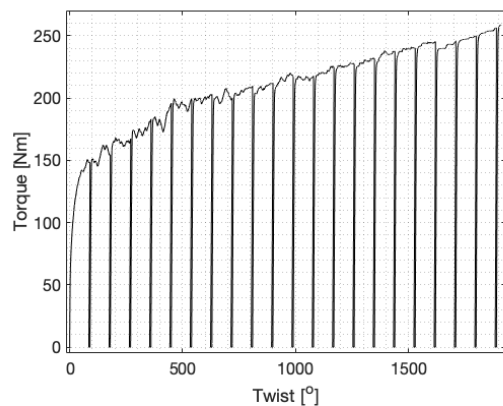
Figure 4.16: Torque vs twist
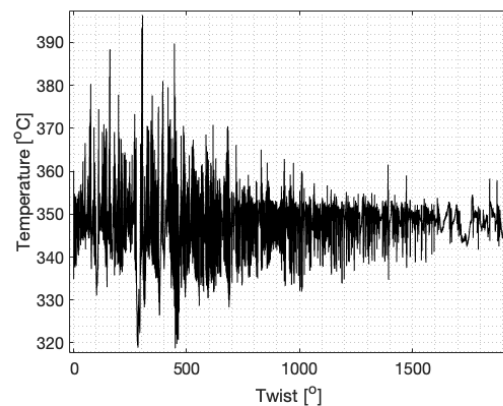
Figure 4.17: Temperature vs twist
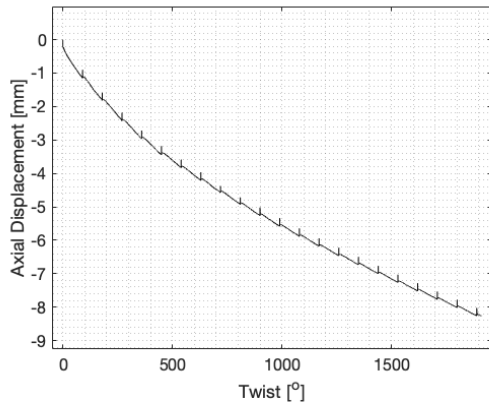
Figure 4.18: Change of specimen length

4.1.8   Test 7

Test 7 completed five twisting cycles and failed at the beginning of the 6th cycle. No cracks were observed during deformation. Torque increased fast during deformation and the torque response was quite smooth for the two first cycles and the temperature deviation during these cycles were low, see figure 4.19 and 4.20. Furthermore, torque increased in a parabolic manner.

The temperature was not stable during the test, see figure 4.20. Up to 160° twist the temperature was quite stable but thereafter the temperature was alternating between low and high temperature deviations.
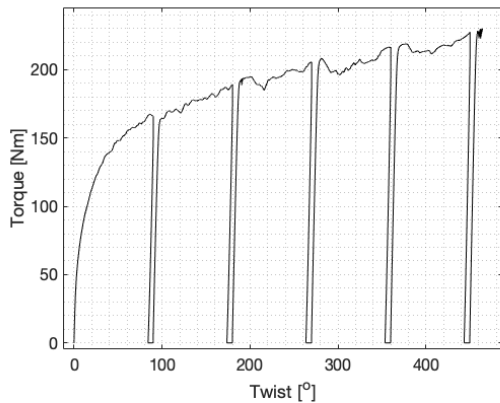
Figure 4.19: Torque vs twist
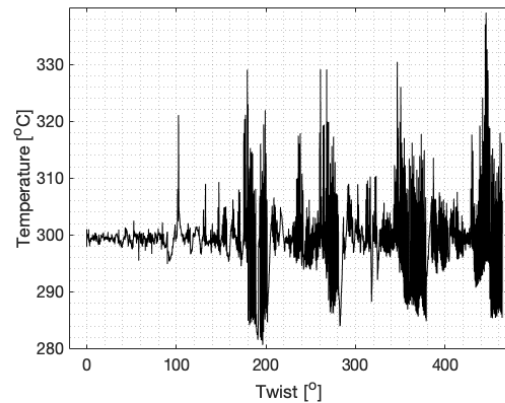
Figure 4.20: Temperature vs time
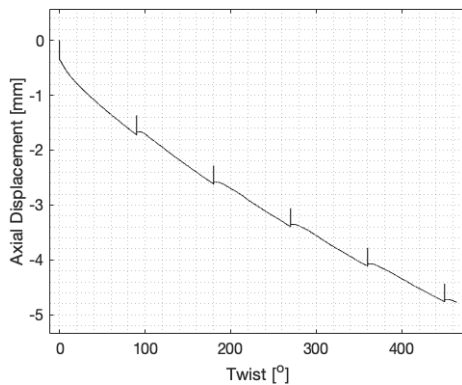
Figure 4.21: Change of specimen length

4.1.9   Comparison and Analysis of All Tests

The torque response with respect to twist angle for all tests is plotted in figure 4.22. The yielding behavior during the first cycle of test 1-3 changes with compression load. For test 2 and 3 yielding occurs at approximately the same torque whilst for test 1 with the highest compression load, yielding starts at a lower torque. Regarding test 5 and 6 the same behavior is observed. Test 6 yields at a lower torque compared to test 5 in which the compression load is lower. Furthermore, compression affects the rate at which torque increases. For test 1-3 the effect of compression is clear. Beginning with test 2 without compression, it is observed that the overall torque is decreased after the first cycle. For test 3 with -250 MPa the overall torque was increased. Regarding test 1 with -500 MPa the increase is considerably higher compared to test 2 and 3. The same effect is also observed for test 5 and 6 where torque in test 6 increases faster than for test 5 which have a lower compression load. In addition, for the test temperature 400 °C and 350 °C the number of cycles increased with compression load except for test 1 which was subjected to buckling.

The influence of compression on torque response is related to axial displacement, see figure 4.23. There it can be seen that an increase in compression load leads to a higher decrease in test bar length which was accompanied with an increase in test bar diameter. It was further observed that the larger the decrease in test bar length per cycle, the higher the torque rate increase becomes. One exception from this behavior was observed for test 7 for which the torque rate increase was the highest but axial displacement per cycle was not the largest.

The influence of temperature on torque response was manifested by comparing the torque response of test 3 with test 5. It was observed that test 3 starts to yield at a lower torque compared to test 5. Furthermore, the length of the test bar in test 3 decreased more per cycle compared to test 5. The overall effect of increasing the temperature from 350 to 400 °C was to decrease the strength of the material. An anomaly was from this behavior was observed when test 7 and 5 was compared with the first cycle of test 4. It was observed that torque for the first cycle of test 5 and 7 was higher than for test 4. It is interesting since there was no difference in axial displacement between test 4 and 5 during the first cycle. Based on the results the material is stronger at 300 °C and 350 °C compared to room temperature.
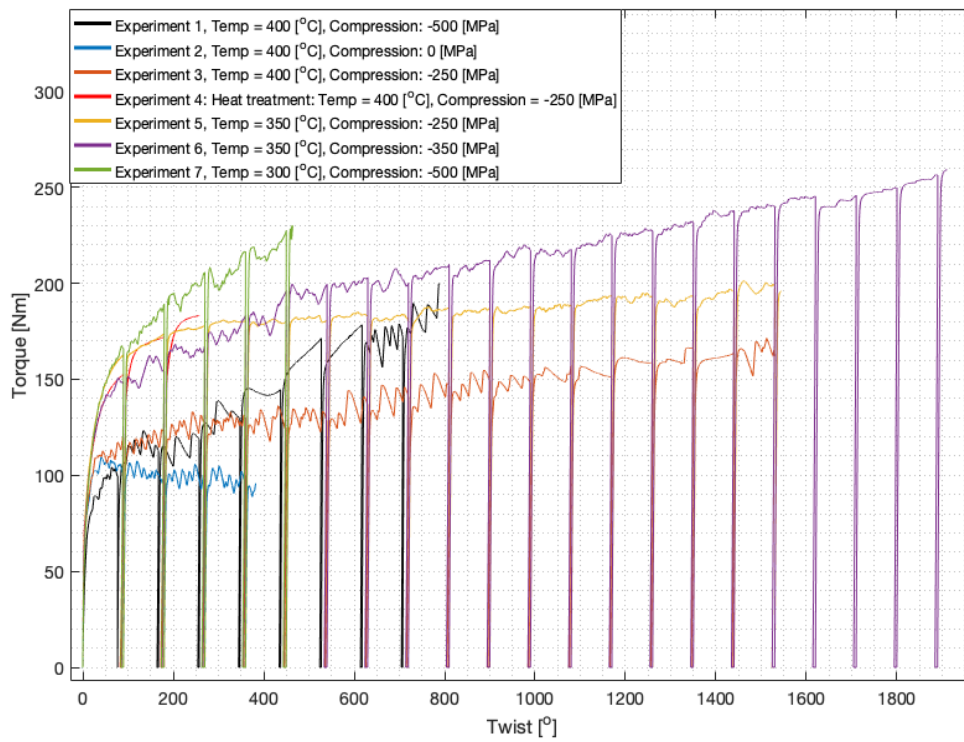
Figure 4.22: Torque vs twist
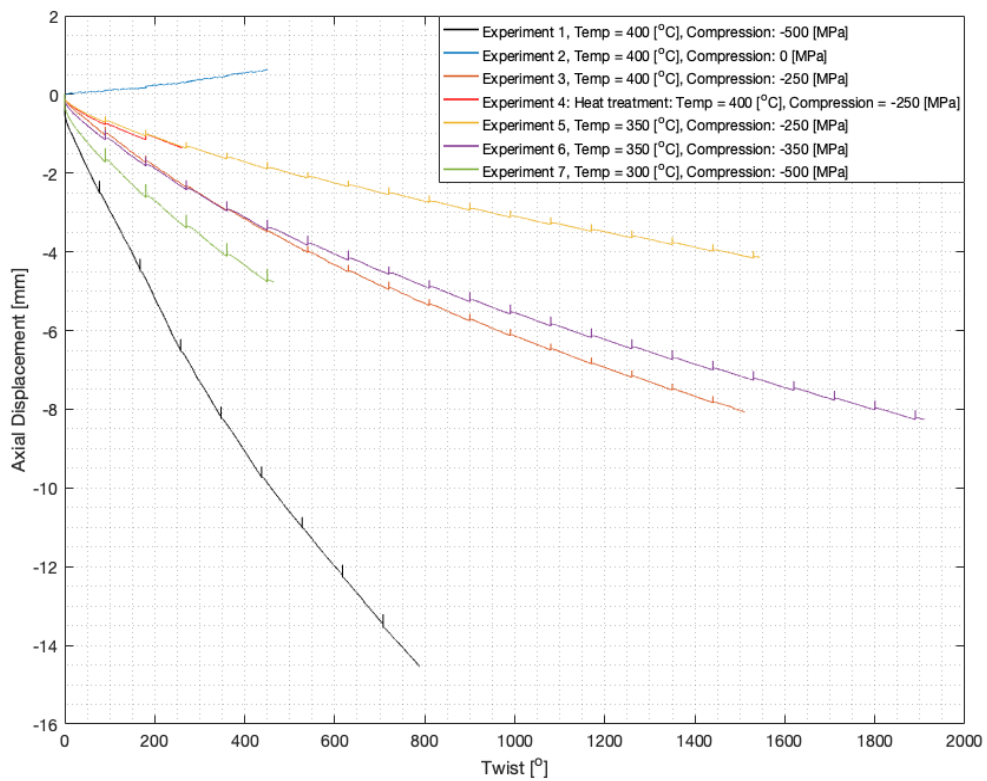
Figure 4.23: Change of specimens length

4.2 Material Characterization

Material characterization of the R260 rail material was conducted by calculating the accumulated shear strain for each test, hardness measurement for both deformed and undeformed rail material and finally by imaging the microstructure using both optical microscopy and scanning electron microscopy.

4.2.1 Shear Strain Measurements

Shear strain was calculated for test 1-7. The shear strain calculation by the grid method proved to show a generally higher amount of accumulated shear strain, see table 4.2. Shear strain could not be measured for test 4 because no flowlines were visible in the micrographs. Highest shear strain was measured for test 3 even though test 6 was twisted even more. The same behaviour can be seen between test 2 and 7.

Table 4.2: Strain measurements

Test	Grid (1), γ	Grid (2), γ	Software, γ	Accumulated twist [°]
1	3.0	3.2	3.4	805
2	2	2.0	2.4	360
3	10.0	10.4	8.3	1530
4	-	-	-	270
5	7.7	7.1	6.1	1530
6	7.8	7.8	5.3	1850
7	1.9	1.9	-	450

4.2.2 Hardness Measurements

This section begin with presenting an average reference hardness for the R260 rail steel which was compared with the average hardness for heat treated undeformed rail material at 350 °C and 400 °C. An average hardness for each flow line sample was also measured and the hardness gradient for each hardness sample was measured.

Reference and Heat Treated Samples

The mean value and standard deviation for the hardness measurements of the reference sample and the heat treated samples are listed in table 4.3. The mean value for the reference sample was 272 HV10 with a standard deviation of 6.6. Slightly higher mean values was obtained for the heat treated samples where the standard deviation was more than twice as large as the reference standard deviation.

Table 4.3: Hardness for reference and heat treatment samples

Test	Mean value - HV10	Standard deviation
Reference	272	6.6
350 °C	280	17
400 °C	283	15

Flowline Samples

The results from the hardness measurements of the flowline samples are listed in table 4.4 and the depths below the surface at which the hardness was measured are listed in Appendix A.2. A certain scatter in depth can be observed which is mainly due to the cutting from the sample preparation.

Highest hardness was measured in test 6 which achieved the most twisting cycles (22). Similarly the second highest hardness corresponds to test 5 which achieved the second most twisting cycles (18). This correlation between hardness and amount of twisting cycles cannot be seen for the rest of the measured hardness values. The third highest hardness corresponds to test 7 which achieved the second least number of twisting cycles.

Table 4.4: Hardness for flowlines samples

Test	Mean value - HV10	Standard deviation
1	367	5.4
2	381	6.5
3	431	49
4	348	18
5	487	3
6	521	12
7	447	3.5

Hardness Samples

The results from the hardness measurements in the axial direction along the radial direction for each test, are plotted in appendix A.4. The results were plotted as a mean value with error bars which represents the standard deviation. Hardness decreased towards the centre of the test bar as expected since torsional deformation is a function of radius with highest deformation at the surface.

The hardness gradient for all hardness samples are plotted together in figure 4.24. Hardness gradient was lowest for test 1, 2, and 4, intermediate for test 7, and 3, and highest for test 5 and 6. No correlation between hardness gradient and accumulated shear strain could be identified. However, hardness increased with accumulated twist and temperature for test 1-3 and test 5-6.
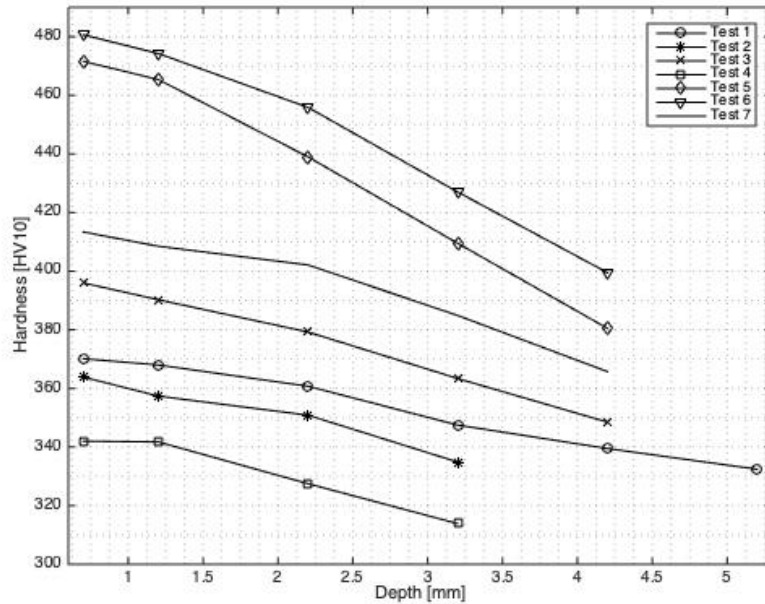
Figure 4.24: Hardness gradient for all hardness samples

4.2.3 Microstructure Analysis

The microstructure analysis show micrographs which are representative overviews of the microstructures for each flowline sample and field sample. The micrographs were taken at both low and high magnification using Optical Microscopy and scanning electron microscopy respectively. The optical micrographs were taken at the magnifications 50x and 100x, see appendix A.5. The SEM micrographs with high magnification were taken at 5k, 10k and 15k, see figure 4.25-4.35 and in appendix A.6. For the SEM micrographs the horizontal direction of the image corresponds to the radial direction of the test bar and the vertical direction corresponds to the axial direction of the test bar.

The microstructure analysis was conducted by comparing each test with the reference microstructure which was undeformed and non heat treated. It begins with presenting the reference and heat treated samples. It continues with presenting each of the tests conducted with the biaxial test rig. The microstructure analysis ends with presenting the microstructure of the field samples.

Room Temperature

Undeformed material of R260 rail steel was extracted from the grip section of a test bar and the microstructure was investigated in SEM, see figure 4.25. It was used as a reference image. The orientation of the colonies within each nodule appear to be more or less random. However some colonies (in the center part of the figure) show a structure where the lamellae have broken up. These structural faults are known as nucleation sites for spheriodization. The origin could be related to fabrication.
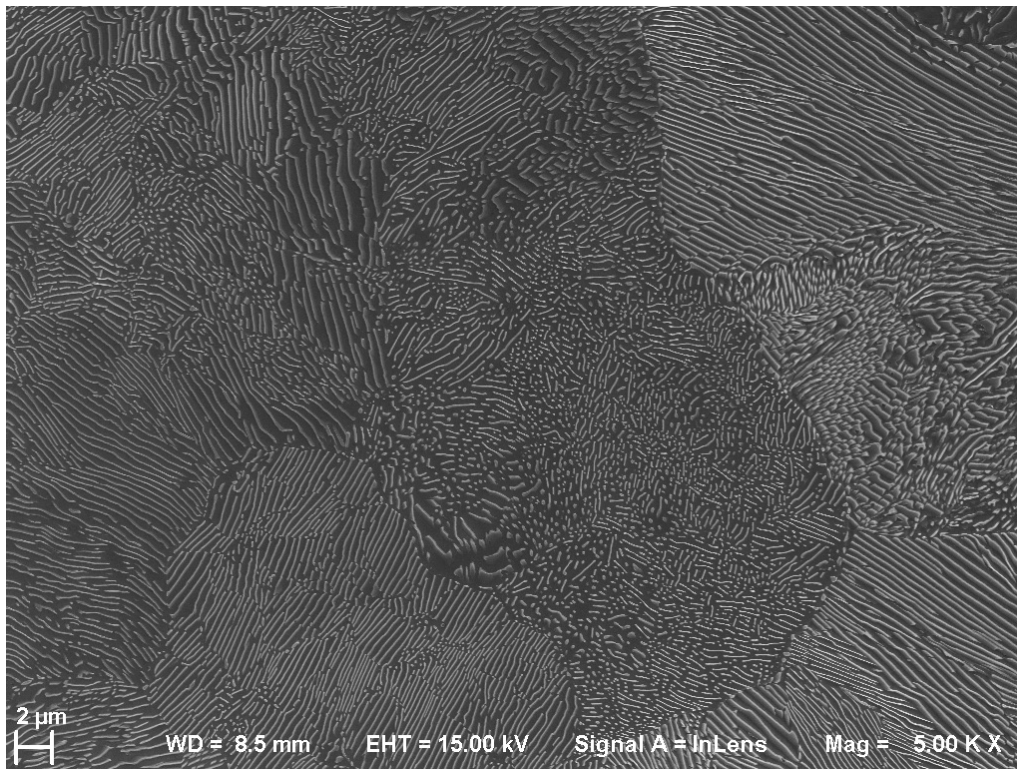
Figure 4.25: Microstructure of undeformed and non heat treated rail steel

350 °C

Undeformed material of R260 rail steel was heat treated at 350 °C and the microstructure is illustrated in figure 4.26. No substantial change in structure could be observed and no indication of spheriodization could either be found.
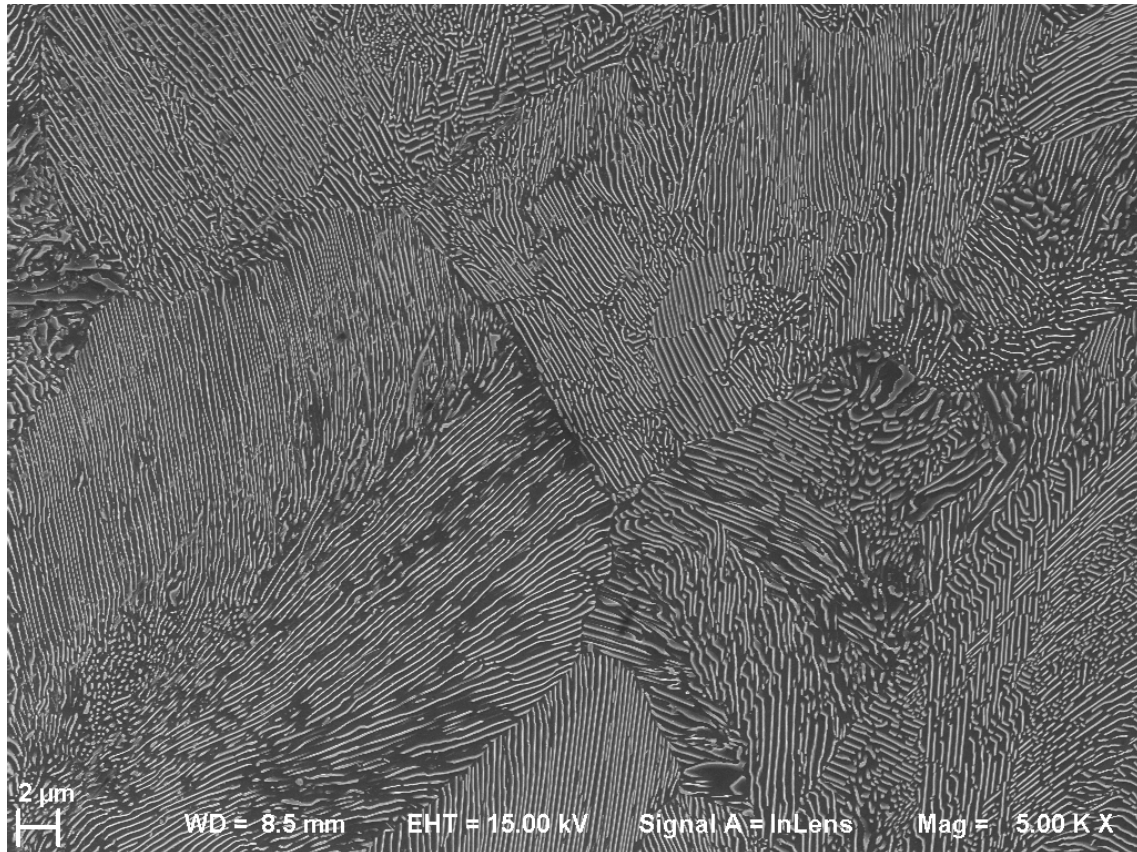
Figure 4.26: Microstructure after 350 °C heat treatment of undeformed rail steel.

400 °C

Undeformed material of R260 rail steel was heat treated at 400 °C and the microstructure is illustrated in figure 4.27. No substantial change in structure could be observed. No indication of spheriodization could either be found.
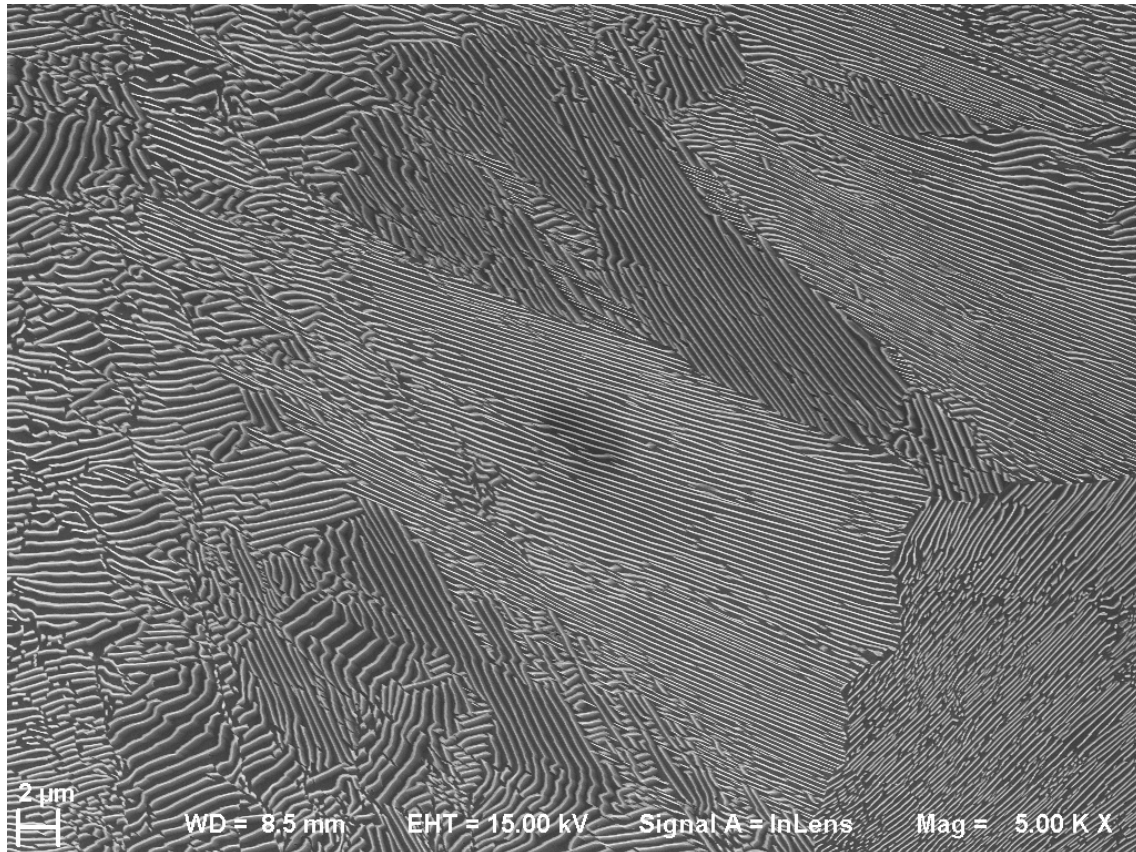
Figure 4.27: Microstructure after 400 °C heat treatment of undeformed rail steel.

Test 1

The representative microstructure for test 1 is shown in figure 4.28. The structure has become heavily deformed and is overall aligned. This overall alignment was also verified with the optical micrograph, see appendix A.5.1. Two observed extreme cases regarding lameallae orientation were found: in some regions the lamellae are parallel to the axial direction and in other regions the lamellae are almost parallel to the radial direction. The observed orientation of the most lamellae lies between these cases with an average angle calculated in section 4.2.1.

The lamellae were observed to be broken up in several regions. The broken structure was observed to mainly consist of small cementite fragments with the shape of an ellipse or plate. Additionally, in some areas the cementite had the shape of a sphere. Further, kinking of lamellae was also observed at several locations in the microstructure. Kinking was mainly observed where the lamellae were orientated in the axial direction.
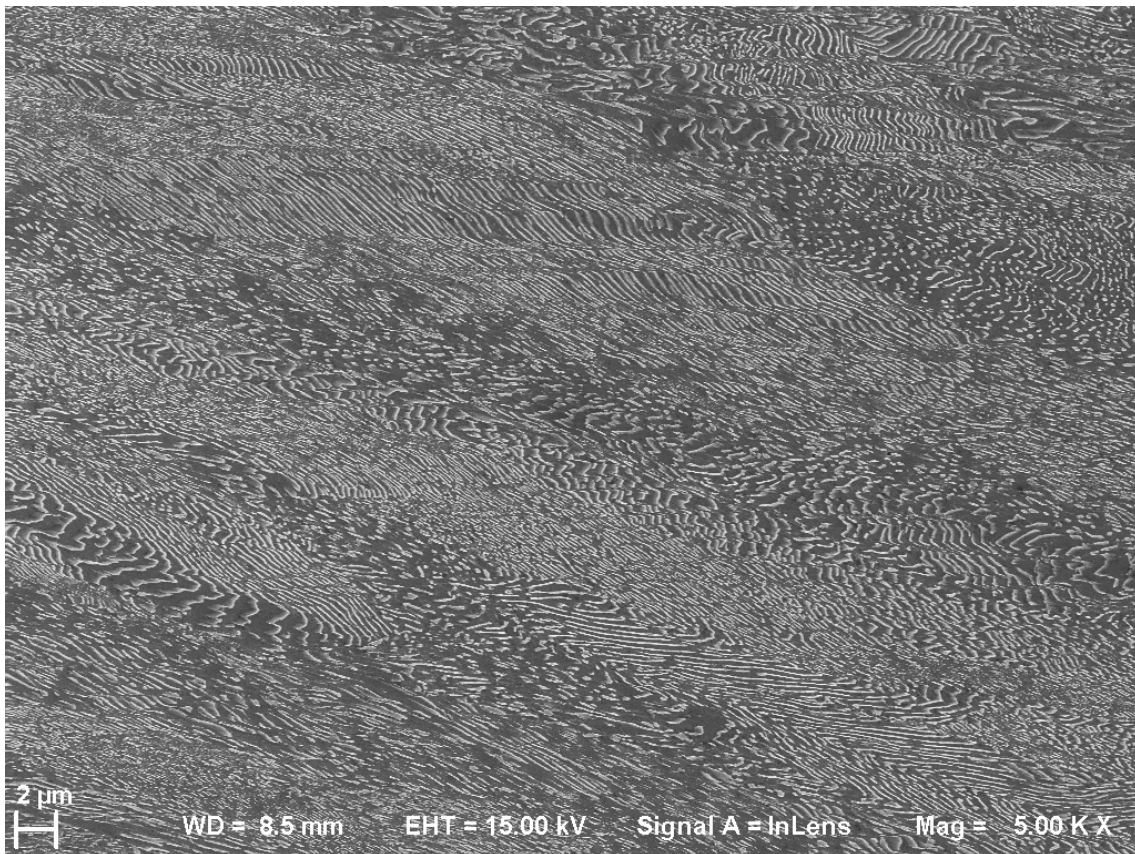
Figure 4.28: Microstructure of test 1.

Test 2

The representative microstructure for test 2 is shown in figure 4.29. The darker areas in the image are artifacts generated during the sample preparation and should be ignored. The overall microstructure was as in test 1 aligned which also was confirmed with the optical micrograph in appendix A.5.2. The two extreme cases regarding lamallea orientation as described for test 1 was also observed. The main observed difference compared to test 1 was that the microstructure was less aligned and the average angle between the lamellae and axial direction was lower i.e lower amount of accumulated shear strain.

The lamellae were further observed to be broken up in several regions. The cementite in the broken structure as in test 1 was observed to mainly consist of small cementite fragments with the shape of an ellipse or plate. Additionaly, in some regions the cementite had the shape of a sphere. Furthermore, kinking of lamellae was also observed at several locations in the microstructure. Kinking was mainly observed where the lamellae was oriented in the axial direction.
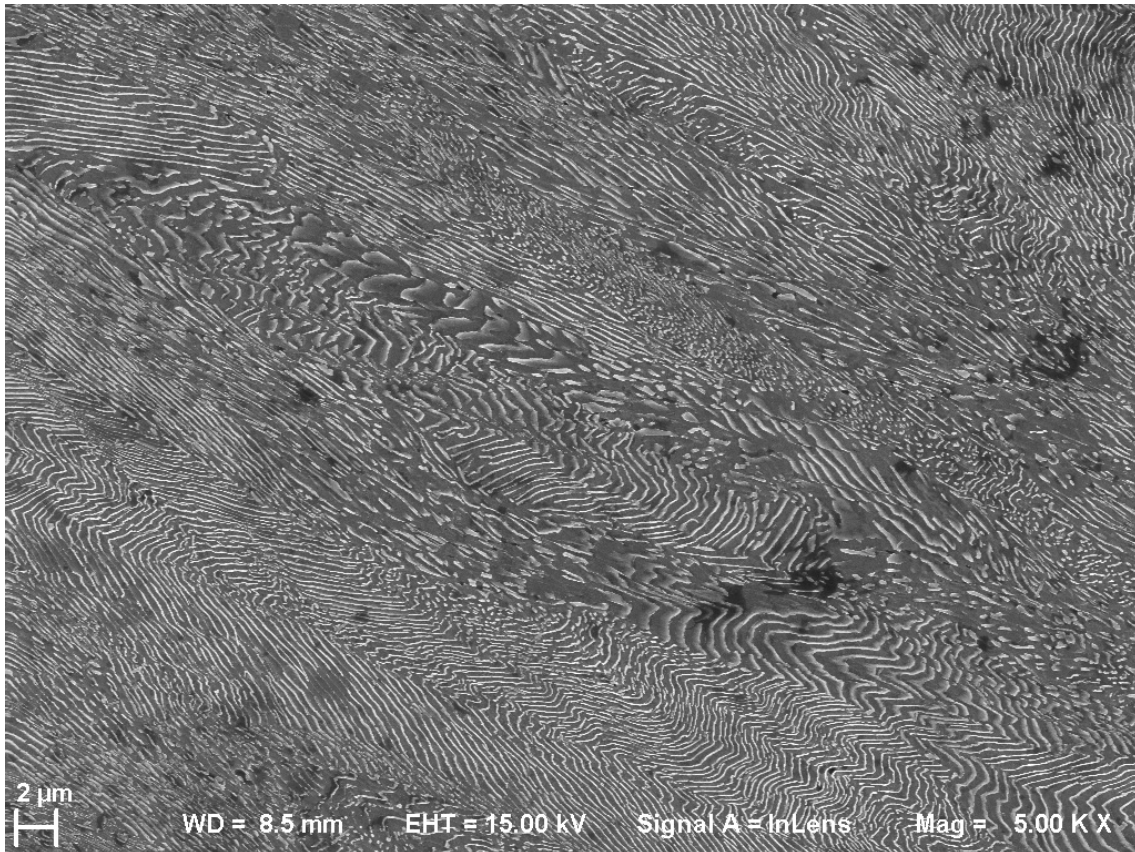
Figure 4.29: Microstructure of test 2

Test 3

The microstructure for test 3 is illustrated in figure 4.30. The optical micrographs are illustrated in A.5.3. The SEM micrographs were taken with 10k magnification. The average angle between the lamellae and axial direction was larger compared to test 1 and 2. Compared to test 1, no extreme cases regarding the lamellae orientation were observed. Instead it was observed that almost the entire structure was aligned in more or less the same direction. The aligned structure was either in the form of aligned lamellae or as in form of bands with broken up lamellae. This alignment can further be seen as flowlines in the optical micrograph, see appendix A.5.3. The most common observation was that the structure was aligned as bands with broken up lamellae. The broken up structure was further observed to mainly consist small cementite fragments with the shape of an ellipse or plate. Furthermore, in some regions the cementite had the shape of a sphere. In addition, kinking was observed observed to a lower extent compared with test 1 and 2.
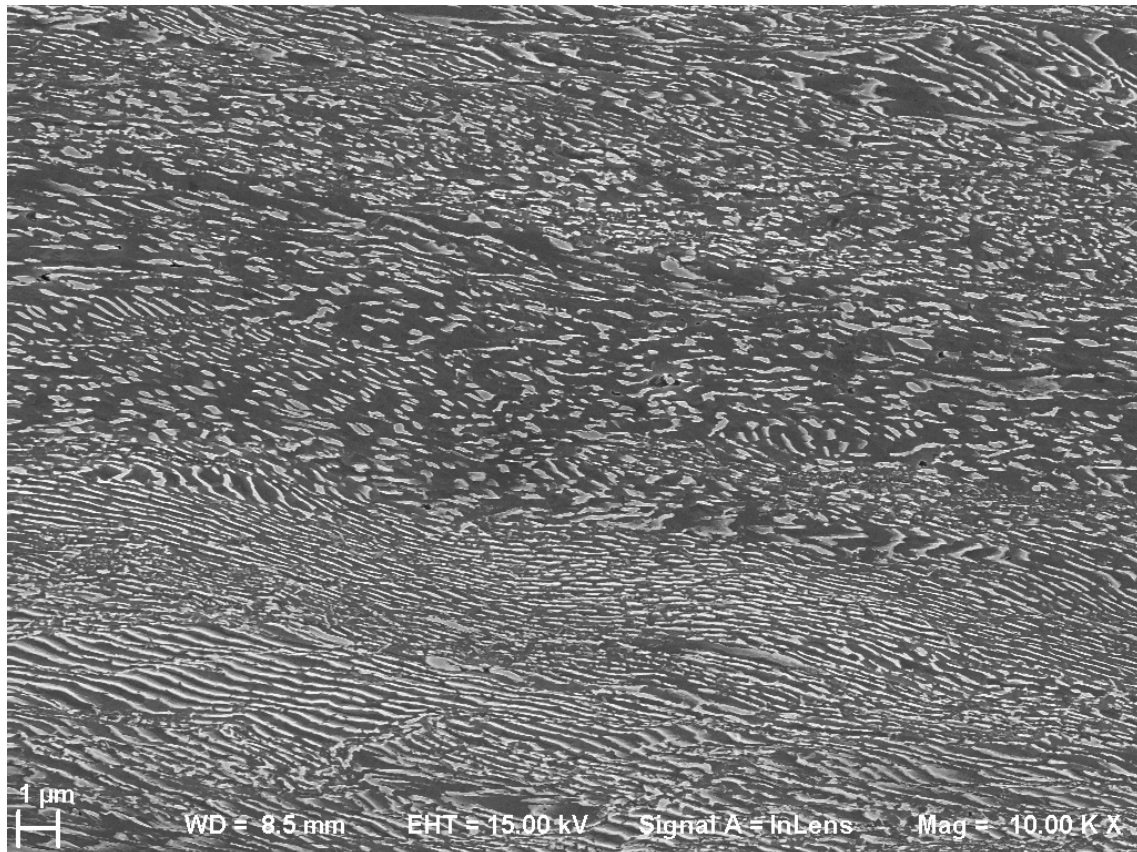
Figure 4.30: Microstructure of test 3

Test 4

The representative microstructure for test 4 is illustrated in figure 4.31. The colonies can be still be separated and no preferred orientation could be observed with the SEM. The optical micrographs, see appendix A.5.4, shows that there was a small texture development but no flow lines can be identified. Furthermore, the amount of broken up structure was observed to be low .
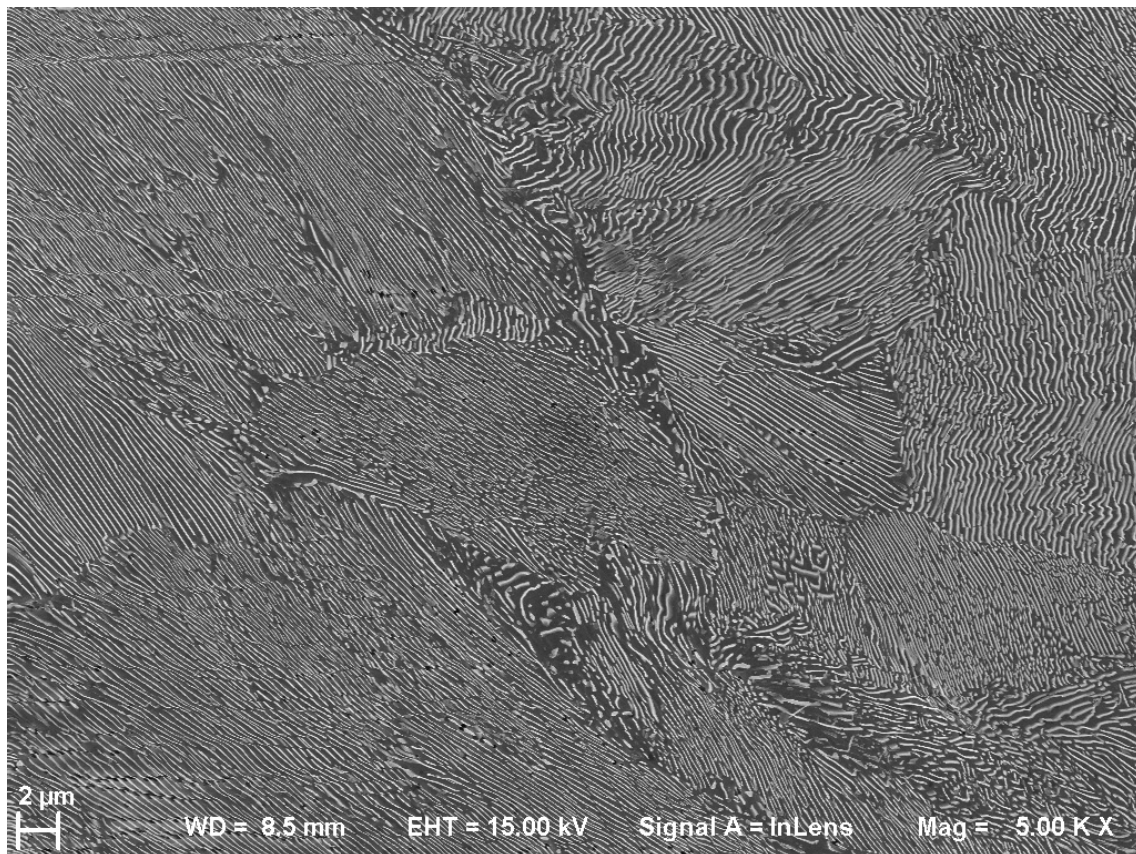
Figure 4.31: Microstructure of test 4

Test 5

The representative microstructure for test 5 is illustrated in 4.32. The structure has been heavily deformed and almost the entire structure as in test 3 was observed to be aligned in the same direction. This alignment can clearly be seen as flowlines in the optical micrograph, see appendix A.5.6. The structure was aligned in bands in which the structure was observed to be either aligned lamellae or broken up lamellae. The broken up lamellae were observed to mainly consist of small cementite fragments with the shape of an ellipse or plate. The amount of broken up lamellae within the bands were observed to be lower compared to test 3. Some lamellae within the bands had kinked and kinking was mainly observed for lamellae oriented close to the axial direction.
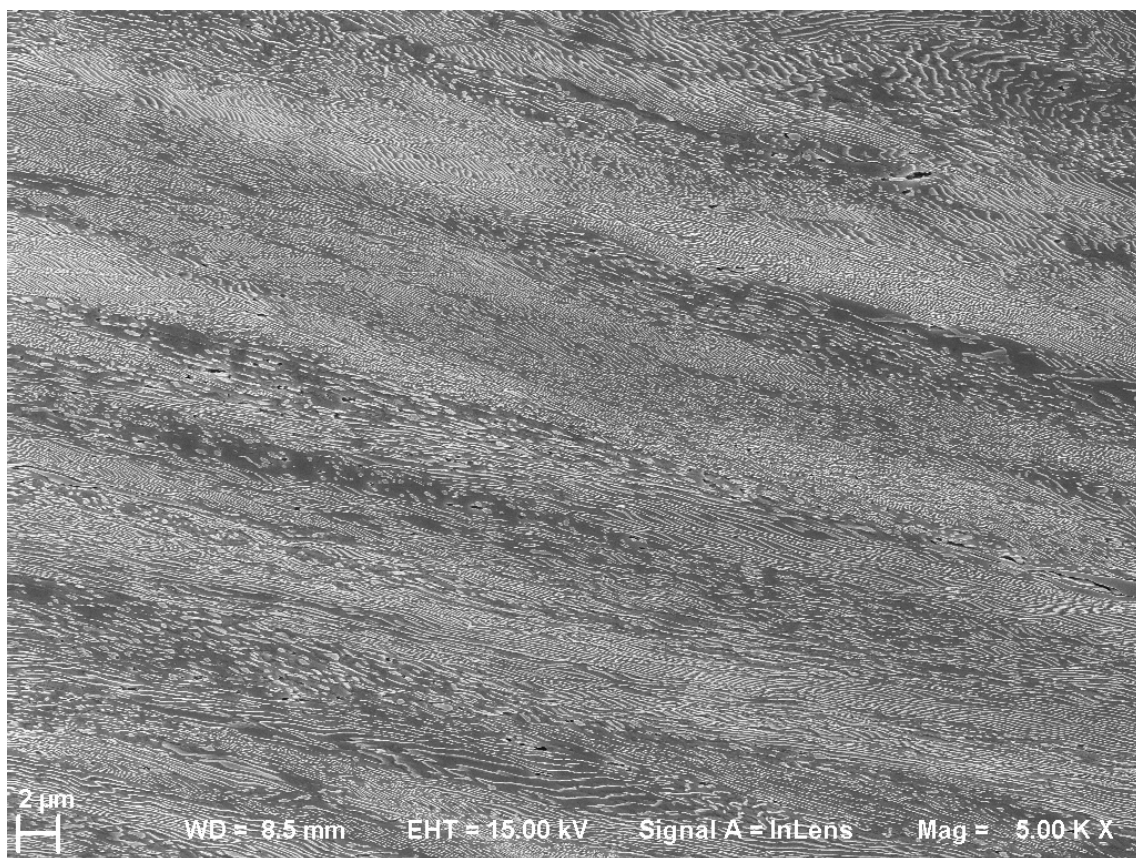
Figure 4.32: Microstructure of test 5

Test 6

The representative microstructure of test 6 is shown in figure 4.33. The overall structure is almost aligned in the same direction. The structure was observed to be similar to the structure in test 5. The observed difference was that the average angle between the alignment direction and axial direction was higher for test 6 i.e higher accumulated shear strain. Furthermore, compared to test 5 the structure is more wavy in test 6. The alignment was further clearly seen as flowlines in the optical micrograph, see appendix A.5.6.
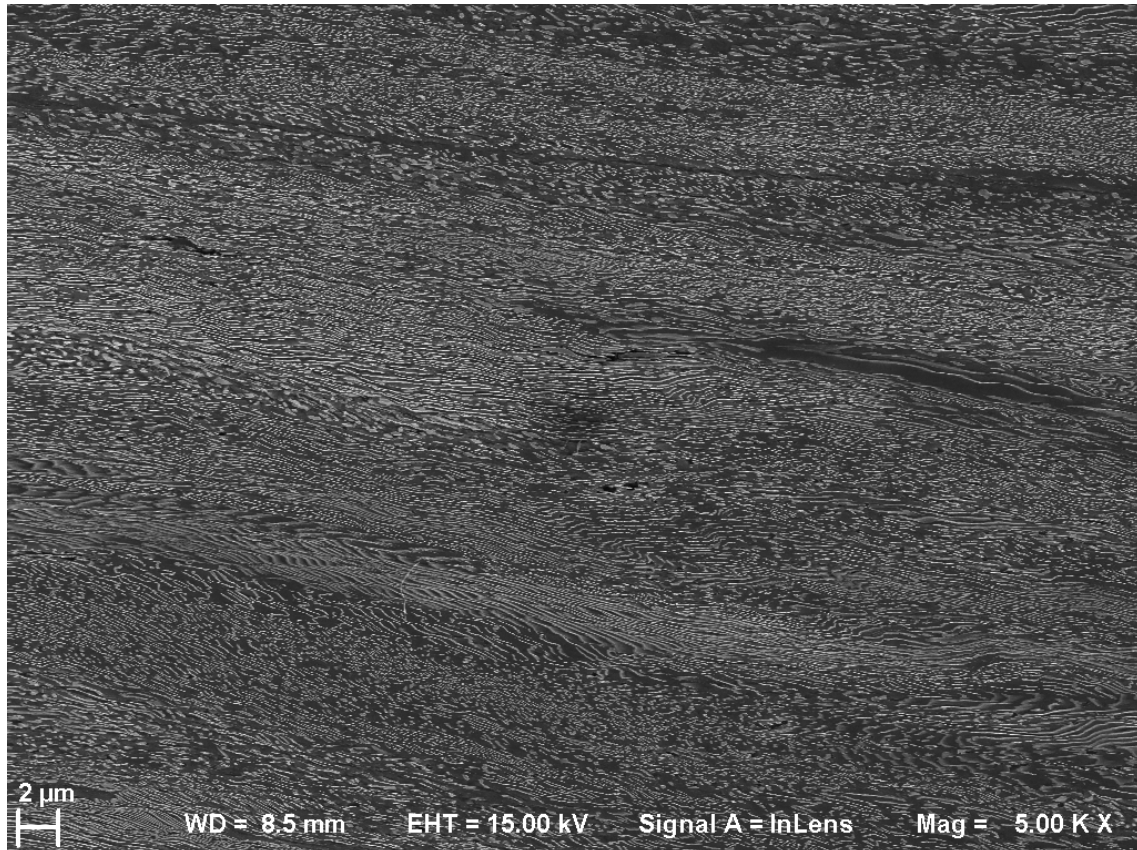
Figure 4.33: Microstructure of test 6

Test 7

The representative microstructure of test 7 is shown in figure 4.34. The colonies were identified in several regions and no preferred direction of the lamallae orientation could be observed. Instead, the colonies appear to be elongated which can be seen in the optical micrograph, see appendix A.5.7. The structure of test 7 was in SEM observed to be similar to test 4. The optical micrograph of test 7 was on the other hand more similar to test 2. There the main difference was that the angle between the orientation direction relative to the axial direction was larger for test 2.
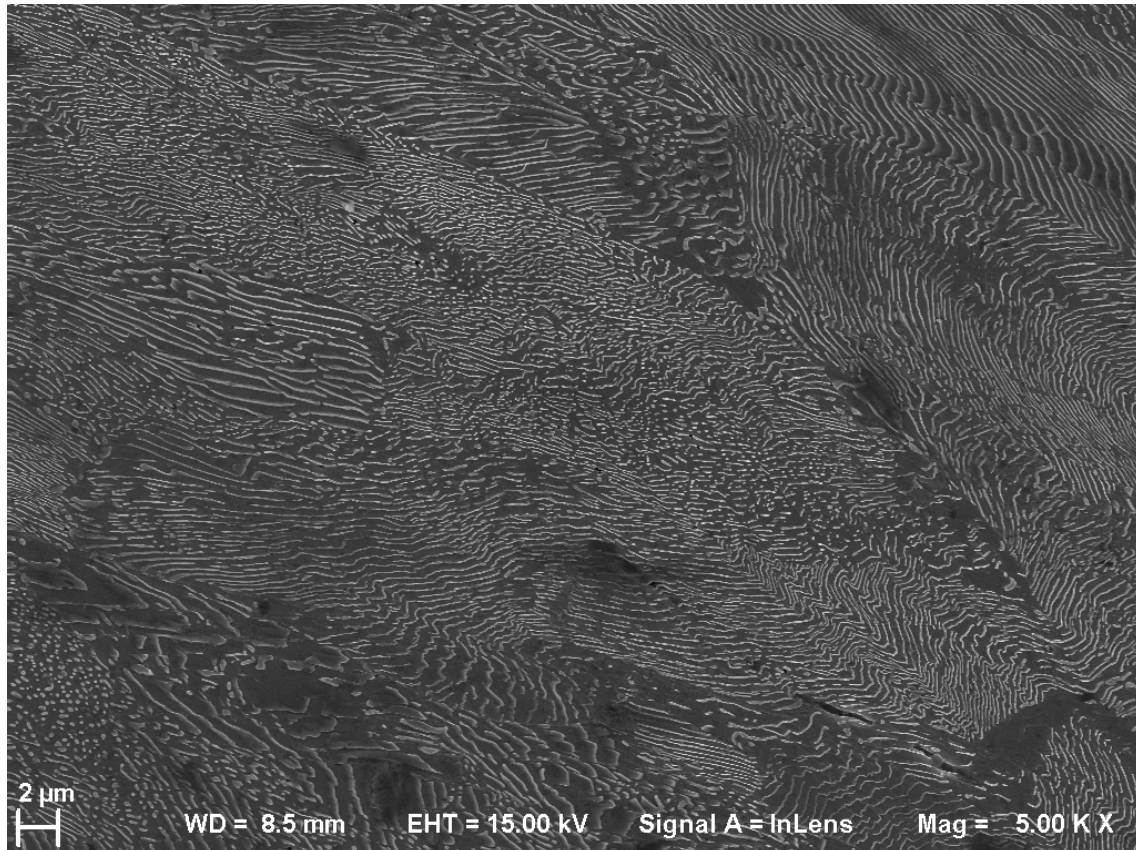
Figure 4.34: Microstructure of test 7

Field Sample

The field sample was provided from previous work [6] conducted at Chalmers and
has been extracted from the gauge corner of the rail at an angle of 45°. The representative microstructure of the field sample close to the surface is shown in figure 4.35.
Close to the surface the overall microstructure was observed to be aligned nearly
parallel to the surface of the gauge corner. The structure was further observed to
be aligned in wavy bands. Within the bands the lamallea were rather intact. The
microstructure of the field sample were resembled the structure in test 5 and 6. The
main difference was that the structure in test 5 and 6 was more broken up.

The field sample showed a microstructure which was aligned and the lamellae
had a low inclination angle. The microstructure appeared to be similar to the one
obtained for test 6.
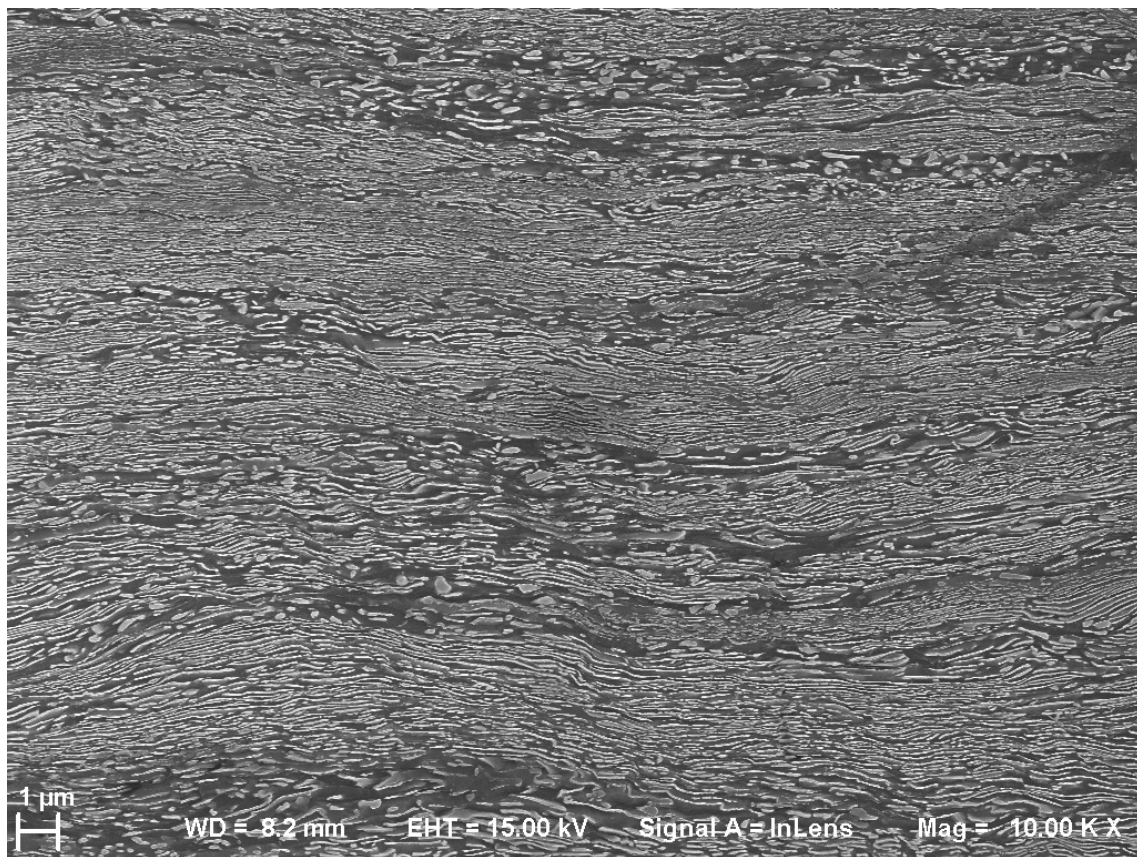
Figure 4.35: Microstructure of field sample

5

Discussion

In this chapter the results are discussed and connected to the theory. It begins with comparing the results from the tests conducted at elevated temperature with results from field samples and result from tests conducted at room temperature in terms of hardness and accumulated strain. It continues with describing the influence of the two parameters; temperature and compression load and how they governs the maximum amount of twisting that could be achieved. The temperature distribution over the test bar is further discussed. Furthermore, the effect of the increased diameter on the torque response is discussed. The accumulated strain is further discussed in terms of the strain measurements, hardness gradient, and the microstructure. The discussion ends with describing the reliability of the results and discuss how to further increase the number of twist cycles.

5.1 Comparison with Field Samples and Previous Work

The predeformation method developed by CHARMEC [6] as described in section 2.3, compared the properties and microstructure of biaxially deformed test bars with rail field samples. The highest hardness and amount of accumulated strain was achieved with a nominal axial compressive stress of -500 MPa. Maximum surface hardness was measured to 360 HV which decreased fairly uniformly towards the center of the test bar where the hardness was measured to 280 HV. The corresponding shear strain was approximately 2.3. Compared to the tests in this thesis both accumulated shear strain and hardness was measured to be higher for test 3, 5 and 6.

The maximum shear strain of the field material extracted from the gauge corner of the rail at 45° orientation was measured to 5.9 at the surface [6]. Compared to the tests in this thesis work, higher accumulated shear strain was obtained for tests 3, 5, and 6. Furthermore, the SEM investigations show that test 6 had a microstructure which was rather similar to the one observed in the field samples provided from previous work [6]. Both had a structure which had been mostly strained along one direction which can be seen by the aligned pearlite lamellae. Several micrographs had a wavy shaped structure which was also observed at different locations in the microstructure for test 6.

5.2   Effect of Temperature and Compression

The torque behavior was serrated for all tests conducted at elevated temperature. The magnitude of the serrations varied between each test and between the torque curves within each test. From the plots in appendix A3 it was observed that there seems to be a correlation between the temperature and torque response for test 1-3. It was observed that an increase in temperature lead to an decrease in torque and vice versa. However, it was not possible to predict how much the torque increased/decreased for a given temperature change. Based on the measured temperature the serrated torque response for test 1-3 is probably due to the temperature fluctuations. Regarding test 5-7 no such correlation could be found.

Highest amount of twisting was achieved for the tests conducted during constant heating at 350 °C and 400 °C. Constant heating at 300 °C showed a lower amount of twisting, see test 7. The low amount of twisting and high rate of work hardening for test 7 could be attributed to DSA. Furthermore, the difference between the two types of heat treatments (constant heating and heating in between twisting) is illustrated by comparing test 1 with test 4, see figure 4.22. By applying constant heating higher amount of twisting could be achieved, see test 1. Deformation was easier at elevated temperature but further investigations are required to determine the reason for this behavior. Test 4 with heating in between the twists had a higher work-hardening rate. A possible explanation could be that static strain ageing occurred after the material had been plastically deformed, unloaded and aged which lead to an increased yield strength and decreased ductility.

Increased compression load yielded in higher number of twisting cycles before failure at the temperatures 350 and 400 °C except for test 1 which buckled. The increased amount of deformation with increased compression load is most likely attributed to that compression suppress crack formation, see section 2.4.1. This explanation is further supported by the observations of crack formation during the tests, see section 4.1. It was observed that increased compression load postponed crack formation.

5.3   Temperature Distribution

The test bar was at the beginning of the tests heated in the section with diameter 10 and 11 mm, see figure 3.2 and 3.6. As deformation was proceeded the length of the test bar decreased and a larger section became heated. The diameter along the test bar after each test was quite uniform except test 1 which buckled, see appendix A7.1. This implies that the diameter gradually increased, starting from the gauge section. Furthermore this also implies that the temperature distribution in the radial direction along the test bar was quite uniform. If the temperature distribution would have been inhomogeneous along the test bar it should have resulted in an uneven diameter distribution.

The temperature distribution affect the overall deformation behavior since the mechanical behavior is temperature dependent. Based on the results a homogeneous temperature distribution would be desired since constant heating at elevated

temperature increase the deformation ability if DSA is not dominating over viscoplastic straining. An inhomogeneous temperature distribution would lead to a varying deformation ability of the material.

The temperature distribution was not managed to be measured. One effect that could have affected the temperature distribution was the skin effect. This effect as described in 2.16 generates a temperature gradient in the radial direction. Furthermore, the design of the induction coil, the position of the test bar inside the coil and distance between coil and sample are factors that could have influenced the temperature distribution. However, since the induction coil is designed to heat test bars with diameters between 6-12 mm the temperature distribution in radial direction should be quite uniform.

5.4 Effect of Diameter Increase on Torque Response

Axial compression was responsible for the length decrease and diameter increase of the test bars. As observed in 4.1.8, compression affected the rate at which torque was increased for the temperatures 350 -and 400 °C. Torque increased at a higher rate when the compression load was increased. The larger diameter increased the required torque to twist the bars. This contribution to the increased torque rate is important to take into account when the mechanical behaviour is evaluated since the torque response is both material and geometry dependent.

The torque increase of test 5 was low after the three first twisting cycles and the corresponding decrease in length was low. Furthermore the torque rate increase and length decrease for test 3 and 6 was similar. The hardness measured in axial direction along the radial direction was only slightly higher for test 6 compared to test 5. This implied that the material hardened at the beginning and that further torque increase was mainly attributed to the effect of diameter increase. A similar behavior was reported by Zhao et al [42]. However, the effect of compression in combination with elevated temperature on work hardening needs to be further investigated before any conclusions can be made.

5.5 Strain Measurement

The strain measurements showed different results depending on which method that was used. The depth of the flowlines was slightly different between the tests, which could have affected the results. The location at the test bar from which the samples had been extracted from could also have affected the measured strain, since it was unknown where maximum accumulated strain occurred. Furthermore, torsional deformation could have been concentrated in zones with different size where a smaller zone would result in higher accumulated shear strains. This could explain or partly explain why higher strains was measured for test 3 compared to test 5 and 6.

Overall, the strain measurement method seemed valid as a comparison value but it was unclear how accurate the shear strain values were. The method was dependent

on the visibility of the flowlines which can been seen for test 4 (see A.5.4) where it was impossible to measure the flowlines angles.

5.6 Hardness Gradient

The hardness gradient was used as an indication of how uniform deformation was. According to figure 4.24 the highest hardness gradient was obtained for test 5 and 6. This implied a more inhomogeneous deformation for test 5 and 6 along the radial direction. However, it seems that deformation was rather homogeneous in the near surface region (around 1.2 mm below the surface) for both tests. Looking at test 3, a more homogeneous deformation with a large amount of accumulated shear strain was obtained. It seemed that by conducting at a higher temperature (see test 3) a more uniform deformation could be obtained. The hardness gradient also provide some information about the strain and stress distribution in the sample. Highest amount of stress and strain was obtained at the surface region, since the maximum hardness was measured there. This can be expected since torque increase with the radius.

5.7 Microstructure

In several SEM micrographs (see figure 4.28, 4.30, 4.32 and 4.33) spherical shaped cementite were observed. The literature study provided mainly two explanations, either spheriodization or highly deformed cementite lamellae. According to previous work [47], lamellae in undeformed ferritic-pearlitic wheel material (grade R8T) starts to break up at 400 °C after 238 minutes annealing. Furthermore it was reported that monotonically prestrained wheel material started to spheroidize at 400 °C after 28 minutes annealing. The conclusion from the work was the material becomes more sensitive to spheroidization if the material have been cold worked. Connecting this to the thesis work no spheroidization was observed for the heat treated undeformed material, see figure 4.26 and 4.27.

Furthermore, the microstructure of test 3, 5 and, 6 was severely deformed and exposed to elevated temperature for a long time. Based on [47] it is possible that the broken structure and the spherical shaped cementite could partly be due to the spheroidization processes. However, it was not possible with SEM to determine whether the broken structure and spherical shaped cementite is attributed to spheroidization processes, heavy deformation or a combination of both. If spheroidization have been present then the amount of spheroidization will be the highest at the surface since deformation along the radial direction was inhomogeneous.

5.8 Reliability of the Results and Possible Error Sources

The strain distribution after the test was not directly visible with the naked eye. The highest amount of deformation should have been located somewhere in the middle. However, it was difficult when preparing the samples to judge where deformation have been largest and how large the heavily deformed zone was. Therefore, the measured hardness might not correspond to the hardness at the location with highest deformation. In order to get a more complete picture over stress and strain distribution, the whole test bar should had been sectioned into small samples where surface strain and hardness around each sample should be measured. Furthermore, on the same samples, hardness should also be measured along the radial direction on all the sectioned samples.

The measured hardness on the flowline samples should be seen as indicative rather than absolute because only two indents were made. Hardness measured along the radial direction is reliable since a large number of indents were made. The measured hardness should be quite representative for hardness of the heavily deformed zone but not necessarily representative for the most deformed zone.

The measured temperature is a possible error source. The stability of the temperature during the tests seemed to depend on the quality of the thermocouples. The measured temperature for test 1-3 is more stable than the measured temperature for test 5-7. As mentioned in section 3.2.7 three different looped thermocouples were used for tests: 1-3, 5 and 6-7. Furthermore, the measured temperature is not necessarily corresponding to the true temperature. Which factors that control the accuracy and precision of the temperature measurements has not been investigated in this work. This needs to be examined in order to determine the reliability of the temperature measurements.

A careful sample preparation method has been used for the microstructure characterization. However some minor effects could have affected the results e.g. reduced hardness from cutting or artifacts generated from the grinding/polishing.

Overall the results from the tests seems to be reasonable in terms of torque response, strain measurements, hardness measurements, and microstructure characterization. However only one test for each type of test has been conducted and therefore the reliability could be questioned. More tests need to be conducted to get more statistics and by this improve the reliability of the results.

5.9 How to Increase Number of Cycles?

The most optimal parameters in the specified parameter window when considering highest amount of accumulated strain were the ones used for test 6. During the twisting cracks appeared at the surface which caused the test bar to break. Perhaps if the test bars were grinded and polished after half the test cracks could be removed and it would allow further twisting which could result in a more homogeneous deformation in the test bar. However this requires further investigations.

5.10   New Test Bar Geometry

With the present test bar geometry, the maximum compression load is limited to -600 MPa at room temperature [50] and must be below -500 MPa at 400 °C in order to avoid buckling. Based on the results and literature [12] deformation increased with a higher compression load. An idea was to use higher compression loads to achieve larger deformation. This could be obtained if the test bar would be designed to sustain a larger compression load. However, there was no room to investigate this further in this project.

6
Conclusion and Future Work

An experimental characterization of fully pearlitic rail steels after thermomechanical straining was investigated. The most important conclusions for this work are listed below.

- The predeformation methodology with constant temperature is able to produce a material with a microstructure which was rather similar to the one found in the surface layer of rail field materials. The microstructure was observed to have pearlite lamellae which were closely spaced, aligned and oriented with a low inclination angle along the sheared direction. Additionally, some pearlite lamellae was observed to have a wavy shape.

- Higher shear strains and strength was measured for the tests conducted at elevated temperature compared to previous work which was conducted at room temperature. However, the test bars contain several cracks and further work is required to be able to use them for mechanical testing.

- Temperature and compression have large influence on the amount of twisting that can be achieved. Deformation increased with compression load if buckling was avoided. The effect of increasing compression load was to increase the resistance to crack formation and crack propagation. The ductility of the material was increased when deformation was conducted at 350 and 400 °C and allowed more twisting. During deformation at 350 °C dynamic strain ageing occurred and when deformation was conducted at room temperature with heating in between the twisting cycles static strain ageing occurred. These hardening mechanisms decreased the ductility of the material and increased the work hardening rate.

- The microstructure and hardness were dependent on the process parameters. Hardness increased with deformation and was dependent on the temperature. Higher hardness was obtained at 350 °C compared to 400 °C. Furthermore, the microstructure became more aligned and broken up with deformation.

- To avoid severe spheriodization and to obtain maximum amount of accumulated shear in the test bars, a temperature close to 350 °C should be selected for the predformation methodology with constant temperature.

- The shear strain measurement methods gave a large spread in the measured values and were dependent on the visibility of the flowlines. These methods

were only able to give a rough estimation but could be used for comparison.

- All tests need to be repeated in order to increase the reliability of the results and see if the methodology with constant temperature can give reproducible results.

The amount of accumulated shear strain that can be reached during simultaneous axial compression-torsion is a function of twist rate, temperature, temperature distribution and nominal axial compression stress. Further research of how these parameters are correlated and how they affect the mechanical behavior is suggested. With this knowledge it might be possible to achieve a more uniform microstructure and higher shear strains. Additionally, a predeformation method that can tailor the microstructure and properties after the desired rail field sample might be possible with further research.

Measuring the heat distribution along the test bar is also recommended as future work since it would verify that the technique is able to provide a homogeneous heat distribution. An attempt has been made to measure the heat distribution with a thermal camera, however the view of the test bar was blocked by the induction coil and therefore it could not be measured. Future work would then have to modify the setup or use another way to measure the heat distribution.

As previously mentioned a new test bar geometry which can withstand higher compression loads for the thermomechanical testing is recommended as future work to see if it is possible to achieve higher strains and strength of the rail material.

Bibliography

[1] Dimitrios Nikas. *Influence of combined thermal and mechanical loadings on pearlitic steel microstructure in railway wheels and rails.* Doktorsavhandlingar vid Chalmers tekniska högskola. Ny serie: 4482. Chalmers University of Technology, 2018.

[2] Martin Schilke. *Degradation of railway rails from a materials point of view.* Doktorsavhandlingar vid Chalmers tekniska högskola. Ny serie: 3498. Chalmers University of Technology, 2013.

[3] Knut Andreas Meyer, Magnus Ekh, and Johan Ahlström. Modeling of kinematic hardening at large biaxial deformations in pearlitic rail steel. *International Journal of Solids and Structures*, 130-131:122 – 132, 2018.

[4] Olofsson U. Lewis, R. *Wheel-Rail Interface Handbook.* Woodhead Publishing, 2009.

[5] S. Beretta, S. Foletti, and K. Valiullin. Fatigue crack propagation and threshold for shallow micro-cracks under out-of-phase multiaxial loading in a gear steel. *Engineering Fracture Mechanics*, 77(11):1835 – 1848, 2010. International Conference on Crack Paths 2009.

[6] Knut Andreas Meyer, Dimitrios Nikas, and Johan Ahlström. Microstructure and mechanical properties of the running band in a pearlitic rail steel: Comparison between biaxially deformed steel and field samples. *Wear*, 396-397:12 – 21, 2018.

[7] Honeycombe Robert Bhadeshia, Harshad. *Steels - Microstructure and Properties (4th Edition).* Elsevier, 2017.

[8] Nasim Larijani, Christoph Kammerhofer, and Magnus Ekh. Simulation of high pressure torsion tests of pearlitic steel. *Journal of Materials Processing Technology*, 223:337 – 343, 2015.

[9] F. Wetscher, R. Pippan, S. Sturm, F. Kauffmann, C. Scheu, and G. Dehm. Tem investigations of the structural evolution in a pearlitic steel deformed by high-pressure torsion. *Metallurgical and Materials Transactions A*, 37(6):1963–1968, Jun 2006.

[10] Yu. Ivanisenko, W. Lojkowski, R.Z. Valiev, and H.-J. Fecht. The mechanism of formation of nanostructure and dissolution of cementite in a pearlitic steel during high pressure torsion. *Acta Materialia*, 51(18):5555 – 5570, 2003.

[11] T. Leitner, G. Trummer, R. Pippan, and A. Hohenwarter. Influence of severe plastic deformation and specimen orientation on the fatigue crack propagation behavior of a pearlitic steel. *Materials Science and Engineering: A*, 710:260 – 270, 2018.

[12] Andrzej Rosochowski. *Severe Plastic Deformation Technology*. Whittles Publishing, 2017.

[13] Xiaodan Zhang, Andy Godfrey, Xiaoxu Huang, Niels Hansen, and Qing Liu. Microstructure and strengthening mechanisms in cold-drawn pearlitic steel wire. *Acta Materialia*, 59(9):3422 – 3430, 2011.

[14] Muñoz Jairo Ostwald, Phillip F. *Manufacturing Processes and Systems (9th Edition)*. John Wiley and Sons, 1997.

[15] J. Toribio. Relationship between microstructure and strength in eutectoid steels. *Materials Science and Engineering: A*, 387-389:227 – 230, 2004. 13th International Conference on the Strength of Materials.

[16] J. Toribio and E. Ovejero. Effect of cumulative cold drawing on the pearlite interlamellar spacing in eutectoid steel. *Scripta Materialia*, 39(3):323 – 328, 1998.

[17] Tian-Zhang Zhao, Shi-Hong Zhang, Guang-Liang Zhang, Hong-Wu Song, and Ming Cheng. Hardening and softening mechanisms of pearlitic steel wire under torsion. *Materials and Design*, 59:397 – 405, 2014.

[18] Y. Tomota, O. Watanabe, A. Kanie, A. Moriai, N. Minakawa, and Y. Moriai. Effect of carbon concentration on tensile behaviour of pearlitic steels. *Materials Science and Technology*, 19(12):1715–1720, 2003.

[19] David A. Porter, Kenneth. E. Easterling, and Mohamed Y. Sherif. *Phase transformations in metals and alloys*. CRC, 2009.

[20] George Krauss. *Steels - Processing, Structure, and Performance (2nd Edition)*. ASM International, 2015.

[21] Ngan A. H. W. Smallman, R. E. *Physical Metallurgy and Advanced Materials (7th Edition)*. Elsevier, 2007.

[22] Leonard E. Samuels. *Light Microscopy of Carbon Steels*. ASM International, 1999.

[23] Yong Tian and R. Kraft. Mechanisms of pearlite spheroidization. *Metallurgical transactions. Part A: Physical Metallurgy and Materials Science*, 18(8):1403, 1987.

[24] S. Chattopadhyay and C.M. Sellars. Kinetics of pearlite spheroidisation during static annealing and during hot deformation. *Acta Metallurgica*, 30(1):157 – 170, 1982.

[25] Joshua Pelleg. *Mechanical Properties of Materials. [electronic resource].* Solid Mechanics and Its Applications: 190. Springer Netherlands, 2013.

[26] William F. Hosford. *Mechanical Behavior of Materials.* Cambridge University Press, 2 edition, 2009.

[27] S. L. Semiatin. *ASM Handbook, Volume 14A - Metalworking: Bulk Forming.* ASM International, 2005; 2009.

[28] Taira Suzuki, Shin Takeuchi, and Hideo Yoshinaga. *Dislocation Dynamics and Plasticity. [electronic resource].* Springer Series in Materials Science: 12. Springer Berlin Heidelberg, 1991.

[29] Clark Alan F. Reed, Richard P. *Materials at Low Temperatures.* ASM International, 1983.

[30] B.A. K and C.P. Sharma. *Mechanical Behaviour and Testing of Materials.* Prentice Hall India Pvt., Limited, 2011.

[31] Marc A. Meyers and Krishan Kumar Chawla. *Mechanical behavior of materials.* Cambridge University Press, 2009.

[32] M. Hiratani and E.M. Nadgorny. Combined model of dislocation motion with thermally activated and drag-dependent stages. *Acta Materialia*, 49(20):4337 – 4346, 2001.

[33] F.C. Campbell. *Elements of Metallurgy and Engineering Alloys.* ASM International, 2008.

[34] L. E. Murr. Dislocation ledge sources: Dispelling the myth of frank–read source importance. *Metallurgical and Materials Transactions A*, 47(12):5811–5826, Dec 2016.

[35] M. Dollar, I.M. Bernstein, and A.W. Thompson. Influence of deformation substructure on flow and fracture of fully pearlitic steel. *Acta Metallurgica*, 36(2):311 – 320, 1988.

[36] O.P Modi, N Deshmukh, D.P Mondal, A.K Jha, A.H Yegneswaran, and H.K Khaira. Effect of interlamellar spacing on the mechanical properties of 0.65 % c steel. *Materials Characterization*, 46(5):347 – 352, 2001.

[37] Xiaodan Zhang, Andy Godfrey, Xiaoxu Huang, Niels Hansen, and Qing Liu. Microstructure and strengthening mechanisms in cold-drawn pearlitic steel wire. *Acta Materialia*, 59(9):3422 – 3430, 2011.

[38] Y. Tomota, O. Watanabe, A. Kanie, A. Moriai, N. Minakawa, and Y. Moriai. Effect of carbon concentration on tensile behaviour of pearlitic steels. *Materials Science and Technology*, 19(12):1715–1720, 2003.

[39] Nitin Chandola, Ricardo A. Lebensohn, Oana Cazacu, Benoit Revil-Baudard, Raja K. Mishra, and Frédéric Barlat. Combined effects of anisotropy and tension–compression asymmetry on the torsional response of az31 mg. *International Journal of Solids and Structures*, 58:190 – 200, 2015.

[40] R. Nakkalil, J.R. Hornaday, and M. Nabil Bassim. Characterization of the compression properties of rail steels at high temperatures and strain rates. *Materials Science and Engineering: A*, 141(2):247 – 260, 1991.

[41] C.H. Gur and J. Pan. *Handbook of Thermal Process Modeling Steels*. CRC Press, 2008.

[42] Tian-Zhang Zhao, Shi-Hong Zhang, Guang-Liang Zhang, Hong-Wu Song, and Ming Cheng. Hardening and softening mechanisms of pearlitic steel wire under torsion. *Materials and Design*, 59:397 – 405, 2014.

[43] Loveless Don Cook Raymond L. Rudnev, Valery. *Handbook of Induction Heating (2nd Edition)*. CRC Press, 2017.

[44] Carsten J. Peters and Dietmar Eifler. Influence of service temperatures on the fatigue behaviour of railway wheel and tyre steels*. *Materials Testing*, 51:748–754, 11 2009.

[45] V. Wagner, P. Starke, E. Kerscher, and D. Eifler. Cyclic deformation behaviour of railway wheel steels in the very high cycle fatigue (vhcf) regime. *International Journal of Fatigue*, 33(1):69 – 74, 2011. Advances in Very High Cycle Fatigue.

[46] *Railway applications – Track – Rail – Part 1: Vignole railway rails 46 kg / m and above, Svensk standard ss-en 13674-1:2011+a1:2017*. Tech.rep, 2017.

[47] Dimitrios Nikas, Johan Ahlström, and Amir Malakizadi. Mechanical properties and fatigue behaviour of railway wheel steels as influenced by mechanical and thermal loadings. *Wear*, 366-367:407 – 415, 2016. Contact Mechanics and Wear of Rail / Wheel Systems, CM2015, August 2015.

[48] Birgit Ottesen Michael Ruckert Leila Bjerregaard, Kay Geels. *Metalog guide, Your Guide to the Perfect Materialographic Structure*. Struers A/S, 2002.

[49] F.A.M. Alwahdi, A. Kapoor, and F.J. Franklin. Subsurface microstructural analysis and mechanical properties of pearlitic rail steels in service. *Wear*, 302(1):1453 – 1460, 2013. Wear of Materials 2013.

[50] Knut Andreas Meyer, Magnus Ekh, and Johan Ahlström. Modeling of kinematic hardening at large biaxial deformations in pearlitic rail steel. *International Journal of Solids and Structures*, 130-131:122 – 132, 2018.

A
Appendix 1

A.1 Diameter Change After Thermomechanical Testing

The diameter change after the thermomechanical testing is illustrated in table A.1. The diameter was measured at 13 mm offset from the grip section and in the middle of the test bar as illustrated in figure A.1.
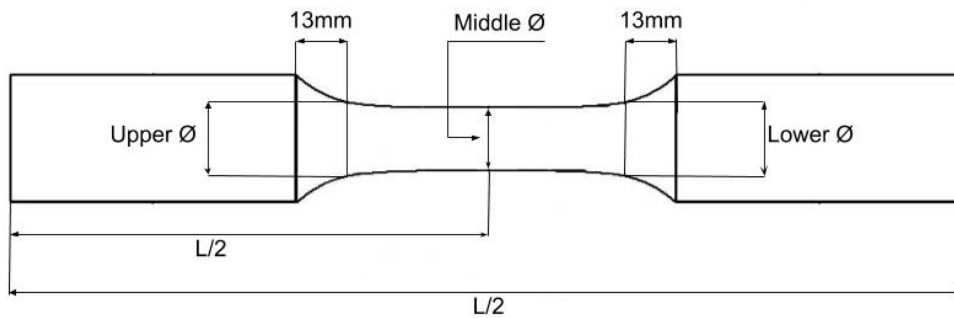
Figure A.1: Diameter measurement

Table A.1: Diameter change after and before deformation

Test	Undeformed bar	1	2	3	4	5	6	7
∅ Upper [mm]	10.5	12.71	10.40	12.05	10.45	10.75	11.42	10.76
∅ Middle [mm]	10	13.60	10.00	12.11	10.29	11.25	11.85	10.97
∅ Lower [mm]	10.5	12.58	10.45	10.85	10.85	10.64	11.87	10.75

A.2   Depth of Flowlines

The measured parameters and the maximum depth of each sample from the radial direction is shown in table A.2 below.

Table A.2: Depth of flowlines

Test	r [mm]	b [mm]	ϕ [°]	h [mm]	d [mm]
1	6.8	2.027	17.34	6.49	0.309
2	5	1.649	19.25	4.72	0.279
3	6.055	1.903	18.31	5.748	0.306
4	5.145	2.11	24.22	4.69	0.453
5	5.625	1.76	18.24	5.34	0.282
6	5.925	1.78	17.48	5.65	0.273
7	5.485	1.677	17.79	5.22	0.262

A.3 Thermomechanical Testing

Additional results from the thermomechanical testing is presented. The plots show
how torque and temperature change with time during each test.

A.3.1 Test 1
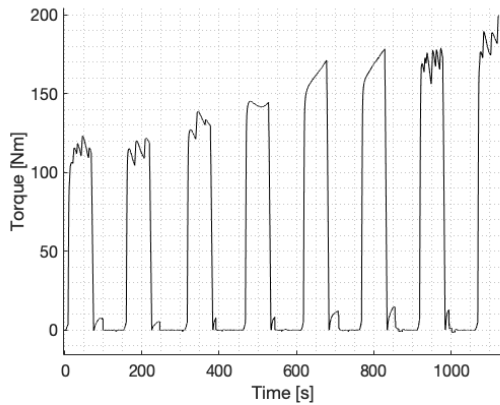
Figure A.2: Torque vs time
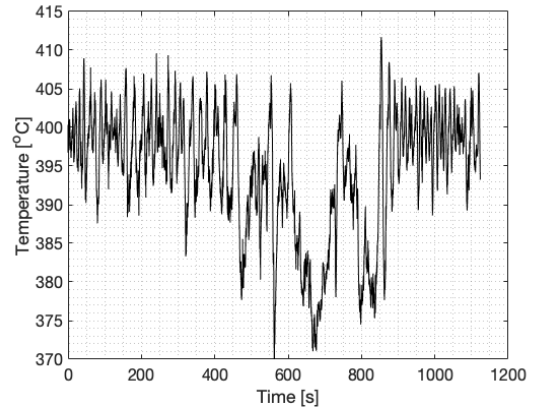
Figure A.3: Temperature vs time
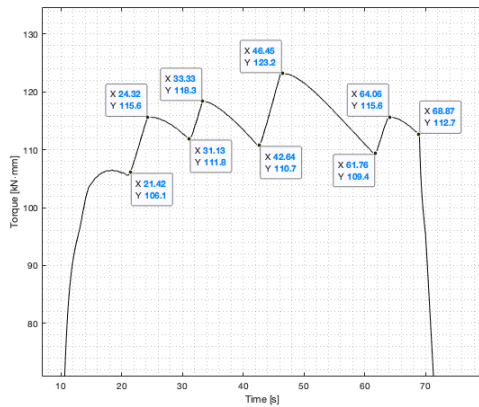
Figure A.4: Max and min values
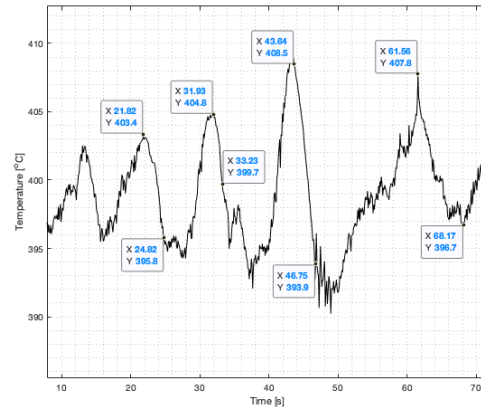
Figure A.5: Max and min values

A.3.2 Test 2
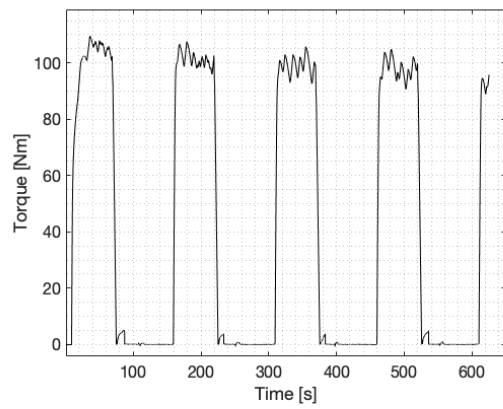
Figure A.6: Torque vs time
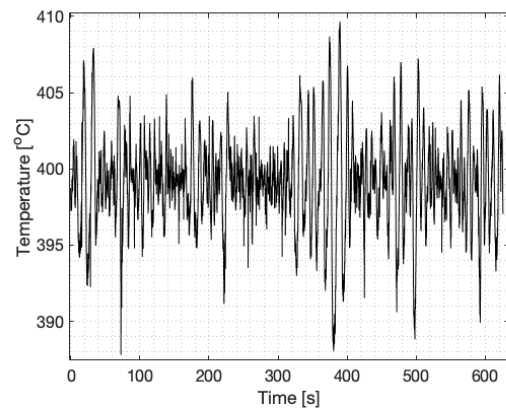
Figure A.7: Temperature vs time
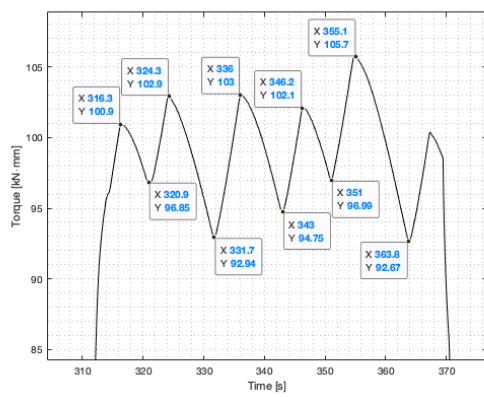
Figure A.8: Max and min values
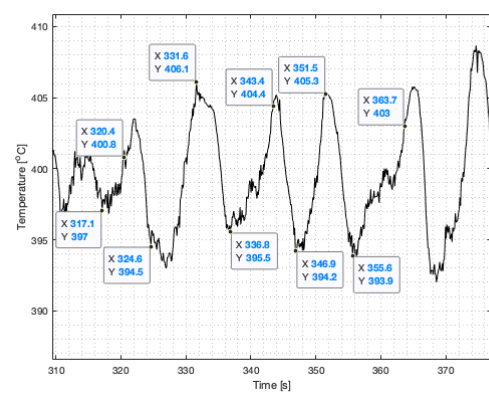
Figure A.9: Max and min values

A.3.3 Test 3
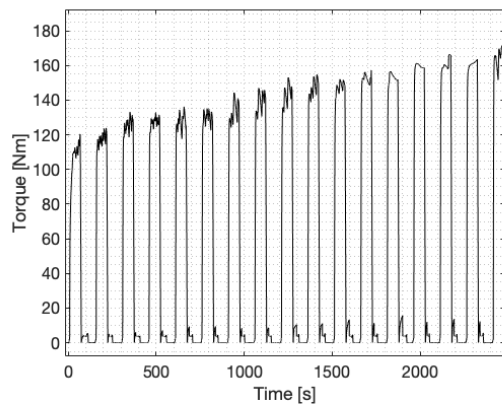
Figure A.10: Torque vs time
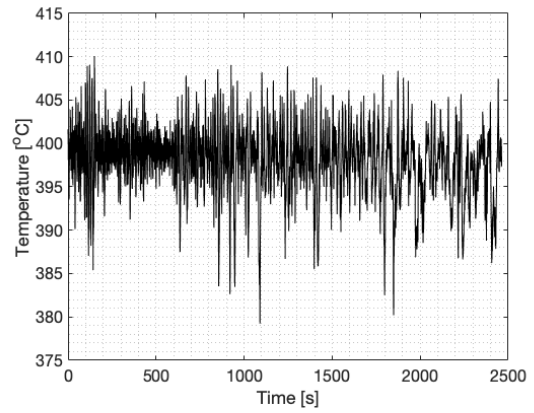
Figure A.11: Temperature vs time
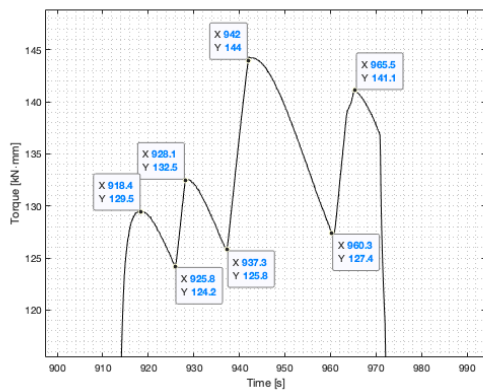
Figure A.12: Max and min values
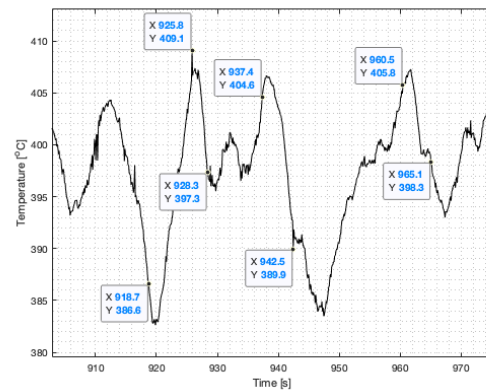
Figure A.13: Max and min values

A.3.4 Test 4
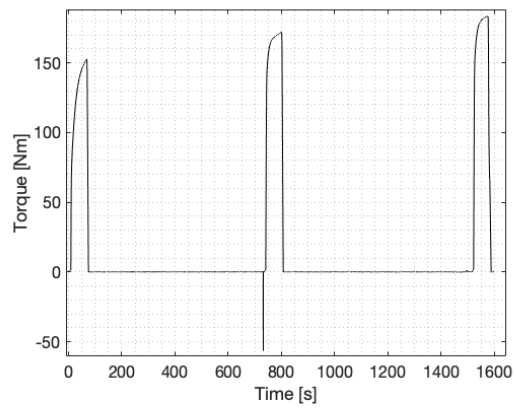
Figure A.14: Torque vs time
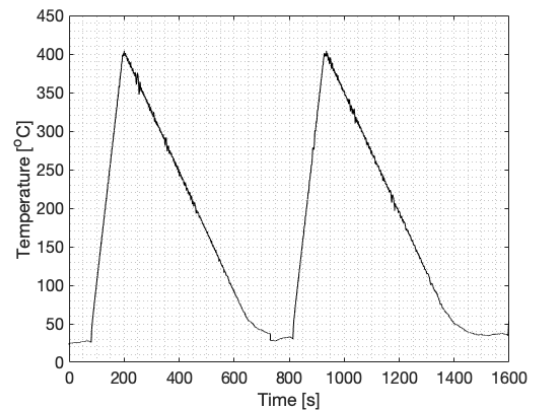
Figure A.15: Temperature vs time

A.3.5 Test 5
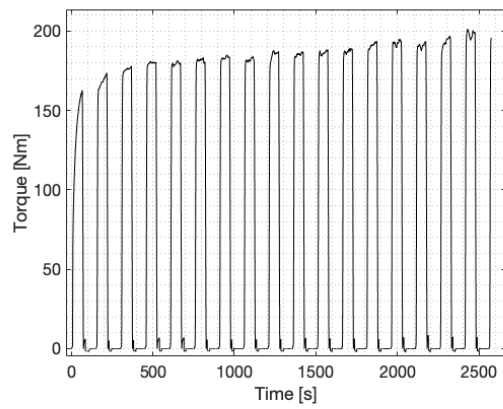
Figure A.16: Torque vs time
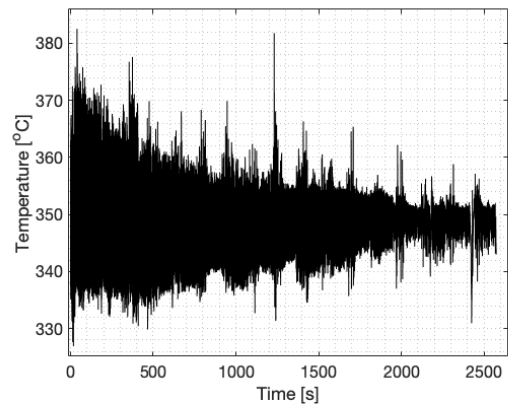
Figure A.17: Temperature vs time
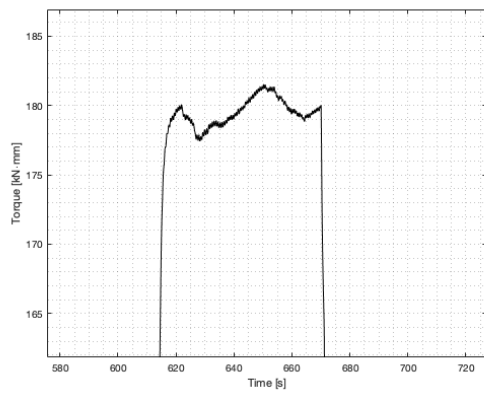
Figure A.18: Max and min values
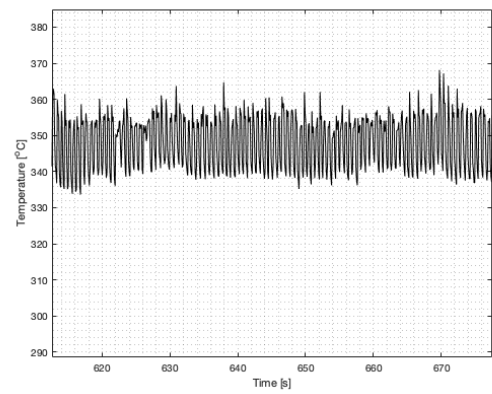
Figure A.19: Max and min values

A.3.6 Test 6
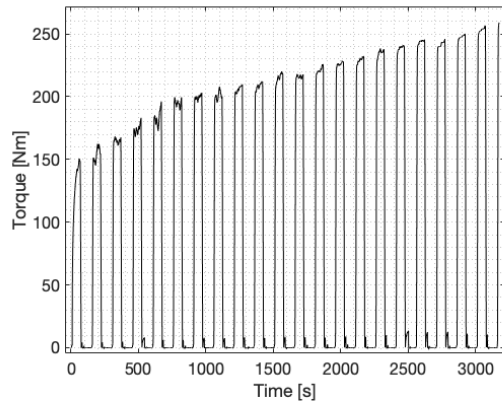
Figure A.20: Torque vs time
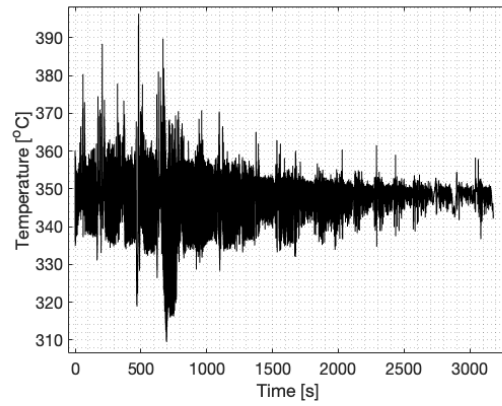
Figure A.21: Temperature vs time
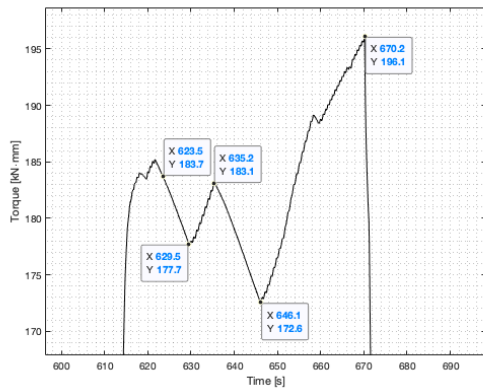
Figure A.22: Max and min values
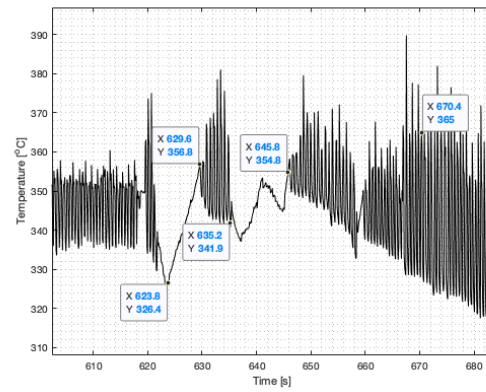
Figure A.23: Max and min values

A.3.7 Test 7
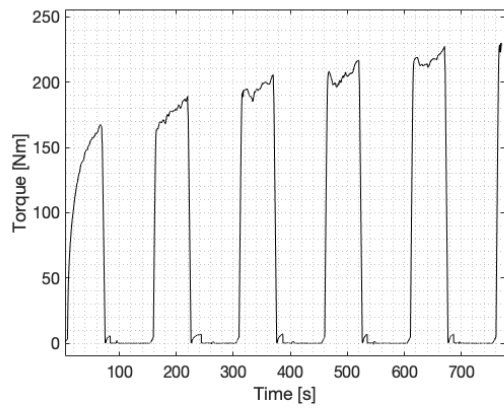
Figure A.24: Torque vs time
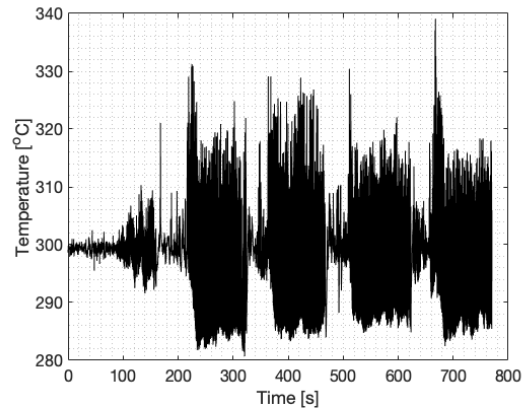
Figure A.25: Temperature vs time
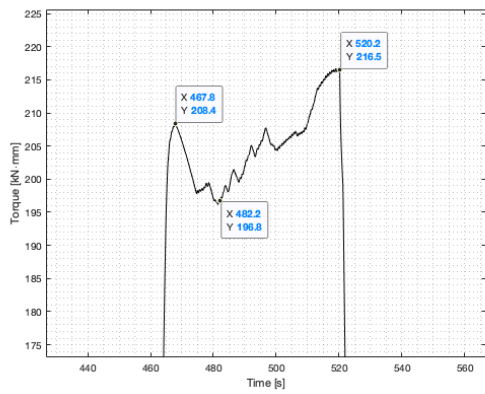
Figure A.26: Max and min values
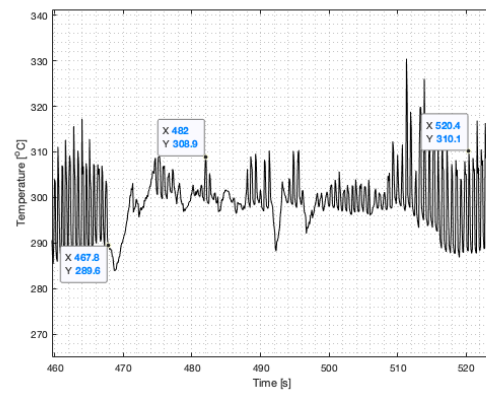
Figure A.27: Max and min values

A.4   Hardness Samples

A seperate plot of the hardness gradient is presented for each test. The plots show also the standard deviation.

A.4.1   Test 1

The hardness gradient for test 1 is plotted in figure A.28. The decrease in hardness is approximately linear down with the same slope for the depths: 0.7 mm - 2.2 mm and 3.2 - 5.2mm. The sample diameter was 13.6 mm and eight measurements was made for each depth. For all depths the mean value of hardness is above 330 which is 60 HV10 higher than the reference hardness. Maximum hardness was measured to 370 HV10 at a depth of 0.7 mm below the surface.
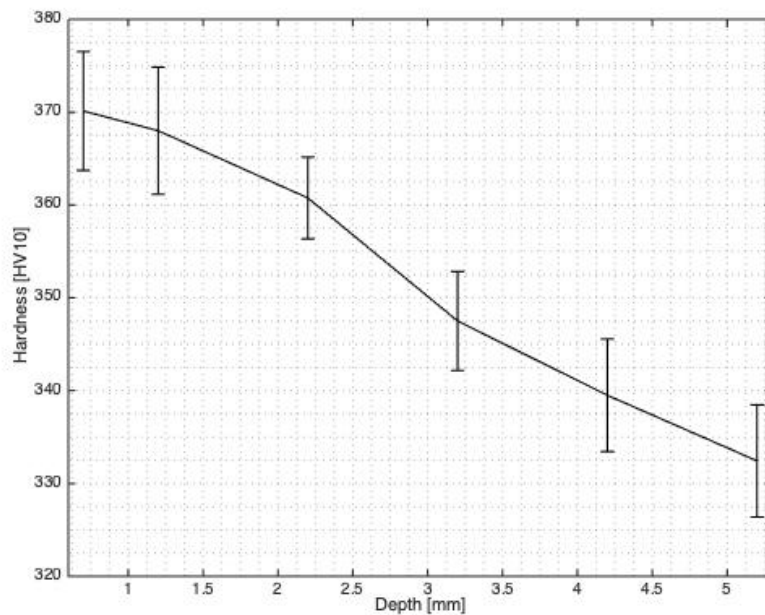
Figure A.28: Hardness gradient for test 1

A.4.2   Test 2

The hardness gradient for test 2 is plotted in figure A.29. The decrease in hardness is quite linear between 0.7 mm to 2.2 mm and then there is a larger drop in hardness. The sample diameter was 10 mm and eight measurements was made for each depth. For all depths the mean value of hardness is above 330 which is 60 HV10 higher than the reference hardness. Maximum hardness was measured to 364 HV10 at a deth of 0.7 mm below the surface.
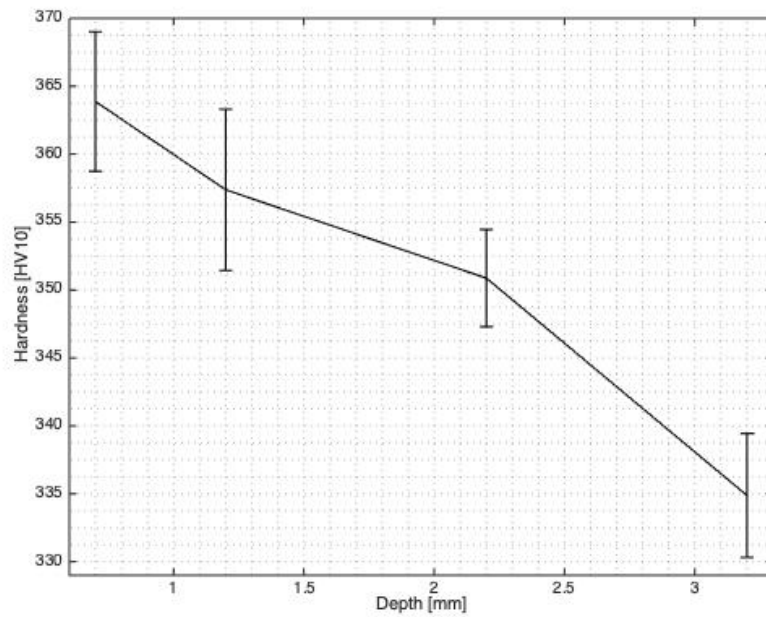
Figure A.29: Hardness gradient for test 2

A.4.3 Test 3

The results of hardness measurement for test 3 are shown in A.30. The error bar illustrate the standard deviation at different depth. Fairly linear decrease of hardness are shown towards the centre of the test bar. Highest hardness is measured at the surface which is reasonable because of higher strains are built up there. Maximum hardness was measured to 396HV10 for 3U and 365HV10 for 3L at a depth 0.7mm below the surface.
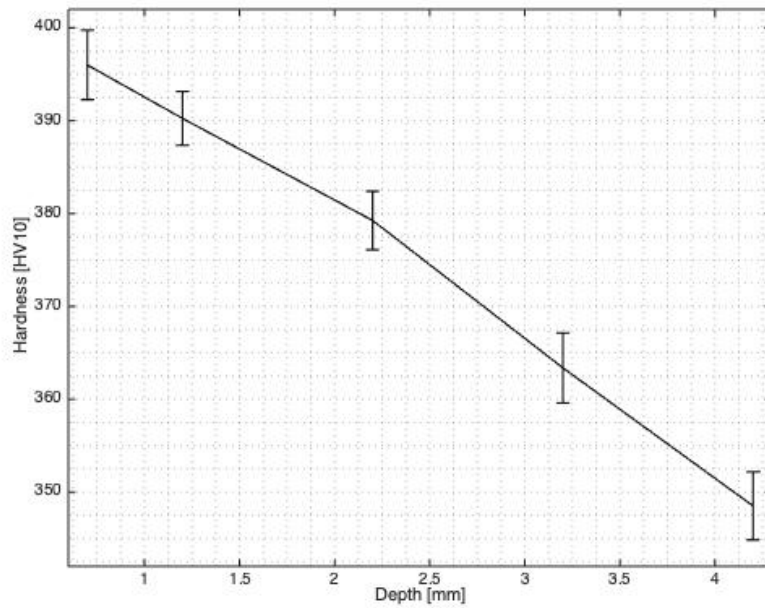
Figure A.30: Hardness gradient for test 3

A.4.4   Test 4

The results of hardness measurement for test 4 are shown in A.31. The error bar illustrate the standard deviation at different depth. Fairly linear decrease of hardness are shown towards the centre of the test bar. Highest hardness is measured at the surface which is reasonable because of higher strains are built up there. Maximum hardness was measured to 342.5HV10 at a depth 0.7mm below the surface.
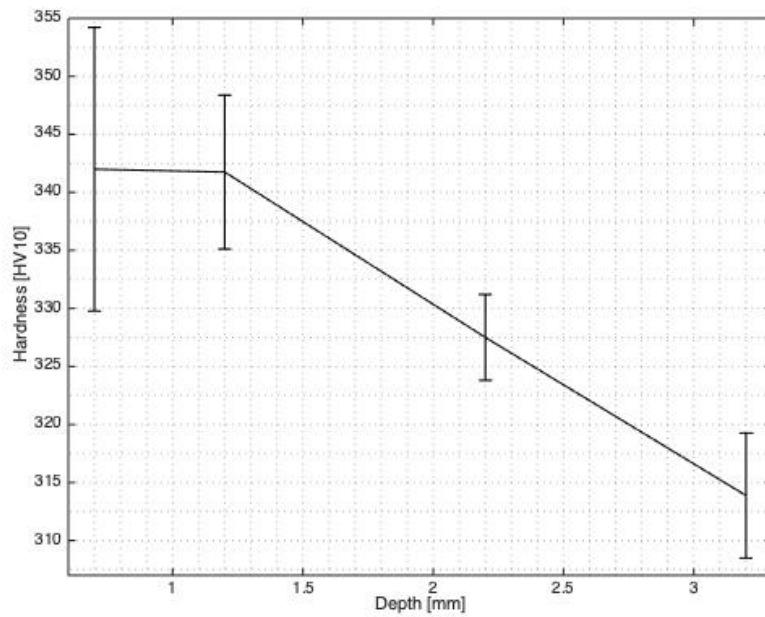
Figure A.31: Hardness gradient for test 4

A.4.5 Test 5

The results of hardness measurement for test 5 are shown in A.32. The error bar illustrate the standard deviation at different depth. Fairly linear decrease of hardness are shown towards the centre of the test bar. Highest hardness is measured at the surface which is reasonable because of higher strains are built up there. Maximum hardness was measured to 470HV10 at a depth 0.7mm below the surface.
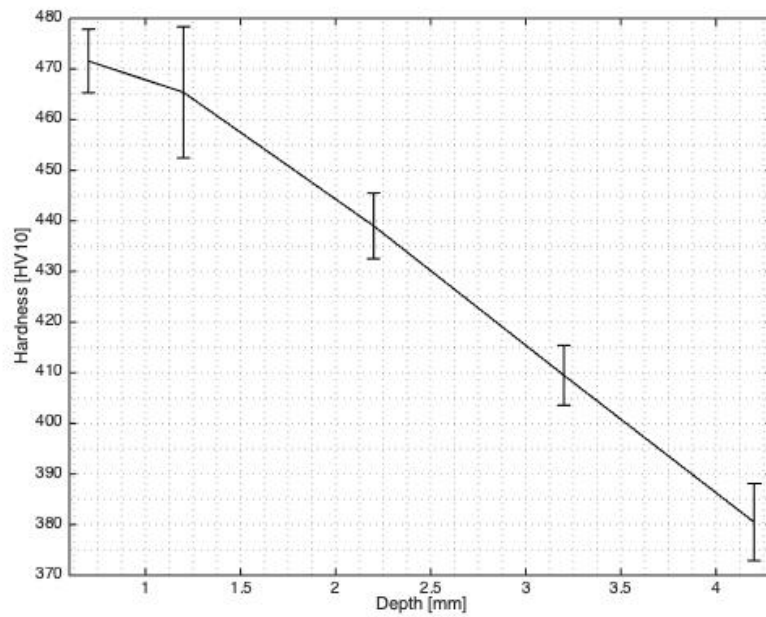
Figure A.32: Hardness gradient for test 5

A.4.6   Test 6

The results of hardness measurement for test 6 are shown in A.33. The error bar illustrate the standard deviation at different depth. Fairly linear decrease of hardness are shown towards the centre of the test bar. Highest hardness is measured at the surface which is reasonable because of higher strains are built up there. Maximum hardness was measured to 480HV10 at a depth 0.7mm below the surface.
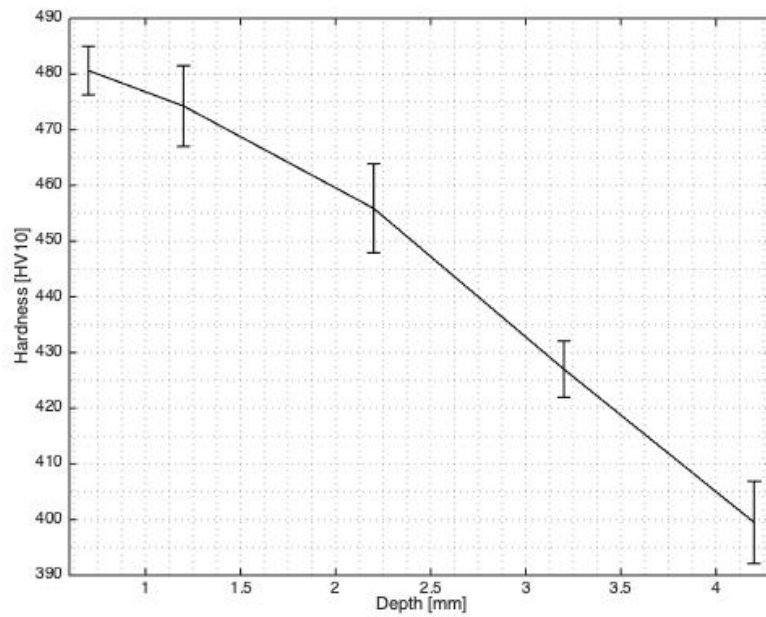
Figure A.33: Hardness gradient for test 6

A.4.7 Test 7

The results of hardness measurement for test 7 are shown in A.34. The error bar illustrate the standard deviation at different depth. Fairly linear decrease of hardness are shown towards the centre of the test bar. Highest hardness is measured at the surface which is reasonable because of higher strains are built up there. Maximum hardness was measured to 412.5HV10 at a depth 0.7mm below the surface.
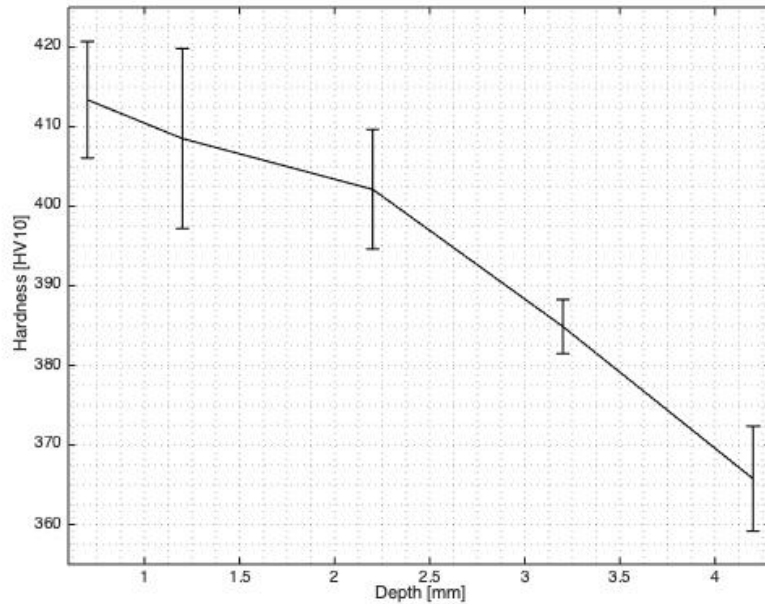
Figure A.34: Hardness gradient for test 7

A.5 Microstructure from OM

All micrographs are taken with a magnification 100x. The micrograph show flowlines with a certain inclination. The angle of the flowlines was later used to quantify the amount of accumulated shear strain. Some micrographs contain black dots which are artifacts from too long etching. Other artifacts e.g cracks and scratches occured after mounting and polishing. The main result from the characterization was that the acculumated shear strain increased with decreased angle between the flowlines which can bee seen in A.35-A.41.

A.5.1 Test 1

An overview of the microstructure for test 1, see A.35. The micrograph show a microstructure which is aligned with flowlines that were easily distinguished. The micrograph contain some artifacts generated from the polishing, but the image is still representative to the microstructure.
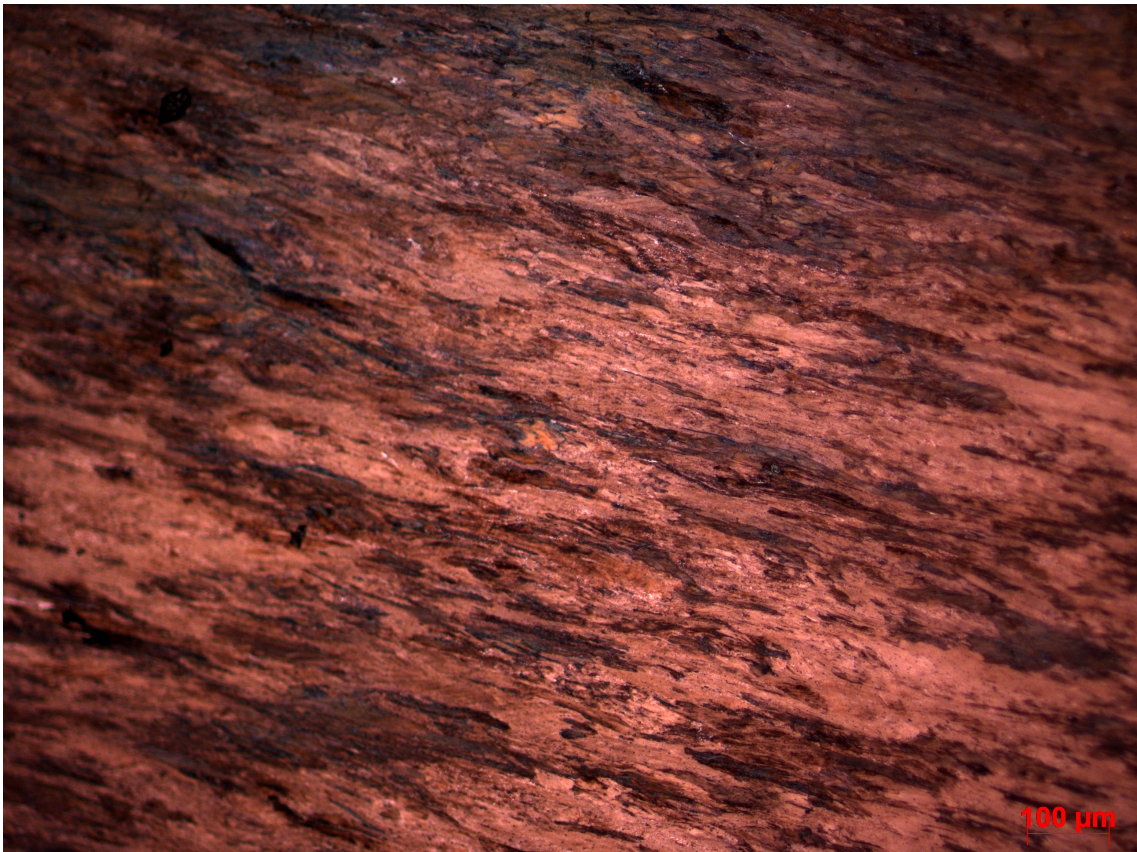
Figure A.35: Microstructure test 1

A.5.2 Test 2

An overview of the microstructure for test 2, see A.36. Artifacts e.g scratches are visible. The flowlines angle could however be measured.

Figure A.36: Microstructure test 2

A.5.3 Test 3

An overview of the microstructure for test 3, see A.37. Flowslines were easily distinguished due to the high amount of accumulated shear strain. The black dots were artifacts generated from too long etching.
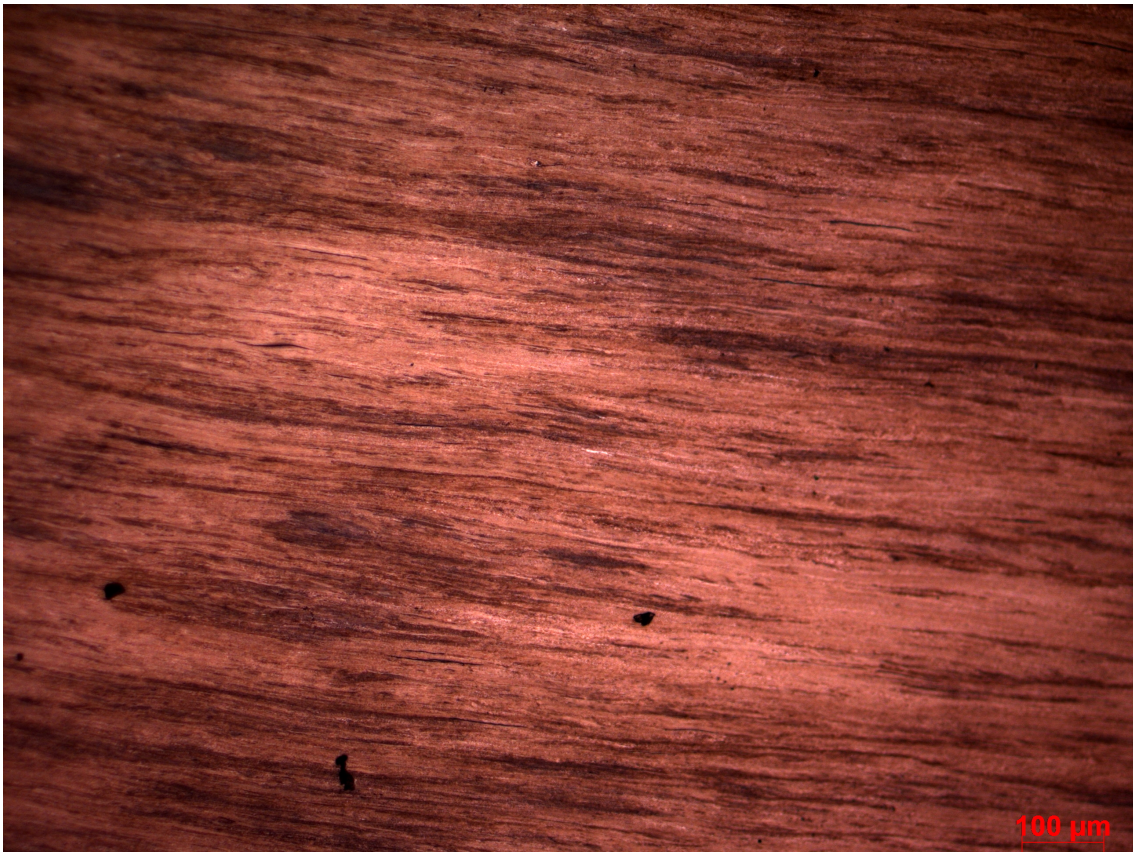
Figure A.37: Microstructure test 3

A.5.4   Test 4

An overview of the microstructure for test 4, see A.38. Flowslines was difficult to distinguish due to the low amount of accumulated shear strain.
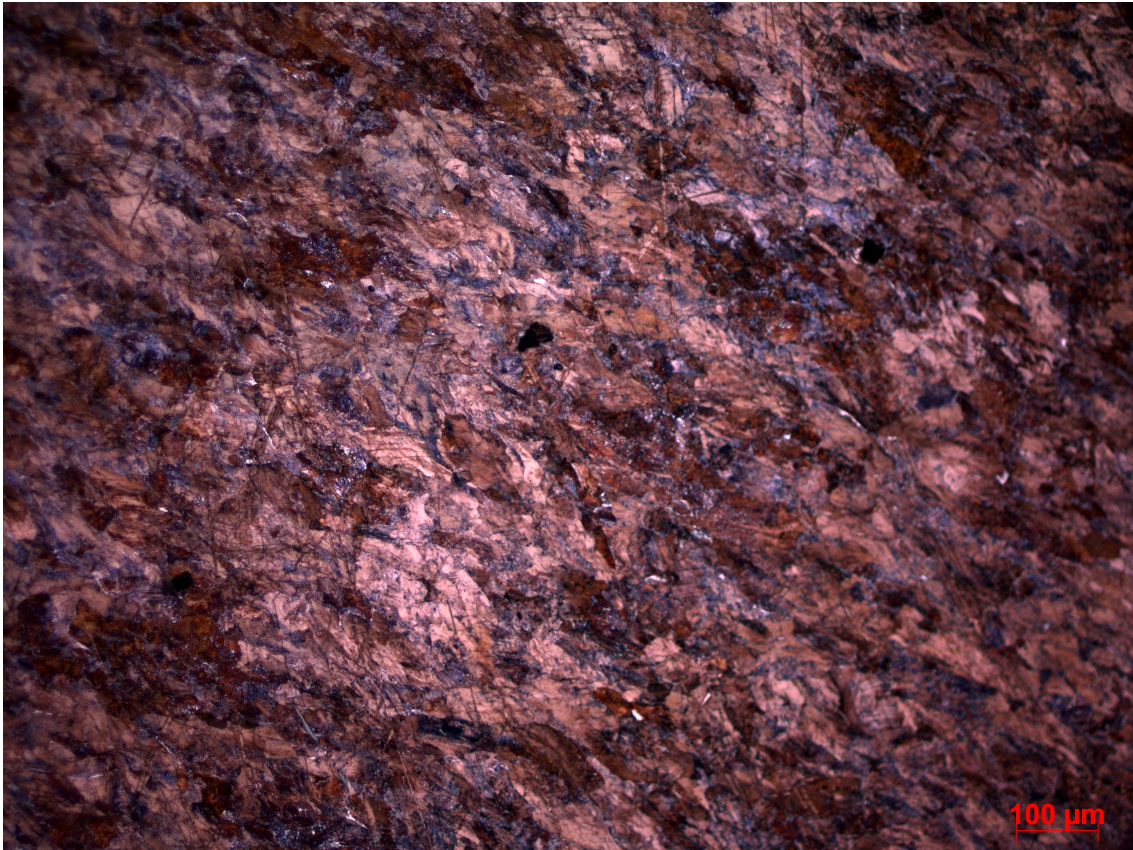
Figure A.38: Microstructure test 4

A.5.5   Test 5

An overview of the microstructure for test 5, see A.39. An aligned microstructure with low angled flowlines were visible. Some artifacts e.g crack and scratches were generated from the grinding and polishing.
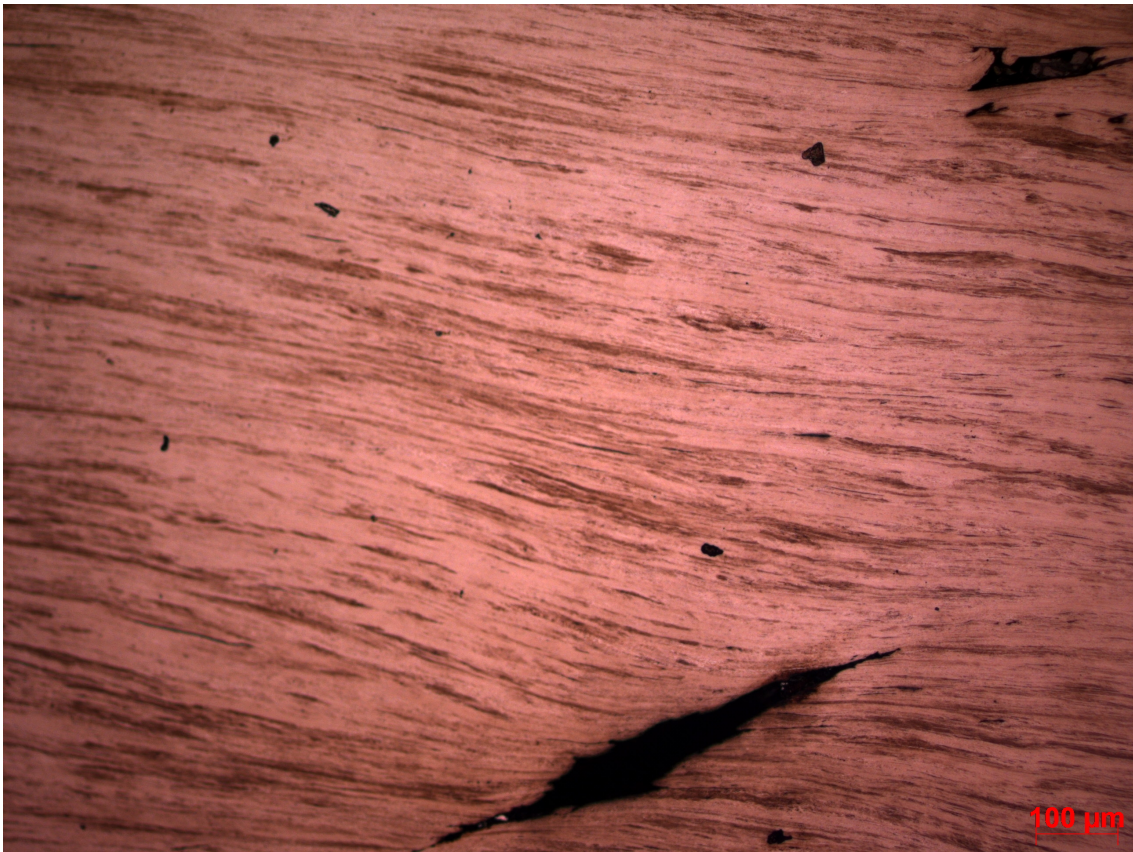
Figure A.39: Microstructure test 5

A.5.6   Test 6

An overview of the microstructure for test 6, see A.40. The microstructure was aligned and the flowlines were easily distinguished. Artifacts e.g scratches and cracks were generated from the sample preparation.
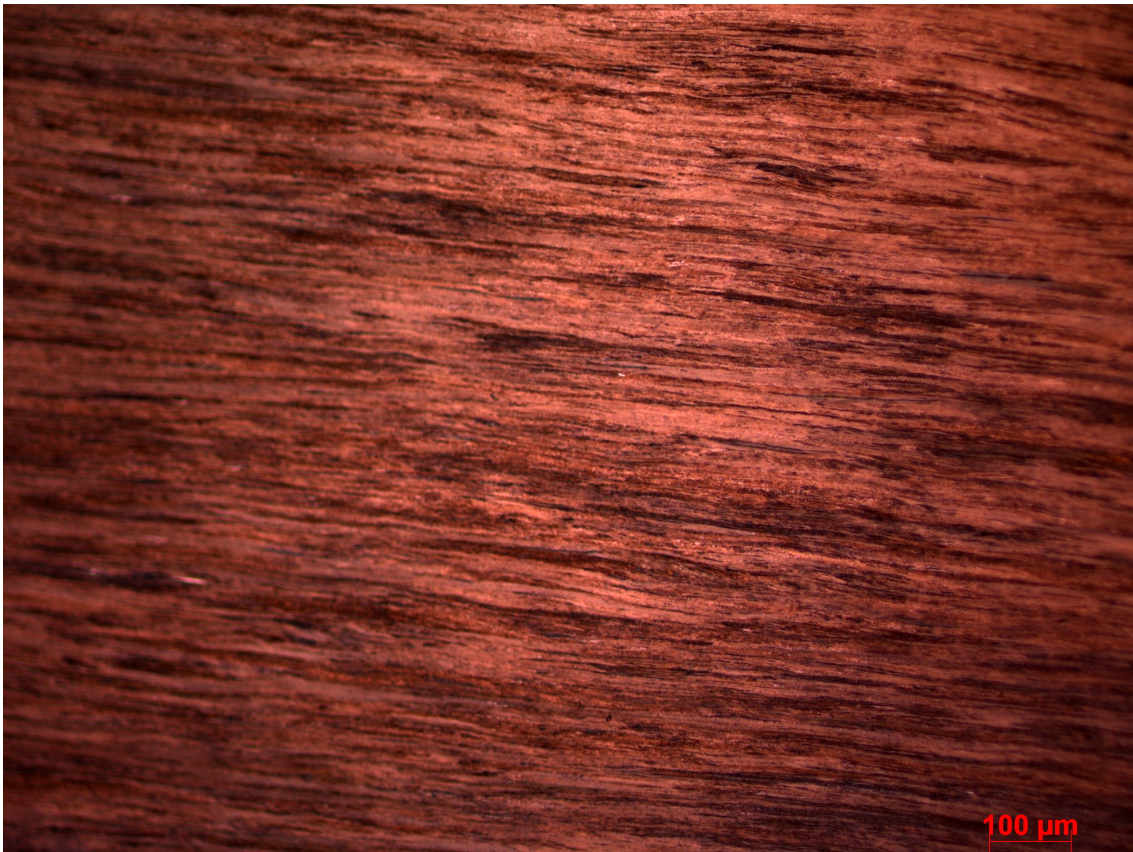
Figure A.40: Microstructure test 6

A.5.7 Test 7

An overview of the microstructure for test 7, see A.41. The black dots are the artifacts which was previously mentioned. Flowlines could be measured for this test.

Figure A.41: Microstructure test 7

A.5.8   Field samples: Rail 3
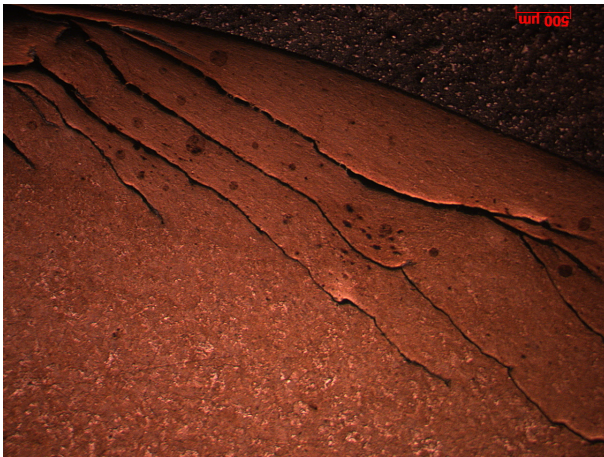
Figure A.42: Rail 3: Flowlines corner

Figure A.43: Rail 3: Undeformed microstructure
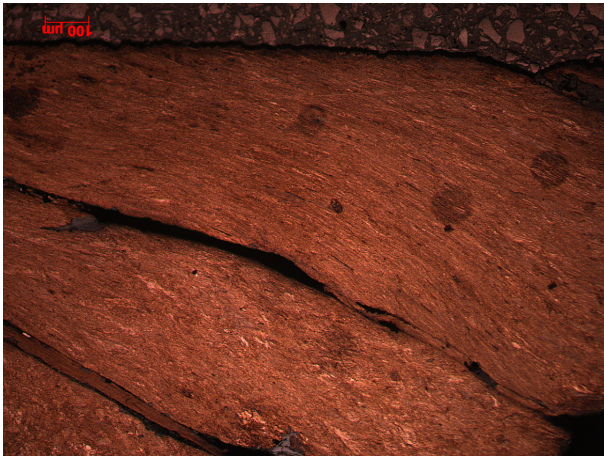
Figure A.44: Rail 3: Flowlines corner

Figure A.45: Rail 3: Flowlines corner

A.5.9   Field samples: Rail 4
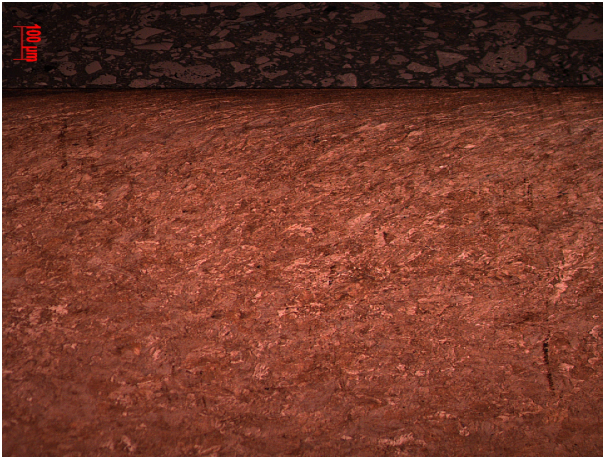
Figure A.46: Rail 4: Flowlines
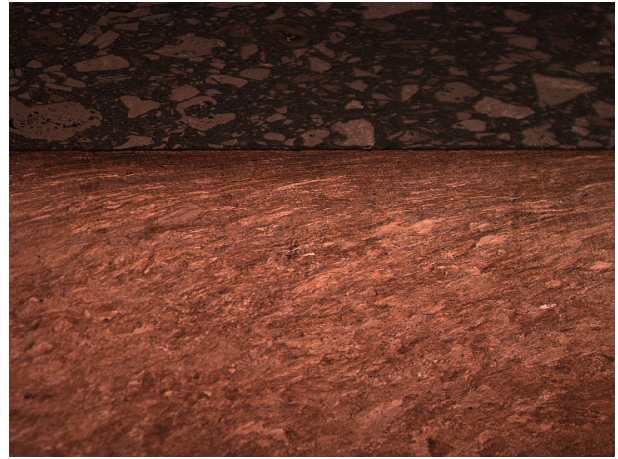
Figure A.47: Rail 4: Flowlines
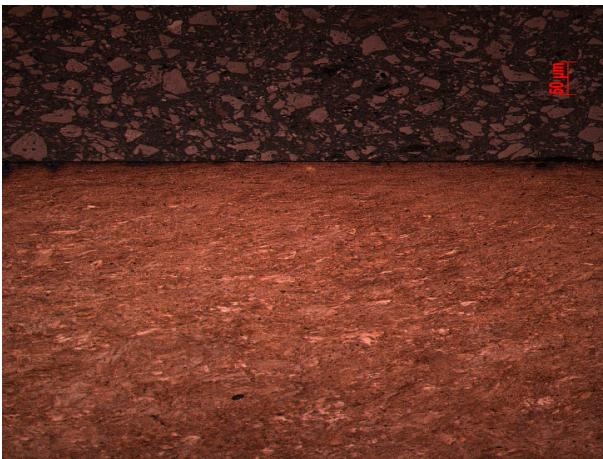
Figure A.48: Rail 4: Flowlines
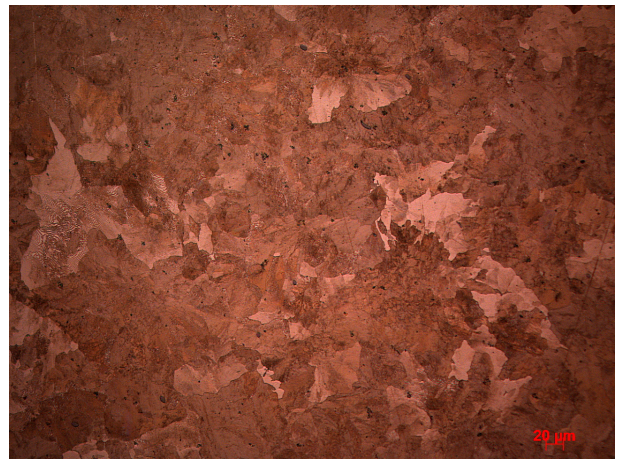
Figure A.49: Rail 4: Undeformed microstructure

A.5.10   Reference: Room Temperature
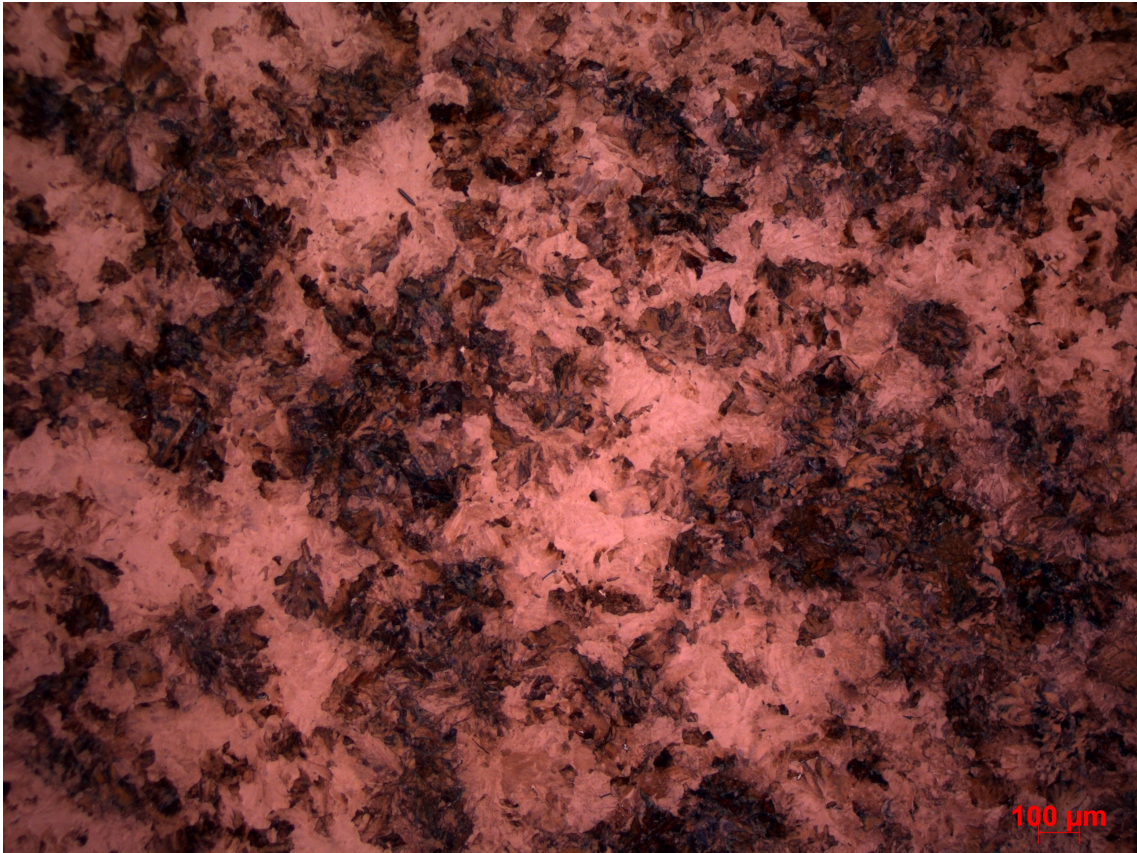
Figure A.50: Microstructure for reference sample

A.5.11   Heat Treatment: 350°C
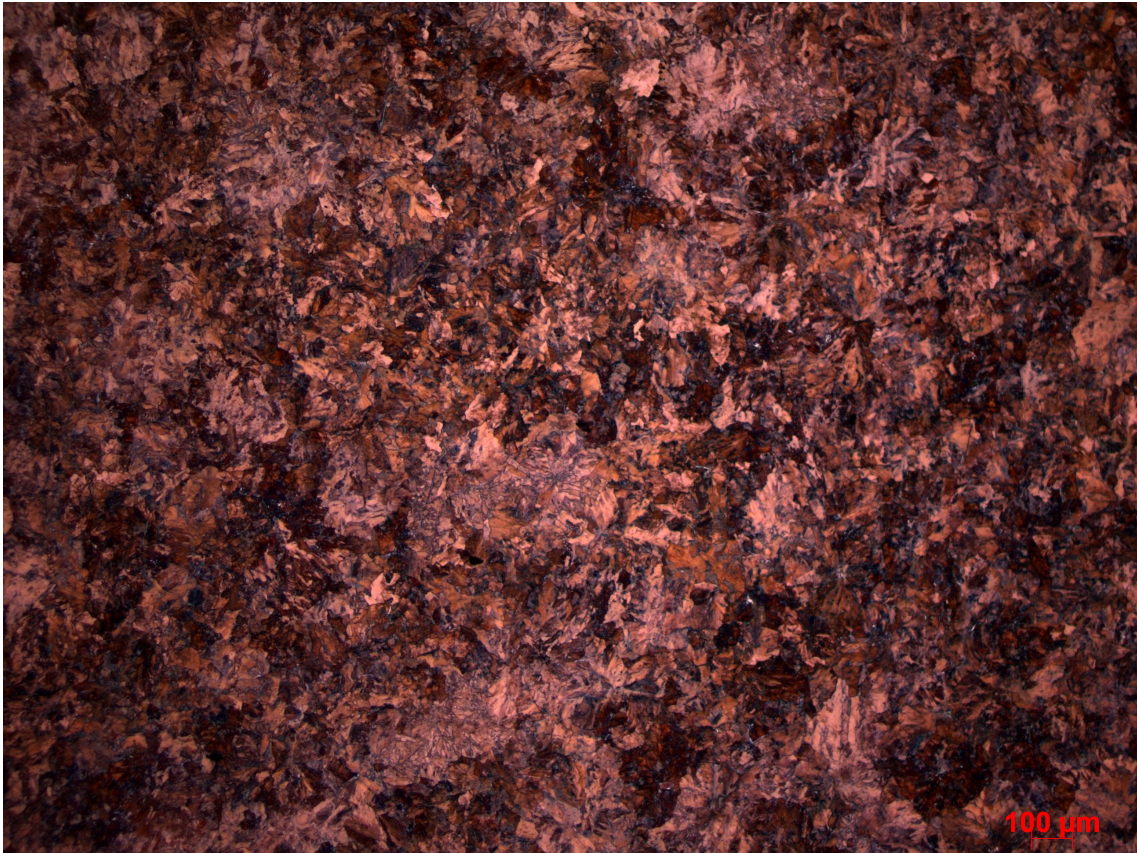
Figure A.51: Microstructure for heat treatment sample 350 °C.

A.5.12 Heat Treatment: 400°C

Figure A.52: Microstructure for heat treatment sample 400 °C.

A.6   Microstructure SEM

Extra micrographs are presented for those testss which achieved high accumulated shear strain (see test 3, 5 and 6).

A.6.1   Test 3
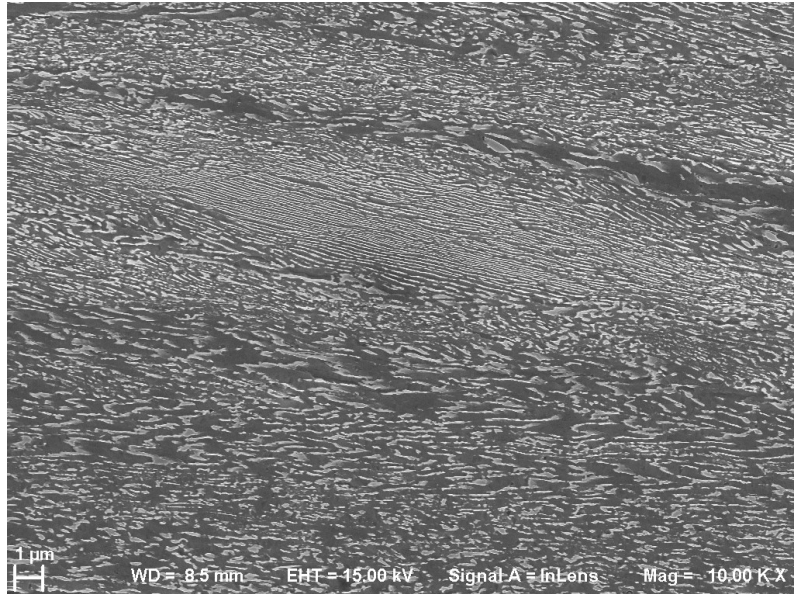
Figure A.53: Microstructure test 3.
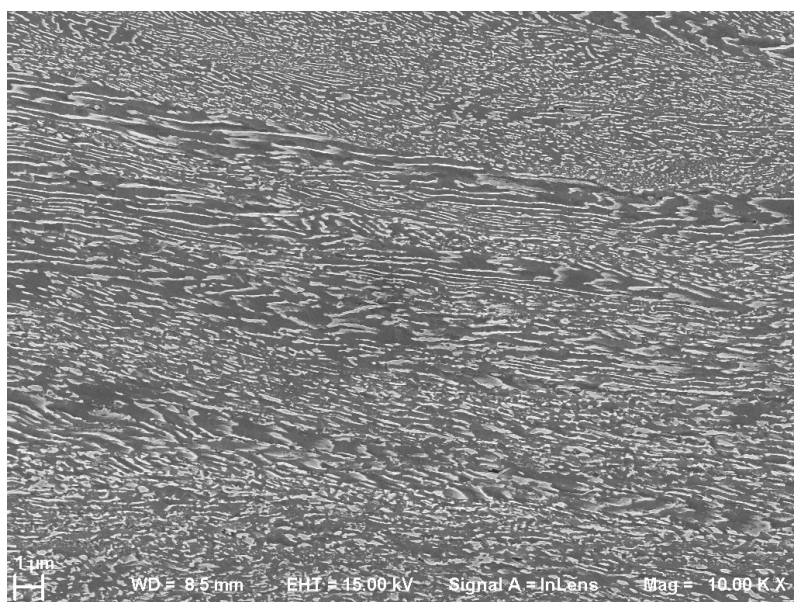
Figure A.54: Microstructure test 3.

A.6.2 Test 5
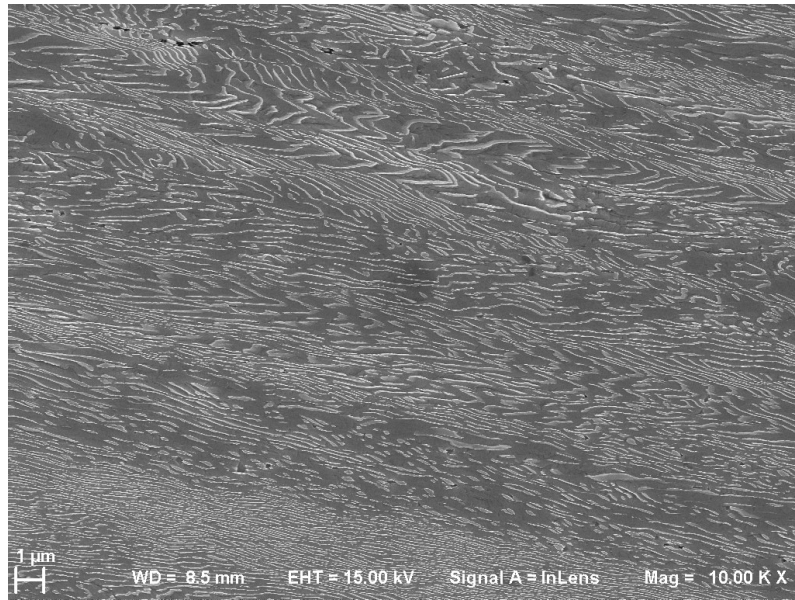
Figure A.55: Microstructure test 5.
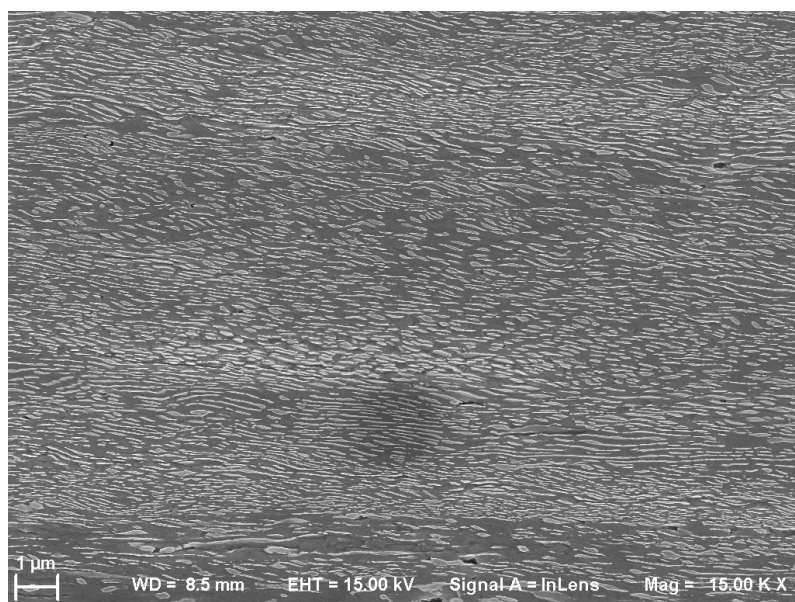
Figure A.56: Microstructure test 5.

XXX

A.6.3 Test 6
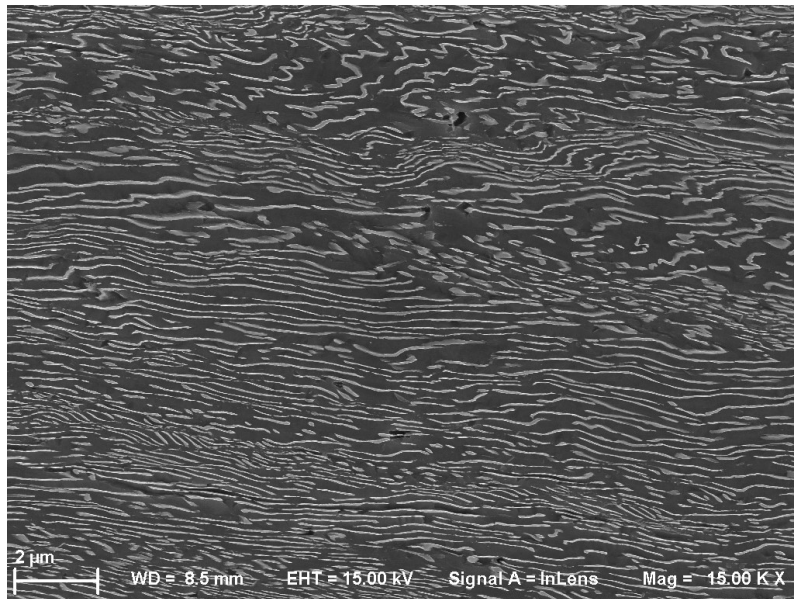
Figure A.57: Microstructure test 6.
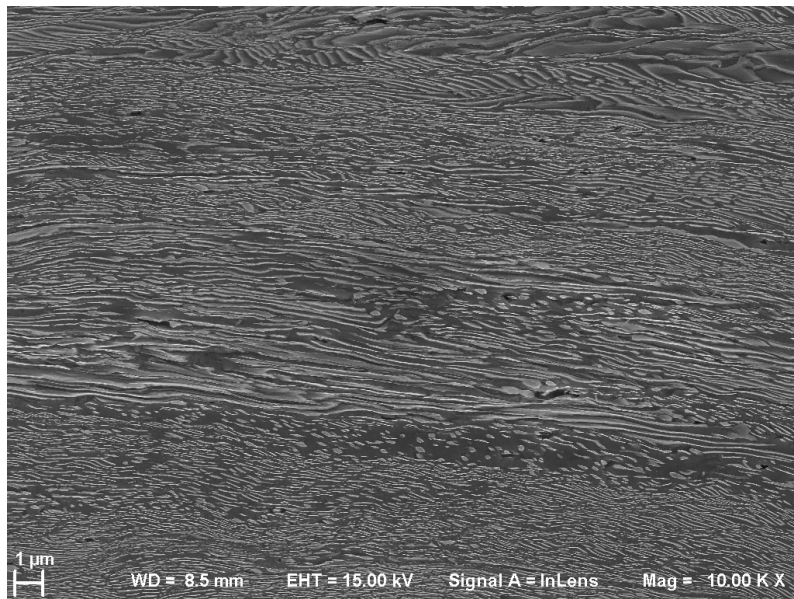
Figure A.58: Microstructure test 6.

A.7 Deformed Test Bars for Test 1-3

A.7.1 Buckled Test Bar for Test 1

Figure A.59: Test bar 1.

Figure A.60: Test bar 1.

A.7.2   Broken Test Bar for Test 2

Figure A.61: Test bar 2.

A.7.3   Deformed Test Bar for Test 3

Figure A.62: Test bar 3.